UNIVERSITÀ DEGLI STUDI DI CATANIA
Department of Biomedical and Biotechnological Sciences
PhD Course in Basic and Applied Biomedical Sciences
Curriculum Molecular Biomedicine and Biotechnology

XXXVIII Cycle

Paolo Giuseppe Bonacci

ELECTROROTATION-BASED CHARACTERIZATION OF HUMAN CELL LINES: A MOLECULAR AND DIELECTROPHORETIC APPROACH

PhD Thesis

Tutor:
Prof. Stefania Stefani

Co-Tutor:
Prof. Nicolò Musso

Academic Years 2022-2025

INDEX

0. ABSTRACT 6
ABBREVIATIONS 7
1. INTRODUCTION 9
1.1. THE CTCs ROLE IN ONCOLOGIC DIAGNOSTIC 9
1.2. LABEL-BASED and LABEL-FREE TECHNIQUES 13
1.2.1. Label-Based Techniques 13
1.2.2. Label-Free Techniques 15
1.3. DIELECTROPHORESIS and ELECTROROTATION 20
1.3.1. State of Art of DEP and ROT in Diagnostic Applications. 24
1.4. AIM of THE WORK 27
2. MATERIALS 30
2.1. EFFECTS OF BUFFER FORMULATION ON CELL BEHAVIOR 30
2.1.1. Buffer Composition 30
2.1.2. Evaluation of Buffers compositions on cell viability 31
2.1.3. Discrimination Capacity Analysis 32
2.1.4. Flow Cytometry Sample Preparation 33
2.1.5. Gene Expression Analysis via RT-qPCR 34
2.1.6. Osmolarity Measurement and Statistical Analysis 36
2.1.7. Impact of Conductivity on CaCo-2 Cell line 36
2.2. ELECTROROTATION EXPERIMENTS 37
2.2.1. Electrorotation System 37
2.2.2. Electrorotation Device and Microchip Design 39
2.2.3. Cell Lines Involved in Electrorotation Experiments 41
2.2.4. Electrorotation Experiments[98] 44
2.2.5. RT-qPCR for Electrorotation-related genes 47
3. RESULTS 50
3.1. IMPACT of BUFFER on CELL LINES 50

3.1.2. FlowSight® Imaging Flow Cytometer Analysis..... 51
3.1.3. Buffer Composition impact on Gene Expression Modulation 55
3.1.4. Impact of Conductivity on Cell Viability..... 59
3.2. ELECTROROTATION SPECTRA..... 60
3.3 RT-qPCR for ELECTROROTATION-RELATED GENES..... 65
4. DISCUSSION 70
4.1. SUITABILITY OF THE BUFFER SYSTEM FOR ROT EXPERIMENTS 70
4.2. ELECTROROTATION SPECTRA REVEAL CELL TYPE- AND TISSUE-SPECIFIC DIELECTRIC BEHAVIOR..... 77
4.3. CORRELATION BETWEEN *BANP* AND *PTK2* EXPRESSION AND ELECTROROTATION PEAK FREQUENCY 80
5. CONCLUSION and FUTURE PERSPECTIVES 86
6. RESEARCH CONTRIBUTIONS AND DISSEMINATION ... 89
6.1. RELATED TO PhD PROJECT 89
6.2. OTHER PUBLICATIONS AND CONTRIBUTIONS 98
6.3. PARTICIPATION IN NATIONAL AND INTERNATIONAL CONFERENCES 102
7. ACKNOWLEDGMENTS 105
8. BIBLIOGRAPHY 107

0. ABSTRACT

This thesis explores the potential of electrorotation (ER) as a powerful, label-free technique for characterizing the dielectric properties of living cells, with implications for both fundamental research and biomedical applications. By developing and validating biocompatible buffers, optimal experimental conditions were established to preserve cell viability and molecular integrity during ER measurements. Electrorotation spectra from twelve human cell lines of different tissue origins revealed distinctive, tissue-specific behaviors. In solid tissue-derived lines (breast, prostate, and colon), ER effectively discriminated between non-tumorigenic and tumorigenic phenotypes, reflecting differences in membrane structure, cytoplasmic conductivity, and intracellular organization. Hematological lines exhibited flatter, more homogeneous spectra, consistent with their suspension nature and reduced internal complexity. Correlation analysis identified a consistent association between BTG3 Associated Nuclear Protein (*BANP)* expression and the ER peak position in solid tissues, suggesting a link between chromatin organization and dielectric response. Conversely, Protein Tyrosine Kinase 2 (*PTK2),* expression showed no significant correlation. Overall, this work establishes electrorotation as a sensitive, non-destructive biophysical profiling tool, providing a foundation for future studies on complex biological systems and for the integration of computational approaches. Its potential applications include cell-based diagnostics, tumor detection, and functional characterization in translational biomedical research.

ABBREVIATIONS

Abbreviation	Full Term (English)	Abbreviation	Full Term (English)
184A1	Non-Tumorigenic Human Mammary Epithelial Cell Line	HCT-116	Human Colorectal Carcinoma Cell Line
ACTB	Beta-Actin	HDLM-2	Human Hodgkin Lymphoma Cell Line
ATCC	American Type Culture Collection	IL-6β	Interleukin 6 Beta
BANP	BTG3 Associated Nuclear Protein	iDEP	Insulator-Based Dielectrophoresis
BSA	Bovine Serum Albumin	iNOS	Inducible Nitric Oxide Synthase
CaCo-2	Human Colorectal Adenocarcinoma Cell Line	LAMP	Loop-Mediated Isothermal Amplification
CCD-841 CoN	Normal Human Colon Epithelial Cell Line	LDH	Lactate dehydrogenase
CD45	Cluster of Differentiation 45	LnCaP	Human Androgen-Sensitive Prostate Cancer Cell Line
CK	Cytokeratin	LOD	Limit of Detection
CTCs	Circulating Tumor Cells	MCF-7	Human Luminal Breast Cancer Cell Line
DEP	Dielectrophoresis	MDA-MB-231	Human Triple-Negative Breast Cancer Cell Line
DLD	Deterministic Lateral Displacement	MEM	Minimum Essential Medium
DMEM	Dulbecco's Modified Eagle Medium	MET	Mesenchymal–Epithelial Transition
DMSO	Dimethyl Sulfoxide	MTT	3-(4,5-Dimethylthiazol-2-yl)-2,5-Diphenyltetrazolium Bromide
DAPI	4′,6-Diamidino-2-Phenylindole	NK	Natural Killer (cell)
EMT	Epithelial–Mesenchymal Transition	PBS	Phosphate Buffered Saline
EpCAM	Epithelial Cell Adhesion Molecule	PCR	Polymerase Chain Reaction

Abbreviation	Full Term (English)	Abbreviation	Full Term (English)
ER	Electrorotation	PC-3	Human Prostate Cancer Cell Line (Bone Metastasis)
FAK	Focal Adhesion Kinase	PTK2	Protein Tyrosine Kinase 2 (Focal Adhesion Kinase 1, FAK1)
FBS	Fetal Bovine Serum	PWR-1E	Normal Human Prostate Epithelial Cell Line
FDA	Food and Drug Administration	qAMP	Quadrature Amplifier
FPS	Frames Per Second	qPCR	Quantitative Polymerase Chain Reaction
GAPDH	Glyceraldehyde-3-Phosphate Dehydrogenase	RNA	Ribonucleic Acid
HCC1937 BL	Epstein–Barr Virus-Transformed Lymphoblastoid Cell Line	RPMI	Roswell Park Memorial Institute Medium
ROT	Electrorotation	ROS	Reactive Oxygen Species
SSC	Side Scatter	RT-qPCR	Reverse Transcription Quantitative Polymerase Chain Reaction
U266	Human Multiple Myeloma Cell Line	TGF-β	Transforming Growth Factor Beta

1. INTRODUCTION

1.1. THE CTCs ROLE IN ONCOLOGIC DIAGNOSTIC

Circulating tumor cells (CTCs) represent a crucial focus in modern oncological diagnostics[1–3]. They are malignant cells that detach from the primary tumor and disseminate through the circulatory system, traveling as single units or clusters (Figure 1).

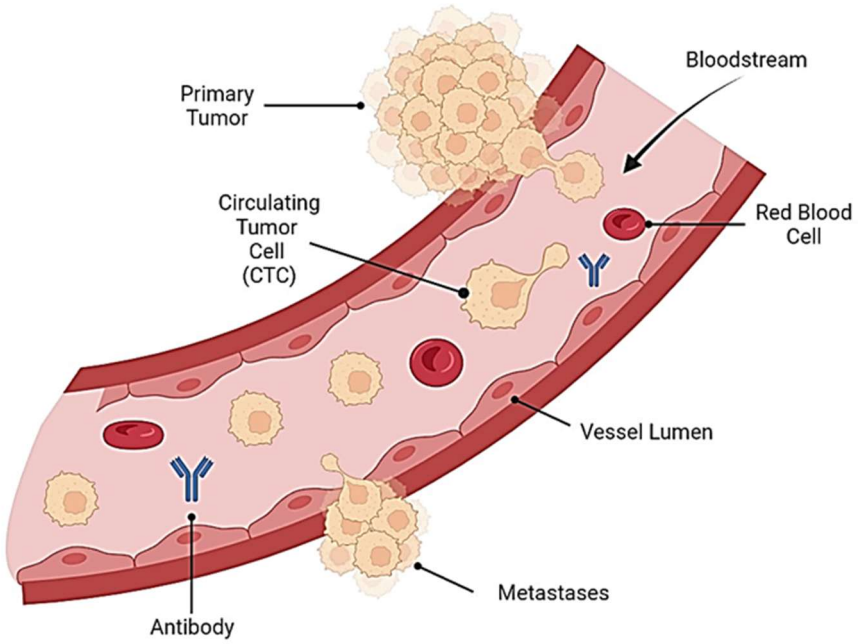

***Figure 1**. Graphic representation of the metastatic process. Figure created by the candidate using BioRender®.*

This phenomenon is closely associated with the metastatic process, one of the leading causes of cancer-related mortality[4]. The first observation of CTCs backs to 1869, when Australian physician Thomas Ashworth identified tumor-like cells in the blood of a cancer patient[5]. Since then, the role of CTCs as mediators of metastasis and potential diagnostic biomarkers has become an increasingly relevant scientific topic [3,6]. CTCs

retain many of the characteristics of the primary tumor[7], including genetic and phenotypic heterogeneity. This makes them unique for monitoring tumor status, providing valuable information on disease progression and treatment response[8]. However, their rarity in the bloodstream, often only a few tumor cells among billions of normal cells, in other words 1-10 per mL of blood [9], poses a significant challenge for their detection and isolation.

Historically an important milestone about metastasis process and mechanisms was the “seed and soil” hypothesis[10] that was proposed by Stephen Paget in 1889: his autopsy studies of breast cancer patients showed that metastases were more common in organs like the liver and lungs suggesting that the organ microenvironment plays a crucial role in whether metastasis occurs. It has led to the discovery of pre-metastatic niches, where tumors can condition distant organs to become more hospitable before cancer cells arrive and modern oncology integrates molecular mechanisms such as exosome signaling[11], cytokine networks[12], and stromal cell interactions[13] into Paget’s original model. This theory contrasts with Ewing's mechanical hypothesis[14], which suggested that metastases occur based on blood flow patterns alone. However, current evidence supports Paget’s model, as molecular and cellular interactions play a significant role in metastatic spread[15,16]. This challenge has driven the development of innovative methods for CTC identification and analysis, as early and accurate diagnosis is crucial for improving therapeutic options and patient prognosis. In modern diagnostics, the importance of early CTC detection is dual. First, it enables the identification of a tumor in its early stages, when it is still localized and treatable. Second, it allows monitoring metastatic dissemination, offering insights into tumor dynamics and therapeutic efficacy. Unlike traditional

biopsies, CTC analysis via liquid biopsy is minimally invasive and provides a temporal and spatial representation of tumor heterogeneity[17]. This approach overcomes many limitations of conventional techniques, which often fail to capture the tumor's dynamic complexity.

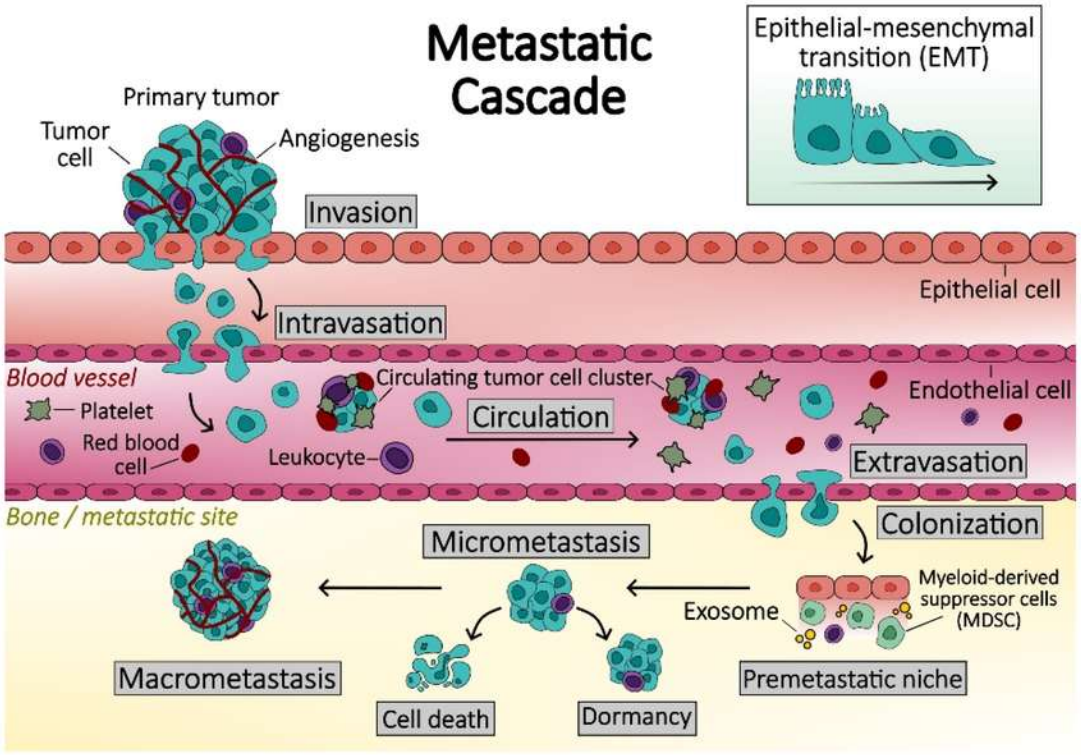

Figure 2. Multi-step process of cancer metastasis, where tumor cells spread from the primary site to distant organs. The cascade begins with tumor growth and angiogenesis, followed by epithelial–mesenchymal transition (EMT), which enhances cell motility and invasiveness. Cancer cells then invade surrounding tissues, enter the bloodstream (intravasation), and travel as single cells or clusters, interacting with platelets and leukocytes. Upon reaching distant sites, they exit circulation (extravasation) and may either remain dormant or initiate colonization. By recruiting supportive cells like myeloid-derived suppressor cells (MDSCs), they create a premetastatic niche that facilitates tumor growth. The interplay between cancer cells, the immune system, and the tumor microenvironment is critical for metastatic progression[18].

Their biological behavior is dictated by a complex interplay of cellular plasticity, survival mechanisms, and interactions with the tumor microenvironment. About this, a critical step in CTC biology is the epithelial-mesenchymal transition (EMT) [19], a process that enables

epithelial-derived tumor cells to acquire mesenchymal characteristics, enhancing their motility, invasiveness, and resistance to anoikis[20] (Figure 2). This transition is coordinated by key transcription factors such as *SNAIL*[21], *SLUG*[22], *ZEB1/2*[23] , and *TWIST*[24], which suppress epithelial markers (e.g., E-cadherin) and upregulate mesenchymal markers (e.g., vimentin, N-cadherin). However, CTCs rarely exhibit a fully mesenchymal phenotype; instead, they exist in a spectrum of EMT states, ranging from epithelial-like to hybrid (partial EMT) or fully mesenchymal[25]. This plasticity allows dynamic adaptation to microenvironmental pressures and influences metastatic potential. Once in the bloodstream, CTCs encounter shear stress, immune surveillance, and oxidative stress, requiring specialized adaptations for survival. One of these is the expression of *CD47* ("don't eat me" signal) allows immune evasion by inhibiting macrophage-mediated phagocytosis[26], while platelet cloaking shields CTCs from natural killer[27] (NK) cell cytotoxicity and provides pro-survival signaling via *TGF-β* and *PDGF*[28]. Additionally, CTCs upregulate antioxidant defense systems [29](e.g., *NRF2* pathway activation) to mitigate reactive oxygen species (ROS)-induced apoptosis. CTCs are found as single cells or clusters, with CTC clusters exhibiting markedly higher metastatic potential due to intercellular adhesion molecules (e.g., plakoglobin, connexins) and cooperative survival signaling[30]. Clusters retain epithelial traits while expressing mesenchymal markers, indicating a unique hybrid EMT state that confers increased metastatic fitness. Extravasation involves adhesion to the vascular endothelium, transmigration, and colonization of distant tissues. CTCs use selectins, integrins (e.g., αvβ3), and chemokine receptors (e.g., *CXCR4*, *CCR7*) to adhere to endothelial cells and migrate through endothelial gaps[31]. Once in the secondary site, they must overcome quiescence signals

and adapt to the new microenvironment, often undergoing mesenchymal-epithelial transition (MET) to reinitiate proliferation.

1.2. LABEL-BASED and LABEL-FREE TECHNIQUES

It is clear that the isolation and detection of circulating tumor cells (CTCs) have been widely explored as a non-invasive approach for cancer diagnosis and monitoring[32]. Over the years, two primary strategies have emerged: label-based and label-free techniques. Label-based methods, developed in the early 2000s, detect specific molecular markers expressed on CTCs to enable their selective capture, often using immunoaffinity-based technologies[33]. In contrast, label-free techniques exploit the intrinsic physical properties of CTCs, such as size, density, and response to an external field, to achieve label-free isolation. While label-based methods offer high specificity, they may miss heterogeneous CTC populations[34], making label-free approaches an attractive alternative. These techniques are, however, continuously improved by modern research to implement sensitivity, reliability, and clinical applicability in liquid biopsy strategies.

1.2.1. Label-Based Techniques

Label-based techniques (or active methods) for circulating tumor cell (CTC) isolation allow the identification and capture of cells expressing specific biomarkers[35]. These methods mainly use antibodies conjugated to magnetic beads or fluorescent dyes to target epithelial markers such as EpCAM[36] (epithelial cell adhesion molecule) and cytokeratins[37], which are commonly expressed by CTCs but missing in normal blood cells. In

this context, the most used system is undoubtedly the CellSearch® platform[38–40], that is the first and only FDA (Food and Drug Administration)-approved system for detecting and enumerating circulating tumor cells (CTCs) in patients with metastatic breast, prostate, and colorectal cancer. This label-based technique is based on the presence of epithelial cell adhesion molecule (EpCAM) on CTCs to selectively identify and isolate them from other blood components.

The process begins with the collection of a patient's blood sample, which is incubated with magnetic nanoparticles coated with anti-EpCAM antibodies. These nanoparticles bind specifically to EpCAM-expressing cells, allowing for their separation through an immunomagnetic enrichment step. Once isolated, the captured cells undergo fluorescent staining to enable their identification. Markers such as cytokeratins (*CK* 8, 18, and 19), which are characteristic of epithelial cells, are used to confirm the presence of CTCs, while a nuclear stain (DAPI) highlights intact cells. Additionally, an anti-CD45 antibody is included to exclude leukocytes, since they express CD45, unlike circulating tumor cells (CTCs), ensuring that only true tumor cells are analyzed.[41]. Following staining, the sample is processed by the CellTracks® Analyzer, an automated fluorescence microscope that scans and captures images of the labeled cells. The platform applies stringent criteria for CTC identification, recognizing only nucleated, EpCAM-positive, cytokeratin-positive, and *CD45*-negative cells as true CTCs. This approach provides a highly specific and reproducible method for CTC detection, making it valuable for both clinical and research applications.

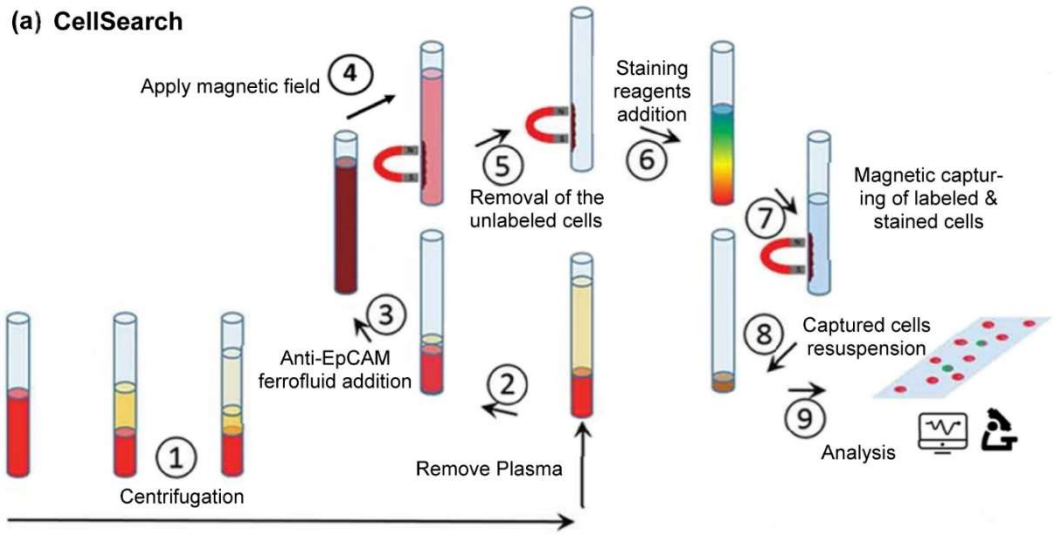

Figure 3. The CellSearch® procedure involves centrifuging a 7.5 mL blood sample to remove the plasma, followed by the addition of anti-EpCAM ferrofluid. The sample is then incubated within a magnetic field to isolate EpCAM-positive cells, which are subsequently analyzed[42].

However, despite its advantages, CellSearch® has limitations: since it relies on EpCAM expression, it may fail to detect CTCs that have undergone epithelial-to-mesenchymal transition (EMT), a process in which tumor cells lose epithelial markers and acquire mesenchymal features[43]. As result, some CTC populations, particularly those with greater metastatic potential, may be undetected. Additionally, another disadvantage is that once the CTCs are isolated and identified, they cannot be recovered for further molecular or functional analyses, limiting their use in more detailed studies[44].

1.2.2. Label-Free Techniques

Label-free techniques represent an alternative approach to circulating tumor cell (CTC) isolation that does not depend on specific molecular markers[45]. In fact, these methods use the intrinsic physical and mechanical

properties of CTCs, such as cell size, deformability, density, electric charge, and dielectric behavior to distinguish them from normal blood cells. This strategy allows for the capture of a broader and more heterogeneous population of CTCs, including those that have lost epithelial markers during EMT[46].

Historically, label-free approaches gained interest as researchers recognized the limitations of molecule-based systems in detecting all CTC subtypes. Technologies such as filtration, inertial microfluidics, acoustophoresis, and electrophysiological-based separations have been developed to enrich and isolate CTCs without the need for prior labeling[47]. These techniques often preserve cell integrity, allowing downstream analyses and biological assays. In the context of label-free isolation of circulating tumor cells (CTCs), separation methods can be broadly categorized into passive and active techniques (Figure 4), based on whether or not external forces are applied during the sorting process.

Passive methods use the intrinsic physical characteristics of CTCs, such as size, shape, and deformability, through the design and geometry of microfluidic channels. These systems rely exclusively on hydrodynamic forces and do not require external fields. Common passive approaches include filtration[47], where CTCs are retained by porous membranes due to their larger size; deterministic lateral displacement (DLD), which separates cells based on size as they flow past an array of micro-posts[48]; and inertial microfluidics[49], where cells are directed into distinct streamlines due to differences in inertial lift forces. Passive systems offer the advantages of simplicity, scalability, and continuous flow operation. However, they may suffer from limited selectivity, especially in cases

where CTCs exhibit physical properties similar to those of certain blood cells[50].

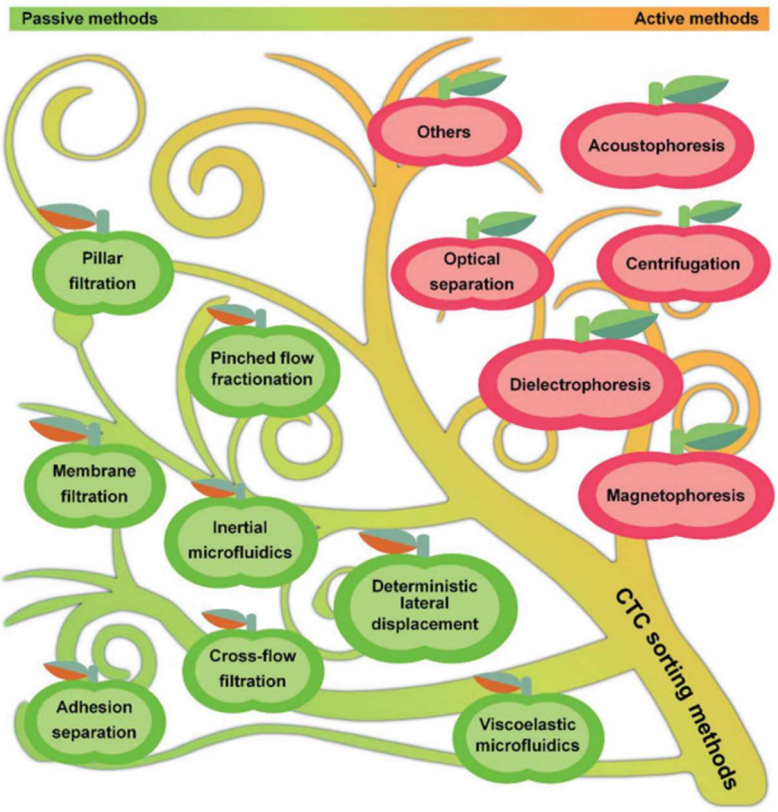

Figure 4. Different CTC label-free techniques actually used[45].

Active methods, in contrast, utilize externally applied forces, such as electric, magnetic, acoustic, or optical fields to manipulate and separate cells based on their dielectric, magnetic, or acoustic properties. Notable active techniques include dielectrophoresis (DEP)[51], which uses non-uniform electric fields to induce differential movement of cells according to their polarizability; acoustophoresis[52], which leverages ultrasound standing waves; and magnetophoresis[53], which employs magnetic fields, often in combination with magnetic labeling. These methods generally provide higher specificity and tunability, and allow the isolation of CTCs independent of size, making them suitable for capturing phenotypically

diverse or rare subpopulations. Nonetheless, active systems tend to be more complex, requiring precise control of field parameters and often exhibiting lower throughput compared to passive devices.

1.2.2.1. The ApoStream® System

Among the active, label-free approaches for the isolation of circulating tumor cells (CTCs), the ApoStream® platform represents an advanced application of continuous-flow dielectrophoresis (DEP)[54]. The core principle of this technology relies on exposing cells to a non-uniform, high-frequency electric field within a microfluidic environment. Under these conditions, each cell acquires an induced dipole moment, the magnitude and direction of which depend on the relative conductivity and permittivity of both the cell and the surrounding medium[55]. The resulting dielectrophoretic force acts perpendicular to the direction of fluid flow and causes differential displacement of cells within the channel (Figure 5). CTCs, which display distinct dielectric properties compared to normal blood cells, particularly in terms of membrane integrity, size, and internal composition, can be selectively separated and enriched[56]. Unlike static or batch DEP systems, ApoStream® operates in a continuous-flow mode, enabling the direct processing of clinically relevant blood volumes (typically 7.5 mL)[54]. The procedure is conducted without the use of antibodies or fluorescent labels, allowing the recovery of viable and functionally intact cells, suitable for downstream molecular analyses or ex vivo culture. This technology stands out for its high specificity in enriching rare cellular subpopulations, including CTCs with non-epithelial or mesenchymal-like phenotypes, which are often missed by marker-based capture systems[51].

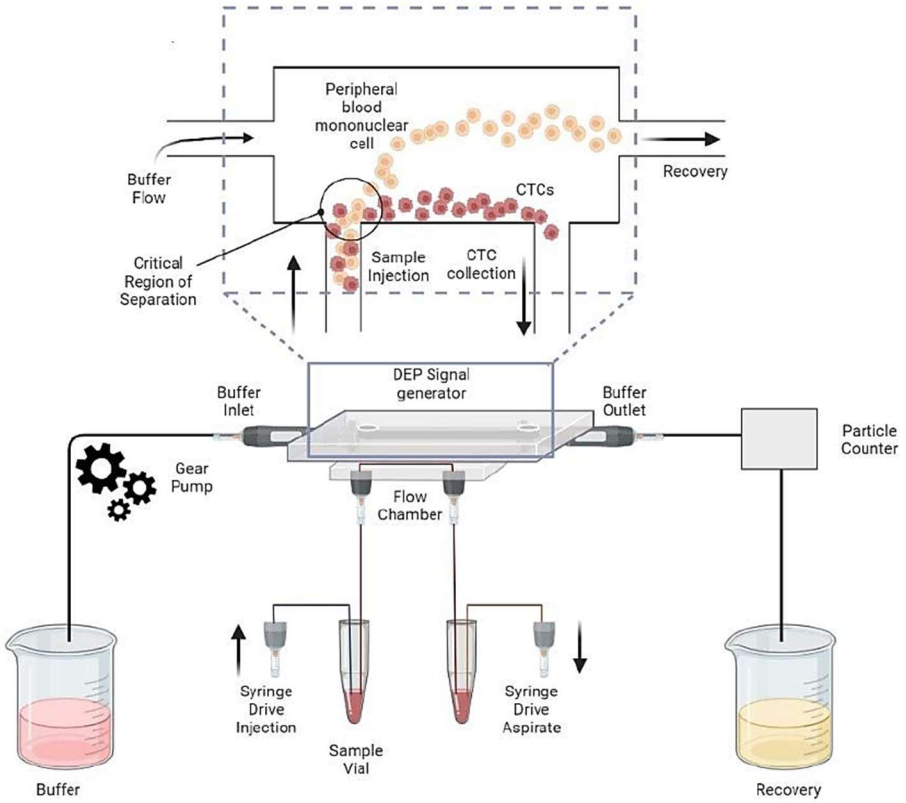

Figure 5. Side view schematic of the ApoStream® device showing the complex multi-inlet, multioutlet and microfluidic system [51].

In conclusion, it is clear that while label-free techniques offer promising approaches for cellular analysis, they often encounter challenges about sensitivity and resolution, particularly in complex biological environments where precise differentiation is crucial[33]. These limitations become even more apparent in the context of early diagnosis, where the ability to detect cellular changes can significantly impact clinical outcomes[7]. In this regard, dielectrophoresis (DEP) and its variation electrorotation (ER) represent a step forward in the pursuit of more reliable and accurate diagnostic tools[57]. These techniques not only overcome some of the limitations of traditional label-free methods but also provide a unique ability to manipulate and characterize cells based on their dielectric properties. By enabling more precise separation and analysis of

different cell types without the need for external labeling, DEP and ER stand out as particularly promising for early-stage disease detection, offering a higher level of specificity and sensitivity that is crucial for timely diagnosis.

1.3. DIELECTROPHORESIS and ELECTROROTATION

Dielectrophoresis (DEP) and electrorotation (ER) are closely related electrokinetic phenomena that exploit non-uniform electric fields to manipulate and characterize particles or cells based on their dielectric properties. In DEP, the non-uniform electric field generates a gradient of force that acts on particles or cells with varying dielectric properties, causing them to move towards areas of higher or lower field intensity depending on their polarizability[51,58–60]. The movement is governed by the interaction between the induced dipole moment of the particles and the spatially varying electric field (Figure 6). The behavior of particles in DEP can vary depending on whether they are more or less polarizable than the surrounding medium, leading to two distinct types of DEP: Positive DEP and Negative DEP[51].

In Positive DEP, particles are attracted to regions where the electric field is strongest. This occurs when the particle is more polarizable than the surrounding medium. Essentially, when an electric field is applied, it induces a dipole in the particle. If the particle's ability to polarize (its polarizability) is higher than that of the surrounding medium, it will be attracted towards areas where the field gradient is most intense. The reason behind this attraction is that the stronger field in these regions generates a stronger force on the particle, pulling it toward the high-field zones. This

principle is particularly useful when you want to trap or concentrate particles, such as in microfluidic applications, where it's crucial to direct particles towards specific locations for further analysis or manipulation.

On the other hand, in Negative DEP, particles are repelled from regions of high electric field strength. This happens when the particle is less polarizable than the surrounding medium. In this case, the particle's dipole moment is weaker compared to the medium's dipole, causing it to be pushed away from regions with stronger electric fields. Repulsive force occurs because the particle behaves in a way that the non-uniform electric field exerts a force on it that drives it toward areas where the field is weaker. Negative DEP is particularly useful for separating particles with different polarizabilities. For example, it can be used to isolate particles with lower polarizability from a mixture, which can be valuable in applications like sorting cells or separating biomolecules in a more controlled manner.

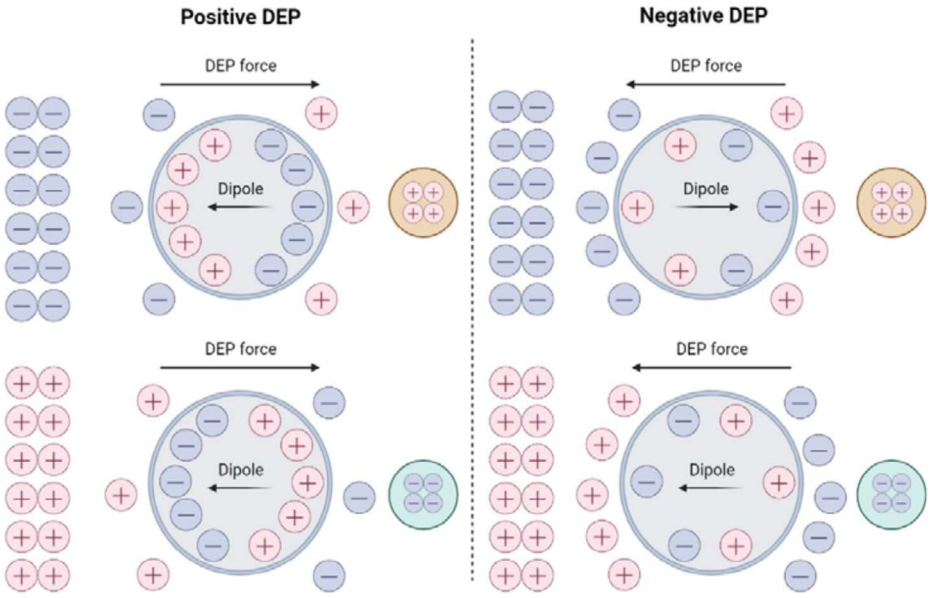

Figure 6. The direction of the net dipole and dielectrophoretic force induced by polarization for a particle that is (left) more polarizable than the surrounding medium and (right) less polarizable. The top and bottom represent two opposing configurations of the background electric field[51]

The ability to control this movement makes DEP a powerful tool for applications such as cell separation, particle manipulation, and the isolation of specific subpopulations in heterogeneous samples, such as circulating tumor cells or micro-organisms (Figure 7).

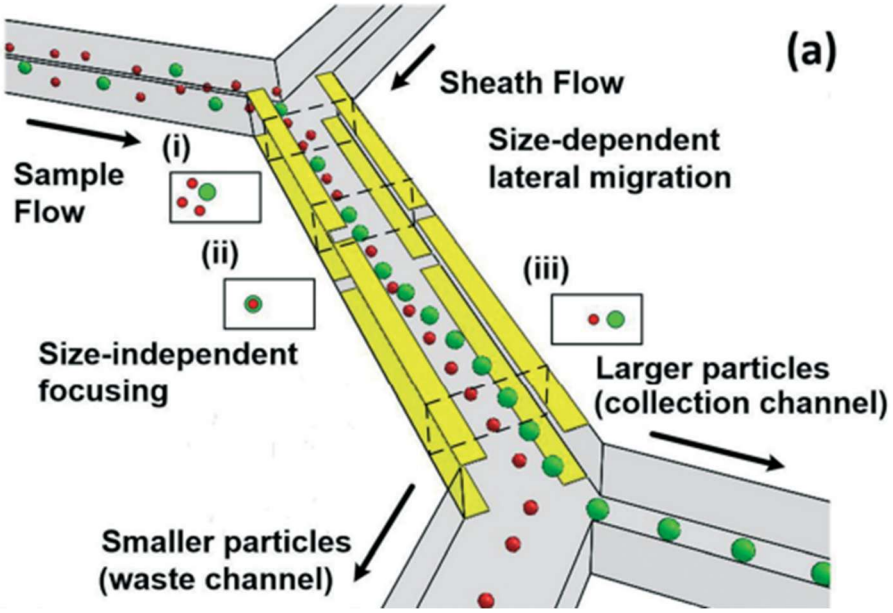

Figure 7. A schematic of a DEP separation platform. In the first stage (i), all particles, regardless of their size differences, are focused into a single stream in three dimensions within a continuous flow, ensuring that particles of varying sizes enter the second stage at the same reference position (ii). In the second stage, the particles migrate to a new focused position under altered electric boundary conditions. Due to the varying DEP forces acting on particles of different sizes, they migrate at different speeds, allowing them to be sorted and collected (iii)[61].

Electrorotation, a specific case of dielectrophoresis, involves the application of a rotating electric field to induce the rotation of particles or cells around their axis[57,62]. The rate and direction of this rotation are dependent on the particle's dielectric properties, including its permittivity and conductivity, as well as the frequency and magnitude of the applied electric field[63]. The rotational behavior of particles provides valuable insights into their dielectric properties, including membrane integrity, cell

viability, and internal structure. Unlike DEP, which induces translational movement, electrorotation focuses on rotational motion, offering a means to characterize cellular and particle characteristics without significantly altering their spatial position[64].

Both techniques are based on the fundamental principles of dielectrophoresis but differ in the nature of the resulting forces and the type of motion they induce. DEP is primarily used for particle separation and manipulation in microfluidic systems, while electrorotation is utilized to probe the dielectric properties of particles and cells at the individual level. Together, these techniques offer complementary approaches for investigating cellular behaviors, characterizing the dielectric properties of biological materials, and conducting high-precision micro-manipulations in the fields of biomedical diagnostics, biosensing, and biotechnology. In this work, we chose to use electrorotation rather than dielectrophoresis because electrorotation provides more detailed insights into the dielectric and morphological properties of cells. This technique enables a deeper analysis of intracellular electrophysiological characteristics, such as membrane conductivity and cytoplasmic permittivity. Specifically, for discriminating between different cell lines or identifying pathological states, electrorotation offers a richer and more distinctive “profile,” facilitating more precise cell characterization.

1.3.1. State of Art of DEP and ROT in Diagnostic Applications

In recent years, dielectrophoresis (DEP) and electrorotation (ROT) techniques have gone through significant advancements in the field of diagnostic applications. These electrokinetic methodologies, using the intrinsic dielectric properties of cells, offer label-free approaches for the manipulation, separation, and characterization of biological particles, proving particularly promising for early diagnosis and monitoring of various diseases.

For example, several works used DEP for early detection of bacteria in blood sample with subsequent PCR confirmation [65–67], broaden techniques against sepsis. Table 1 reports some of the techniques employed until now for this aim.

Table 1. Overview of microfluidic-based diagnostic techniques for the detection of various pathogenic bacteria. The table summarizes the pathogens investigated, the employed microfluidic and biosensing techniques, the corresponding limits of detection (LOD), and the relevant literature references.

Pathogen involved	Employed Technique	LOD	Reference
Escherichia coli	Impedimetric microfluidic sensor with antibody-modified surfaces	10^2 CFU/mL	[68]
Listeria monocytogenes	Microfluidic PCR with immunomagnetic separation	10^1 CFU/mL	[69]
Salmonella Typhimurium	Immunomagnetic enrichment + PCR in microfluidic chip	1 CFU/reaction	[70]
Staphylococcus aureus	On-chip immunoassay with fluorescence detection	10^2 CFU/mL	[71]
Mycobacterium tuberculosis	Loop-mediated isothermal amplification (LAMP) on chip	10 CFU/reaction	[72]
Vibrio cholerae	Microfluidic qPCR with pre-concentration	10 CFU/mL	[73]

Shigella spp.	Electrochemical detection on antibody-coated electrodes	10^2 CFU/mL	[74]
Clostridium difficile	Integrated LAMP in microfluidics	10^1 CFU/reaction	[75]

Similarly, these techniques have already been extensively studied and refined for the diagnosis and analysis CTCs[76] in different samples. As demonstrated by Gascoyne et al.[77], various cell types respond differently to DEP fields due to differences in their membrane capacitance, cytoplasmic conductivity, and morphological features. In fact, circulating tumor cells (CTCs) exhibit dielectric characteristics that are distinct from those of hematologic cells, allowing for effective separation in heterogeneous samples such as blood. This frequency-dependent behavior enables fine-tuned separation and has been successfully applied to the label-free isolation of viable CTCs, with significant implications for early cancer diagnosis and prognosis. Table 2 summarizes some of the most representative studies that employed DEP for the detection and separation of CTCs, highlighting the investigated cell types, techniques used, and the corresponding limits of detection (LOD).

Table 2. Summary of selected studies employing dielectrophoretic techniques for the detection and isolation of circulating tumor cells (CTCs). The table includes the type of cancer cell investigated, the specific DEP approach applied, and the reported limit of detection (LOD). References refer to the original publications.

Cell Type Investigated	**Employed Technique**	**LOD (Limit of Detection)**	**Reference**
MDA-MB-231 (Breast cancer)	Insulator-based DEP (iDEP)	~10 cells/mL	[78]
PC-3 (Prostate cancer)	Contactless iDEP (c-iDEP)	~1 cell/μL	[79]
A549 (Lung cancer)	3D-electrode DEP	10 cells in 1 mL	[80]

SW620 (Colorectal cancer)	Microfluidic DEP with 3D posts	1–10 cells/mL	[81]
SKOV-3 (Ovarian cancer)	Gradient DEP	5 cells/mL	[82]
MCF-7 (Breast cancer)	DEP-Biochip	1–100 cells/mL	[83]
HeLa (Cervical cancer)	3D-electrode array DEP	10 cells/mL	[84]
Mixed CTCs from patient blood	iDEP + Pre-enrichment step	~1 cell/mL (after enrichment)	[85]

1.4. AIM of THE WORK

It is clear that in recent years, there has been a growing interest in label-free techniques for cell characterization, as they allow the study of living cells without the need for exogenous markers that may alter their physiology, and making the cells useful for further downstream analysis. Despite their potential, these approaches often face limitations related to buffer compatibility, sensitivity to cellular complexity, and reproducibility across different cell types. In this context, electrorotation (ROT) has emerged as a promising method, as it integrates information on both membrane properties and intracellular organization, providing a complete dielectric fingerprint of cells. However, the application of ROT has been constrained by the lack of standardized, biocompatible experimental conditions and by the need for systematic correlations with molecular and functional markers.
Building on these premises, the aim of this three-year PhD project can be summarized in three key objectives (Figure 8):

1. To formulate and validate a bio-electrochemically suitable buffer for electrorotation experiments, ensuring the survival of cells before, during, and after exposure. Particular attention was dedicated to metabolic compatibility, osmolarity, and morphological stability[86].

2. To characterize twelve human cell lines (Table 3), both healthy and tumorigenic, from four distinct tissues, using a novel electrorotation device developed at the Departments of Computer and Electronic Engineering of the University of Catania. The rotational velocity

was investigated across a broad frequency spectrum, with low-frequency ranges reflecting membrane properties and high-frequency ranges probing the cytoplasm.

Table 3. Summary of the cell lines used in this study, their tissue origin, and main biological or clinical relevance.

Cell Line	Tissue Origin	Type / Main Application
184A1	Mammary epithelium	Non-tumorigenic breast epithelial line; physiological control for breast models
MCF-7	Mammary gland	Luminal A breast cancer line; model for hormone-responsive, low-aggressiveness tumors
MDA-MB-231	Mammary gland	Triple-negative breast cancer line; model for highly invasive and metastatic phenotype
PWR-1E	Prostate epithelium	Normal prostate epithelial line; non-tumorigenic control
LNCaP	Prostate	Androgen-sensitive prostate adenocarcinoma; model of early-stage prostate cancer
PC-3	Prostate (bone metastasis)	Androgen-independent metastatic prostate cancer line; aggressive phenotype
CCD-841 CoN	Colon epithelium	Normal human colon epithelial line; non-tumorigenic reference
CaCo-2	Colon (adenocarcinoma)	Moderately differentiated colorectal cancer line; model for intestinal barrier and tumor polarity
HCT-116	Colon (carcinoma)	Microsatellite-unstable colorectal carcinoma; model for aggressive, high-proliferation tumors
HCC1937 BL	Peripheral blood (B-lymphocytes)	Epstein–Barr virus–transformed lymphoblastoid line; model for B-cell activation and transformation
U266	Bone marrow (plasma cells)	Multiple myeloma line; secretory, suspension cell model
HDLM-2	Lymph node (Hodgkin lymphoma)	Hodgkin lymphoma line with Reed–Sternberg–like morphology; suspension model for hematologic neoplasms

3. To explore possible correlations between electrorotation profiles and the expression of genes involved in nuclear and cytoskeletal organization. In particular, the study focused on *BANP* (BTG3 Associated Nuclear Protein) and *PTK2* (protein tyrosine kinase 2), testing their potential as molecular predictors of dielectric behavior.

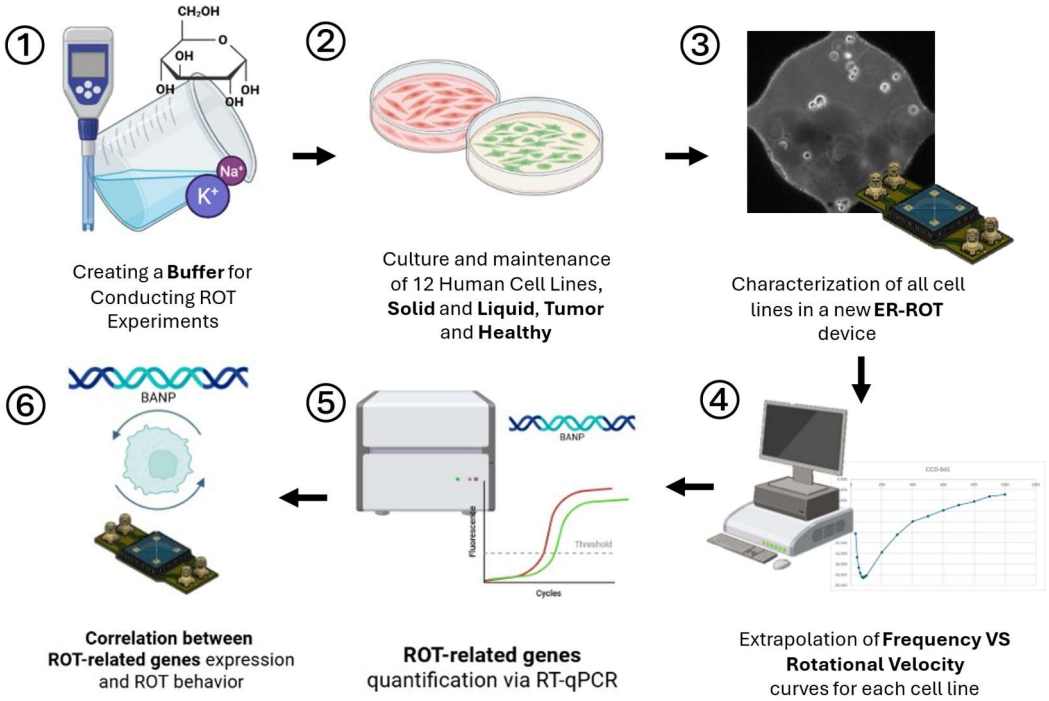

Figure 8. Overview of the experimental workflow developed during the PhD project, which included the following main steps:

1) the formulation of a buffer suitable for conducting experiments while ensuring cell viability; 2) the maintenance and preparation of 12 human cell lines derived from breast, prostate, colorectal tissue, and blood; 3) the performance of electrorotation on all 12 cell lines; 4) the extraction of each cell line's rotational behavior under different frequencies, with velocity calculated through a dedicated algorithm; 5) the quantification, via RT-qPCR, of genes considered potentially related to the distinct electrorotational responses; 6) the verification of correlations between electrorotation velocity and the expression of the aforementioned genes.

2. MATERIALS

2.1. EFFECTS OF BUFFER FORMULATION ON CELL BEHAVIOR

2.1.1. Buffer Composition

To find the best formulation for a buffer that would allow cell survival during Electrorotation (ROT) experiments and at the same time minimize parasitic effects, four formulations (Table 4) were tested.

Table 4. The four buffers employed in this investigation and their chemical makeup. Ultra-Pure MilliQ® Water was used to prepare each buffer.

Buffer 1	**Buffer 2**	**Buffer 3**	**Buffer 4**[87]
1X phosphate buffered saline (PBS) pH 7.0, 1%;	1X FBS, 2%;	Sucrose 9.5%;	Sucrose 9.5%;
1X fetal bovine serum (FBS), 2%;	Sucrose 9.5%;	Dextrose 0.1 mg/mL;	Dextrose 0.1 mg/mL;
0.1% bovine serum albumin (BSA), 2%.	Glucose 0.1 mg/mL;	0.1% BSA, 2%.	0.1% BSA, 2%.
Tested conductivity: 33 mS/m	0.1 BSA, 2%.	1X PBS pH 7.0, 1%;	1X PBS pH 7.0, 1%;
	Tested conductivity: 58 mS/m	$(CH_3COO)_2Ca$ 0.1 mM.	$(CH_3COO)_2Ca$ 0.1 mM.
		Tested conductivity: 296 mS/m	Tested conductivity: 33 mS/m

All chemicals were supplied by Merck (Merck KGaA, Darmstadt, Germany) unless specified otherwise. All the reagents and chemicals used in the present study were of analytical grade. Once prepared, all buffers were filtered using a Millex syringe filter with 0.22 μm pores (Millipore, Biosigma S.p.A., Cona, Italy). The conductivity of Buffer 1 and Buffer 4 was adjusted to 33 mS/m, one of the most commonly used values[88] by adding a 0.1 mM potassium chloride (KCl) solution. This value is below the typical cell cytoplasmic conductivities (1 S/m) to facilitate DEP manipulation of the cells[87]. Conductivity measurements were performed with a DDS-307 Electric Conductometer (Changzhou W&J Instrument Co., Ltd., Changzhou, Jiangsu, China). The best-performing buffer turned out to be Buffer 4, that is a slightly modification of a buffer already present in literature[87]. This clarification is important because, throughout the study, Buffer 4 is also referred to as Buffer DEP. The name 'Buffer 4' was used during the compatibility testing phase, while the designation 'Buffer DEP' was adopted after it was identified as the most effective option.

2.1.2. Evaluation of Buffers compositions on cell viability

To perform cell viability experiments, Caco-2 cells (HTB-37™; human colorectal adenocarcinoma, American Type Culture Collection, Manassas, VA, USA) were cultured in Dulbecco's Modified Eagle Medium (DMEM) supplemented with 10% heat-inactivated fetal bovine serum (FBS), 2 mM L-glutamine, and penicillin-streptomycin (50 U/mL and 50 μg/mL, respectively). K562 cells (CCL-243™; human chronic myelogenous leukemia, ATCC) were maintained in Roswell Park Memorial Institute (RPMI) 1640 medium, also supplemented with 10%

heat-inactivated FBS, 2 mM L-glutamine, and penicillin-streptomycin (50 U/mL and 50 µg/mL). Both cell lines were grown in 25 or 75 cm^2 polystyrene culture flasks with vented caps at 37 °C in a humidified incubator with 5% CO_2 and 95% air. Although both are cancer-derived, the two cell lines differ markedly in origin and characteristics. Caco-2 cells are epithelial in nature, isolated from colon tissue of a 72-year-old White male with colorectal adenocarcinoma, while K562 cells are lymphoblast-like, derived from the bone marrow of a 53-year-old patient with chronic myelogenous leukemia. Furthermore, the two lines show a sufficiently low crossover frequency to allow comparative analysis[89]. Twenty-four hours prior to treatment, cells were trypsinized, counted using a C-Chip disposable hemocytometer, and seeded into 96-well plates at the appropriate density. The culture medium (200 µL) was then replaced with the same volume of the four buffers, and cells were incubated for 1 hour and 24 hours. At the end of each incubation period, cell viability was assessed via MTT assay, as previously described[90]. . All measurements represent the mean ± standard deviation (SD) of at least four technical replicates.

2.1.3. Discrimination Capacity Analysis

In addition to the metabolic impact, assessed via the MTT assay, we also aimed to test the effect of the new buffers on certain physical properties of the cells, such as granularity and Side Scatter (SSC), which can be understood as a measure of the internal complexity of the cells (e.g., the presence of granules or structural irregularities).

To do this, being aware that the buffers might induce even subtle differences, we first considered it important to test the sensitivity of the flow cytometer to be used for the subsequent experiments, and only then to carry out the actual experiments with abovementioned buffers.

To assess the ability of the FlowSight® Imaging Flow Cytometer (Amnis®, Millipore, Merck KGaA, Darmstadt, Germany) to distinguish cellular features in the presence of increasing saline concentrations, seven NaCl solutions (0%, 0.3%, 0.6%, 0.9%—the standard concentration used for physiological saline[91] 1.5%, 3%, and 4%) were prepared. Caco-2 cells were incubated at 37 °C for 1 hour in each of these solutions, after which they were analyzed using the FlowSight® system. This cytometer enables high-sensitivity detection of brightfield, darkfield, and fluorescence images. Image analysis was carried out using IDEAS® software (Image Data Exploration and Analysis Software), which supports robust statistical evaluation of both image intensity and a wide range of morphological parameters. Among these, two key parameters, Area and Diameter, were selected for the analysis. A total of 1000 events per concentration was recorded.

2.1.4. Flow Cytometry Sample Preparation

Caco-2 and K562 cells were centrifuged, and the supernatant was discarded. The cell pellets were resuspended in 300 µL of 1X PBS, and 100 µL of each suspension were transferred into 1.9 mL of either Buffer 1, Buffer 4, or Minimum Essential Medium (MEM) without phenol red (used as control). Aliquots were collected at five time points, T0 (0 min),

T1 (15 min), T2 (30 min), T3 (45 min), and T4 (60 min), and analyzed for circularity, area vs. diameter, and SSC, considered as rapidly responsive morphological parameters.

2.1.5. Gene Expression Analysis via RT-qPCR

To investigate the impact of Buffer 1 and Buffer 4 on gene expression, aliquots of cells treated with both buffers at T4 (120 min) and T5 (240 min), were stored in 350 µL of Buffer RLT (from the Qiamp RNeasy Mini Kit, Qiagen, Hilden, Germany) supplemented with 1% β-mercaptoethanol until RNA extraction. Quantitative real-time PCR (RT-qPCR) was conducted on previously reported time frames at which changes in target gene expression related to metabolism, oxidative stress, and inflammation become detectable [29,34]. Total RNA was extracted using the Qiamp RNeasy Mini Kit, following the manufacturer's protocol. RNA quantity and integrity were assessed using the Agilent RNA 6000 Nano Kit on the 2100 Bioanalyzer system (Agilent Technologies, Santa Clara, CA, USA)(Supplementary Table 1). Reverse transcription, amplification, fluorescence detection, and quantification were carried out using the same protocol described in references [92,93]. Gene expression was evaluated using Although no primer efficiency curves or custom melt-curve optimizations were performed in this study, all reactions were carried out using QuantiTect Primer Assays (Qiagen), which are pre-designed and laboratory-validated primer sets with manufacturer-certified amplification efficiency, specificity, and single-amplicon melt profiles. These assays undergo extensive internal QC, ensuring optimal primer performance without the need for additional experimental validation by the user. For

this reason, primer efficiency, melt-curve behavior, and amplification specificity were considered reliable as provided. QuantiTect Primer Assays were used for the following targets: β-actin (Cat. No. QT00095431), iNOS/nitric oxide synthase 2 (Cat. No. QT00100275), IL-6B (Cat. No. QT00083720), and GAPDH (Cat. No. QT01658692) (Table 5). No-template controls (NTC) were included as negative controls. Relative expression levels were calculated using the 2^−ΔΔCT method (see "Calculation of Fold-Change using the ΔΔCt method" paragraph), normalizing the threshold cycle (CT) values of target genes to those of the reference gene β-actin. All RT-qPCR reactions were performed in triplicate.

Table 5. List of primers used for quantitative real-time PCR (RT-qPCR).

Official Name	**Official Symbol**	**Alternative Titles/ Symbols**	**Detected Transcript**	**Amplicon Length**
Actin Beta	ACTB	ACTB; BRWS1; PS1TP5BP1; Beta-actin; actin; beta; actin beta	NM_001101	146 bp
Nitric Oxide Synthase 2	Nos2	iNOS; Nos-2; Nos2a;i-NOS; NOS-II; MAC-NOS	NM_010927	118 bp
Glyceraldehyde-3-phosphate dehydrogenase	GAPDH	Gapd	NM_008084 NM_001289726	144 bp
Interleukin 6	IL6	IL-6B	NM_031168	128 bp

For each target gene, relative expression values were compared among experimental groups using an ordinary one-way ANOVA, followed by post-hoc multiple comparisons where appropriate. Statistical significance was defined as $p < 0.05$.

Data are presented as mean ± standard deviation (SD) from three independent experiments.

2.1.6. Osmolarity Measurement and Statistical Analysis

The osmolarity of Buffer 1 and Buffer 4 was determined by analyzing 50 µL of each sample using a Gonotec® Osmomat® Model 030-D freezing point osmometer (ELITech Group, Logan, Utah, USA). For RT-qPCR data, statistical analysis was performed using GraphPad Prism version 8. One-way ANOVA followed by Bonferroni's post hoc test was applied for multiple comparisons. A p-value < 0.05 (two-tailed) was considered statistically significant. All experiments were conducted in triplicate or more, unless otherwise specified.

2.1.7. Impact of Conductivity on CaCo-2 Cell line

A final evaluation of the metabolic impact on the CaCo-2 cell line via MTT assay was performed by varying the conductivity of Buffer 4/DEP, which had been identified as the most suitable buffer for conducting electrorotation experiments. CaCo-2 cells were grown and seeded in a 96-well plate as described in section 2.1.2. Twenty-four hours after seeding, the culture medium was replaced with four solutions of Buffer 4/DEP at decreasing conductivity: 33 mS/m (reference), 10 mS/m, 1 mS/m, and 0.1

mS/m. The conductivity of the four buffer solutions was measured using a DDS-307 Electric Conductometer (Changzhou W&J Instrument Co., Ltd., Changzhou, Jiangsu, China). After 2 hours and 24 hours, an MTT assay was performed as described in section 2.1.2. Data obtained were analyzed using an ordinary one-way ANOVA to evaluate differences in cell viability among the experimental groups with varying buffer conductivity (33, 10, 1, and 0.1 mS/m). Statistical significance was set at $p < 0.05$. All measurements represent the mean ± standard deviation (SD) of at least four technical replicates. The CaCo-2 cell line was selected for the conductivity assays because it represents a well-established model of adherent epithelial cells and is widely used to evaluate the effects of physicochemical parameters on cell viability and membrane integrity[94,95]. Its reproducible growth pattern and robust metabolic profile made it suitable for assessing the impact of buffer conductivity prior to extending the experiments to other cell types.

2.2. ELECTROROTATION EXPERIMENTS

2.2.1. Electrorotation System

The compact and purpose-built electrorotation (ROT) system presented in this work is developed by a collaboration between the Department of Electrical Electronic and Computer Engineering (University of Catania) and STLab s.r.l. Created for automatic measurements in biological environments, the device consists of three main components: a custom quadrature amplifier (QAMP), a ROT-device composed of a dedicated

chip where the cell suspension is placed and the rotating electric field is generated, and a tailored algorithm for the automatic extraction of cell rotation data.

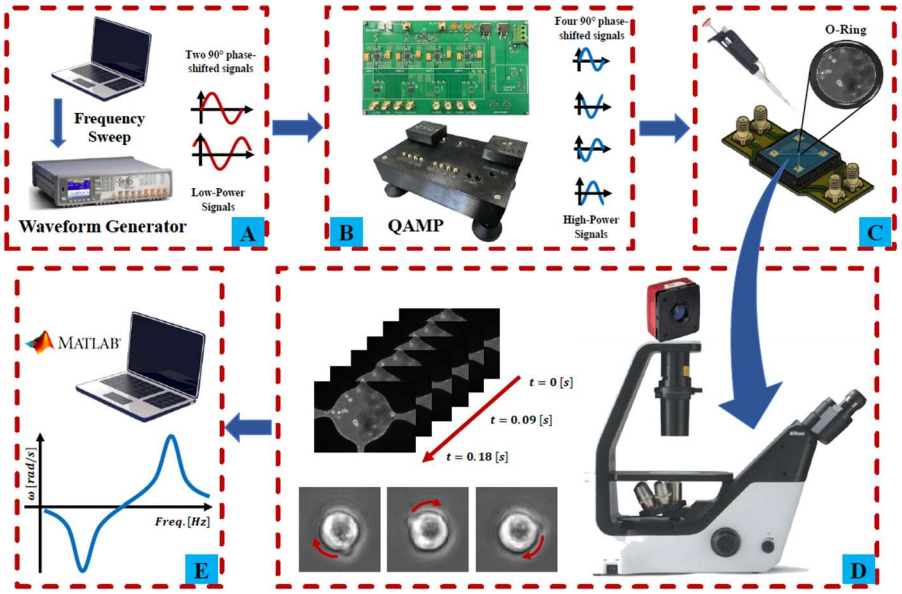

Figure 9. Working principle schematic: (A) Low-power signal generations, (B) high-power quadrature stage, (C) ROT-Device,

(D) sensing and acquisition, and (E) offline analysis and result evaluation.

The operating principle is illustrated in Figure 9. A standard, low-cost waveform generator, controlled via PC, produces two low-power sinusoidal signals with a 90° phase shift, as shown in Figure 9(A). These signals are fed into the QAMP, which amplifies and converts them into four high-power sinusoidal signals in quadrature, Figure 9(B). These four signals are then connected to the ROT-device, Figure 9(C), where a rotating electric field is established by arranging the signals in a specific configuration. The biological sample is placed at the center of the device: a rubber O-ring positioned between the electrodes forms a fluidic chamber to contain the suspended cells. The cell suspension is loaded into the chamber using a calibrated pipette, and a coverslip is placed on top to seal

the chamber and reduce cell movement. The ROT-device is then inserted under a microscope, and cell rotation is monitored via a digital camera, Figure 9(D). A custom script running on the PC handles the initial setup of the waveform generator, defining the amplitude, starting frequency, and phase shift between the two sinusoidal signals. Once the initial parameters are set, the script initiates a frequency sweep through a cyclic routine. At each step of the cycle, the frequency of the signals is changed while keeping amplitude and phase shift constant. Each cycle is divided into three phases: the rotation phase, the resting phase, and the sweep phase. In the rotation phase, the sinusoidal signals are active (non-zero amplitude), inducing cell rotation for a duration t_1. During the resting phase, the signal amplitude is set to zero for a time t_2, effectively nullifying the rotating electric field ($\langle \Gamma ROT \rangle = 0$) and stopping cell rotation. This pause is essential to automate the analysis, as it marks the precise moments when frequency changes occur. Finally, in the sweep phase, the signal frequency is adjusted to explore the full electrorotation spectrum. For each frequency, a set of image frames is acquired and stored. Once the sweep is complete, the recorded frames are processed by the custom algorithm to automatically extract the characteristic electrorotation curve of the cells, Figure 9(E).

2.2.2. Electrorotation Device and Microchip Design

The ROT-device consists of a custom-designed printed circuit board (PCB) optimized to reduce parasitic capacitance, thereby enabling efficient high-frequency operation, along with a specially engineered, glass-based ROT microchip, as illustrated in Figure 10(A). The PCB is

designed to facilitate both the handling of the microchip and the electrical interfacing, providing four RF coaxial connectors for signal transmission between the QAMP and the microchip electrodes. The ROT microchip features four metallic electrodes patterned on a glass substrate, defining a central circular region with a radius of 200 µm, the area where the rotating electric field is established. To minimize non-uniformities in the field and reduce dielectrophoretic (DEP) forces that could cause the cells to drift from the region of interest (ROI), a specific "bone electrode" configuration, as described previously[96], was implemented. The electrode layout and a photograph of the microchip are presented in Figure 10(B).

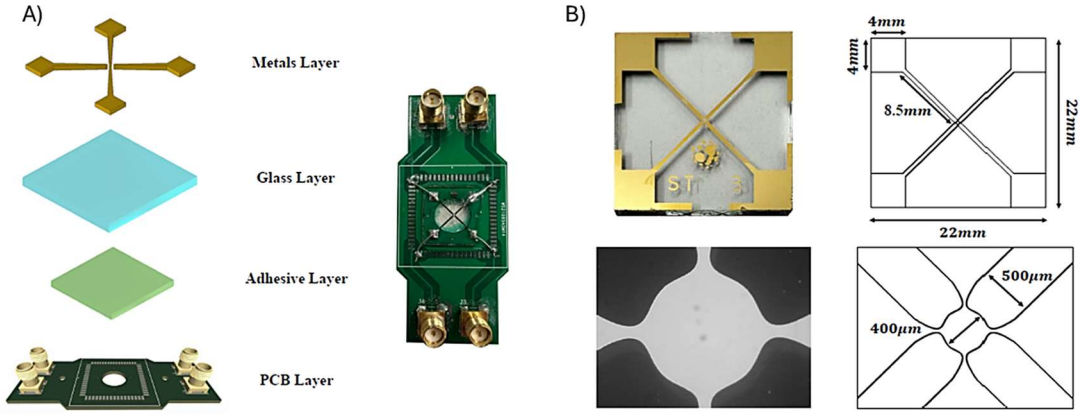

Figure 10. (A) ROT-Device Layer structure. (B) ROT-microchip dimensions and electrode geometry.

The ROT microchip was fabricated using standard photolithographic techniques[97]. The electrodes consist of a 20 nm chromium adhesion layer topped with a 100 nm gold layer, deposited on a glass substrate selected for its biocompatibility and optical transparency. The microchip was mechanically mounted onto the PCB using an adhesive layer, as shown in Figure 10(A), and the electrodes were electrically connected to the PCB via wire bonding.

2.2.3. Cell Lines Involved in Electrorotation Experiments

A total of twelve human immortalized cell lines from various tissue origins were used for electrorotation (ROT) analyses. All cell lines were cultured according to ATCC protocols and maintained at 37 °C in a humidified 5% CO_2 incubator. Culture media were supplemented with 10% fetal bovine serum (FBS) and 1% penicillin-streptomycin, unless otherwise specified. The twelve human cell lines employed in this work were selected as a representative and biologically coherent model system to support the goal of this project: the early detection and dielectric characterization of circulating tumor cells (CTCs) through electrorotation. Breast (184A1, MCF-7, MDA-MB-231), prostate (PWR-1E, LNCaP, PC-3), and colon (CCD-841 CoN, CaCo-2, HCT-116) cell lines were chosen to reproduce the epithelial origin of solid tumors that most frequently release CTCs into the bloodstream. Each tissue set includes non-tumorigenic, low-grade, and highly malignant counterparts, allowing direct comparison of dielectric properties along the tumor progression axis. This gradient provides a controlled model for understanding how malignant transformation modifies the electrorotation profile.

Hematologic cell lines (HCC1937 BL, U266, HDLM-2) were included as non-adherent systems mimicking the suspension environment encountered by CTCs in peripheral blood. Their different lineage origins (B-cell, plasma cell, and Hodgkin-type lymphoma) offer complementary insights into how cell morphology and internal organization influence dielectric behavior under flow-like conditions. All cell lines were cultured in their appropriate media formulations (e.g., DMEM or RPMI-1640) and subcultured at 70–80% confluency using 0.05% trypsin-EDTA when

adherent. ROT experiments were performed using cells in exponential growth phase.

Breast-derived cell lines (Figure 11) included 184A1 (ATCC CRL-8798), a non-tumorigenic epithelial line derived from normal mammary tissue; MCF-7 (ATCC HTB-22), a luminal breast cancer cell line; and MDA-MB-231 (ATCC HTB-26), a triple-negative breast cancer cell line.

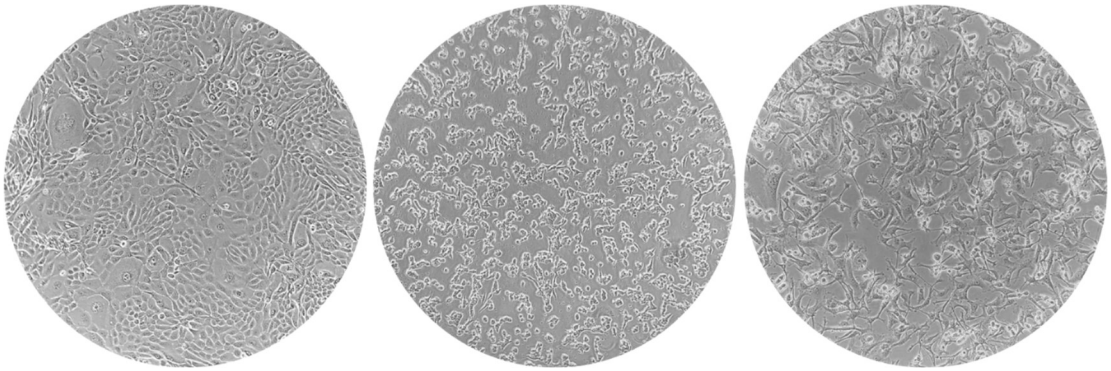

Figure 11. Breast Cell Line used in the presented work under the optical microscope at different magnifications. 184A1 (left), MCF-7 (middle) and MDA-MB-231 (right).

Prostate-derived cell lines: (Figure 12) PWR-1E (ATCC CRL-11611), a normal epithelial prostate cell line; PC-3 (ATCC CRL-1435), derived from bone metastasis of prostate adenocarcinoma; and LNCaP (ATCC CRL-1740), an androgen-sensitive prostate cancer line.

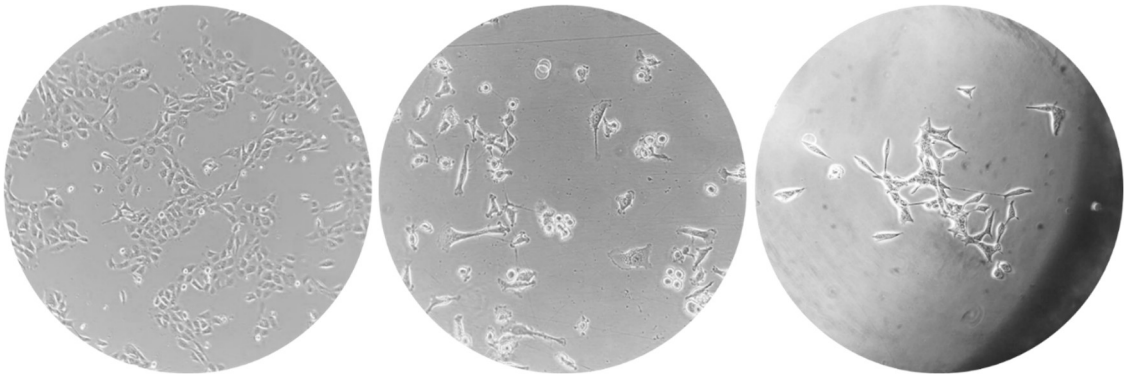

Figure 12. Prostate Cell Line used in the presented work under the optical microscope at different magnifications.
PWR-1E (left), PC3 (middle) and LnCap231 (right).

Colon-derived cell lines: (Figure 13) included CCD 841 CoN (ATCC CRL-1790), a normal human colon epithelial cell line; CaCo-2 (ATCC HTB-37), a colorectal adenocarcinoma line with enterocyte-like differentiation; and HCT-116 (ATCC CCL-247), a microsatellite-unstable colorectal carcinoma line.

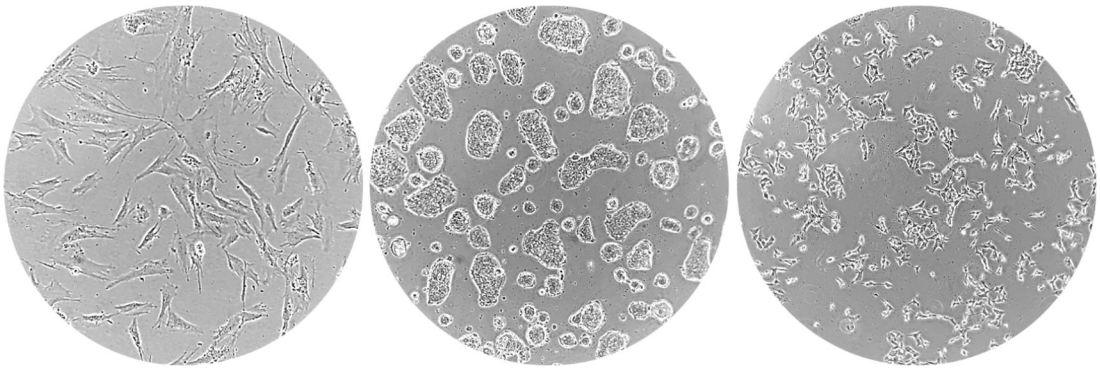

Figure 13. Colorectal Cell Line used in the presented work under the optical microscope at different magnifications.
CCD-841 (left), CaCo-2 (middle) and HCT-116 (right).

Hematologic cell lines (Figure 14) comprised HDLM-2 (DSMZ ACC-19), a Hodgkin lymphoma-derived cell line of B-cell origin; U266 (ATCC TIB-196), a multiple myeloma cell line; and HCC1937 BL (ATCC CRL-2337), an Epstein-Barr virus-transformed lymphoblastoid cell line established from peripheral blood of a BRCA1-mutated breast cancer patient.

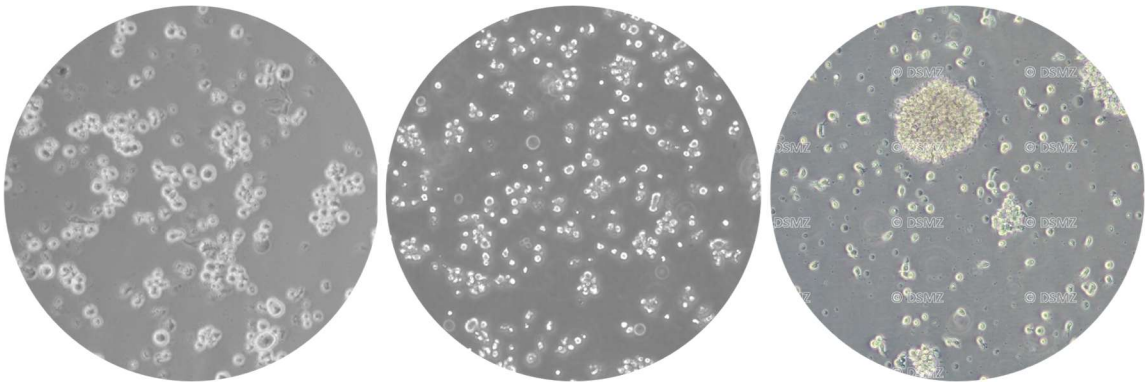

Figure 14 Hematologic Cell Line used in the presented work under the optical microscope at different magnifications.
HDLM-2 (left), U266 (middle) and HCC1937 BL (right, photo by Leibniz Institute DSMZ German Collection of Microorganisms and Cell Cultures GmbH).

2.2.4. Electrorotation Experiments[98]

Before each electrorotation (ROT) experiment, cells were prepared following a standardized workflow designed to ensure physiological stability, homogeneous suspensions, and reproducible dielectric conditions. Adherent cells were first washed by aspirating the culture medium and rinsing once with a low-conductivity DEP buffer (33 mS/m). They were then incubated for five minutes at 37 °C in the same buffer to allow a gradual adjustment to the low-ionic environment required for ROT analysis. After incubation, the buffer was removed and cells were detached using trypsin for approximately five minutes, with the detachment process monitored under a microscope. Trypsin activity was stopped by adding DEP buffer supplemented with 10% fetal bovine serum (FBS). The resulting suspension was centrifuged for five minutes at 100 × g in Eppendorf tubes and the pellet was gently resuspended in fresh DEP buffer. Cells were then counted using a hemocytometer and diluted to a final working concentration of 500 cells/µL. This concentration was selected to minimize cell–cell interactions, reduce mutual hydrodynamic interference, and ensure the presence of isolated, single cells within the ROT field of view, which is essential for reliable angular velocity extraction. For each experiment, 15 µL of the cell suspension, corresponding to approximately 2250 cells, was loaded into the measurement chamber of the ROT-device.

Suspension cell lines, such as U266, HDLM-2, or HCC1937 BL, were processed in an analogous manner. Cells were collected in 50 mL tubes, centrifuged at 1200 RPM for five minutes, resuspended in the same 33

mS/m DEP buffer, and incubated for five minutes to equilibrate. A second centrifugation step was then performed, and the final pellet was diluted to 500 cells/µL in DEP buffer adjusted to the target conductivity. The conductivity of the buffer was checked before and after each experiment to confirm the stability of the dielectric conditions. In all cases, the use of a low-conductivity medium ensured that the electric field would efficiently couple to the cell membrane while minimizing unwanted electrothermal or shielding effects.

ROT measurements were carried out using a compact, custom-built system composed of a Quadrature Signal Generator (QSG), a plug-and-play ROT-chip, and an automated image-processing algorithm for angular velocity extraction (Figure 15A). The QSG delivered four sinusoidal signals phase-shifted by 90°, with an output amplitude of up to 8 Vpp; an operating amplitude of 6 Vpp was selected as the optimal working condition after preliminary tests, as it maximized the rotational response without inducing electrolysis or excessive heating. The ROT-chip, fabricated using Cr/Au microelectrodes patterned on a glass substrate, employed a bone-electrode geometry engineered to generate a highly uniform rotating electric field in the central region of the chamber while minimizing dielectrophoretic forces. Simulations performed in COMSOL confirmed that the field non-uniformities, and therefore DEP forces, approach zero within a radius of approximately 150 µm from the geometric center. For this reason, only cells located within this region were considered suitable for analysis. The central region of the chip had a radius of 200 µm, and the electrodes were terminated with 50 Ω resistors to ensure impedance matching and preserve signal integrity over the high-frequency operating range. The chip could be reused for multiple experiments after careful rinsing with PBS and DEP buffer.

The ROT-device was mounted on an inverted phase-contrast microscope (Nikon Eclipse Ts2) equipped with a 20× objective (Figure 15A). Image acquisition was performed using a Thorlabs 340M Fast Frame CCD camera with a resolution of 640 × 480 pixels and a pixel size of 7.4 μm, connected to a computer running ThorCam™ 3.7.0. Videos were recorded at 60 frames per second (Figure 15 B). Before analysis, cells positioned outside the uniform-field region, cells touching the chamber surface, or cells showing morphological compromise were excluded to ensure analytical reliability.

A custom MATLAB script was used to control the QSG and fully automate the frequency sweep procedure. At the beginning of each experiment, the script defined the frequency vector, the amplitude of the applied signal, the rotation duration at each frequency, and the fixed resting interval between frequencies. The acquisition was organized into alternating rotation and resting phases. During the rotation phase, the rotating electric field was applied at a given frequency, and the cell's rotation was recorded. The duration of this phase, t_1, was not fixed but adapted to the cell's angular velocity, which itself depends on the applied electric field frequency. To ensure an accurate estimation of the rotational speed, it was empirically determined that each frequency step must capture at least four full rotations of the cell. Fewer rotations resulted in high variability and an increased discrepancy between estimated and actual angular velocity, whereas four or more rotations reduced the error to acceptable levels while maintaining the overall duration of the experiment within reasonable limits. Because the cell rotates faster at some frequencies than at others, t_1 varied between approximately 4 and 10 seconds across the spectrum.

Following each rotation phase, the electric field was switched off for a fixed resting interval (0.5 s), allowing the MATLAB algorithm to clearly identify the transition between successive frequencies and segment the video stream without ambiguity. A logarithmic frequency stepping strategy was used to span the range between 30 kHz and 1 MHz, enabling optimal sampling of the dielectric dispersion of the cell membrane across the β-relaxation region. The total acquisition time required to obtain a complete ROT spectrum was approximately 120 seconds, to which the time needed for cell loading and chip preparation was added. All experiments were conducted at room temperature.

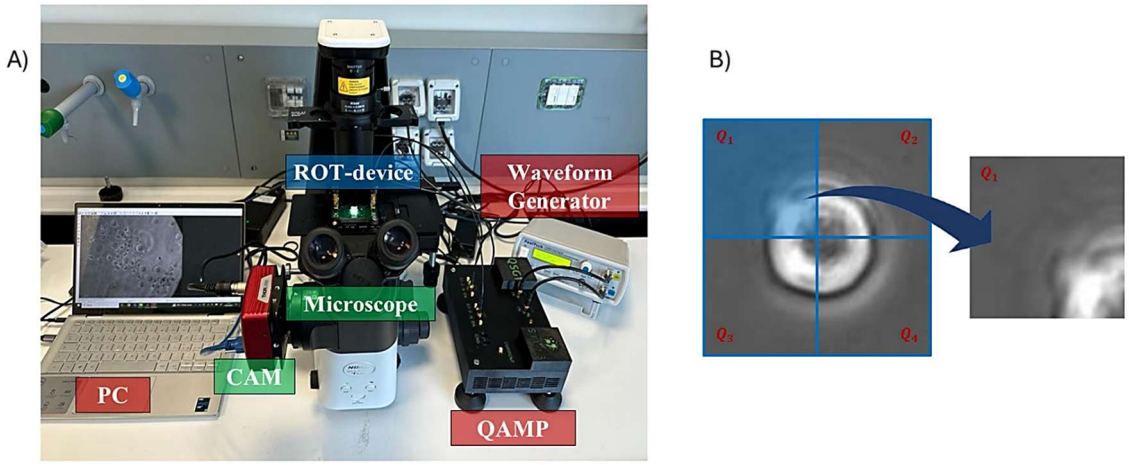

Figure 15. (A) Experimental setup for ROT experiments.
(B) Division of cell in quadrants for rotational velocity analysis after ROT experiments.

2.2.5. RT-qPCR for Electrorotation-related genes

Quantitative real-time PCR (RT-qPCR) analysis of *BANP* and *PTK2* genes expression was performed using specific QuantiTect LNA Primer Assay specific (Qiagen, Cat. No. 249990, QIAGEN GmbH)(Table 6) following manufacturer protocols. Total RNA was extracted using the RNeasy Mini Kit (Qiagen, Cat. No. 74104, QIAGEN GmbH, 40724

Hilden, Germany). Reverse transcription was carried out using the QIAGEN Reverse Transcription Kit (Cat. No. 205311, QIAGEN GmbH), according to the manufacturer's instructions. Each qPCR reaction was performed using 25 ng of cDNA per well, in a final volume prepared with QuantiTect SYBR® Green PCR Master Mix (Qiagen, Cat. No. 204143).

Table 6. Primer used for RT-qPCR performed for *BANP* and PTK2 analysis.c

Official Name	**Official Symbol**	**Alternative Titles/Symbols**	**Detected Transcript**	**Amplicon Length**	**Cat.No.**
Actin Beta	ACTB	ACTB; BRWS1; PS1TP5BP1; Beta-actin; actin; beta; actin beta	NM_001101	146 bp	249990
Associated Nuclear Protein	*BANP*	BTG3; SMAR1; BEND1; SMARBP1	NM_017869	63	
Protein Tyrosine Kinase 2	*PTK2*	PPP1R71; FAK1; FAK; FADK	NM_001358045	91	

All reactions were performed in triplicate. No-template controls (NTCs) were included to monitor potential contamination. Relative expression levels were calculated using the $2^{-\Delta\Delta CT}$ method, normalizing threshold cycle (CT) values of the target gene to those of ACTB. For each target gene, relative expression values were compared among experimental groups using an ordinary one-way ANOVA, followed by post-hoc multiple comparisons where appropriate. Statistical significance was defined as $p < 0.05$. Data are presented as mean ± standard deviation (SD) from three independent experiments.

Calculation of Fold-Change using the ΔΔCt method

Ct (Cycle threshold): Number of cycles required for the fluorescence signal of the target gene to exceed a defined threshold value (three values average).

ΔCt (Delta Ct): Difference between the Ct of the gene of interest and the Ct of the reference gene (e.g., beta-actin).

$$\Delta Ct = Ct_{target} - Ct_{ACTB}$$

ΔΔCt (Delta Delta Ct): Difference between the ΔCt of the treated (or experimental) condition and the ΔCt of the control condition.

$$\Delta\Delta Ct = \Delta Ct_{experimental} - \Delta Ct_{control}$$

Fold-Change: Relative variation of target gene expression compared to the control, calculated as:

$$2^{-\Delta\Delta Ct}$$

Interpretation:

- If the value is >1, the gene is upregulated in experimental condition.
- If the value is <1, the gene is downregulated.
- If the value is ≈1, gene expression does not change significantly.

3. RESULTS

3.1. IMPACT of BUFFER on CELL LINES

3.1.1. Impact on Cell Viability

The effects of the four different buffer formulations on the viability of Caco-2 and K562 cells at 1 h and 24 h are shown in Figure 16.

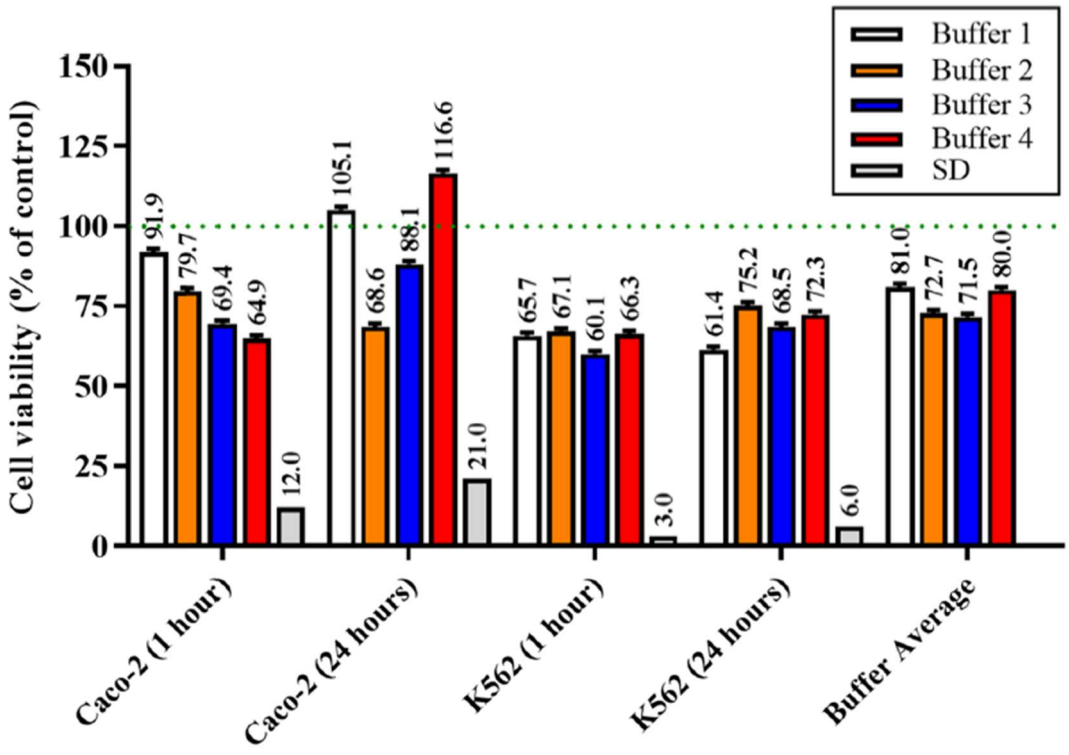

Figure 16. Caco-2 and K562 cell viability changes after one and twenty-four hours in the presence of the four tested buffers[86]. The percentage change in the absorbance at 569 nm found in cells cultured in the presence of MEM (physiological cell culture medium; dotted line) is represented by the data. SD stands for standard deviations between the four buffers under a particular circumstance; Buffer Average is the average of the four well viability (%) values that were measured for each buffer (Caco-2 at 1 and 24 hours; K562 at 1 and 24 hours).

Buffer 1 had a slight effect on Caco-2 cell viability at both time points, with values comparable to those observed in the control group (cells grown in MEM) (91.9% at 1 h; 105.1% at 24 h). Buffer 2, typically used for flow cytometry experiments, reduced Caco-2 cell viability in a time-dependent way (79.7% at 1 h; 68.6% at 24 h), suggesting that the cells suffer due to incubation with this buffer. A different effect was observed with Buffer 3; despite a decrease in cell viability at 1 h (69.4%), cells were able to recover at 24 h, with a viability value of 88.1% compared to control conditions. Interestingly, Buffer 4, which showed the greatest decrease among all buffers used at 1 h (64.9%), did not affect cell viability at 24 h, with a value even higher (116.6%) than that of control cells, indicating a full recovery within 24 h.

When considering the effects of the buffer composition on K562 cell viability at 1 h, a similar decrease in viability (~35%) was observed for all tested buffers. Unlike the Caco-2 cells, K562 cells were unable to fully recover under any of the four experimental conditions at 24 h. The smallest decrease in viability at 24 hours was observed with Buffer 2 (75.2%) and with Buffer 4 (72.3%). From this dataset, we selected Buffers 1 and 4, which had the least impact on cell viability, making them the most suitable for subsequent experiments.

3.1.2. FlowSight® Imaging Flow Cytometer Analysis

As previously mentioned, to assess the ability of the FlowSight® Imaging Flow Cytometer to discriminate cell features in solutions with increasing saline concentrations, seven NaCl solutions (0%, 0.3%, 0.6%, 0.9%, 1.5%, 3%, and 4%) were prepared, and their effects on Caco-2 cells features

were tested. For each solution analyzed, a total of 5000 events were recorded. The tool defines a cut-off by combining the "Area" and "Diameter" parameters, resulting in two populations: one in which the geometric parameters are below the cut-off (Area vs. Diameter –) and another where the values exceed the cut-off (Area vs. Diameter +). Regarding the Area vs. Diameter – population, the number of cells in this group increases with higher NaCl concentrations (Figure 17A). This is likely due to the osmotic effect, which causes water to flow from the lower concentration (inside the cells) to the higher concentration (outside the cells), resulting in a decrease in cell size (Figure 17C). This phenomenon is further supported by the data shown in Figure 17B, where a linear correlation is observed between the independent variable "NaCl concentration" and the dependent variable "Percentage of elements in the Area vs. Diameter + population."

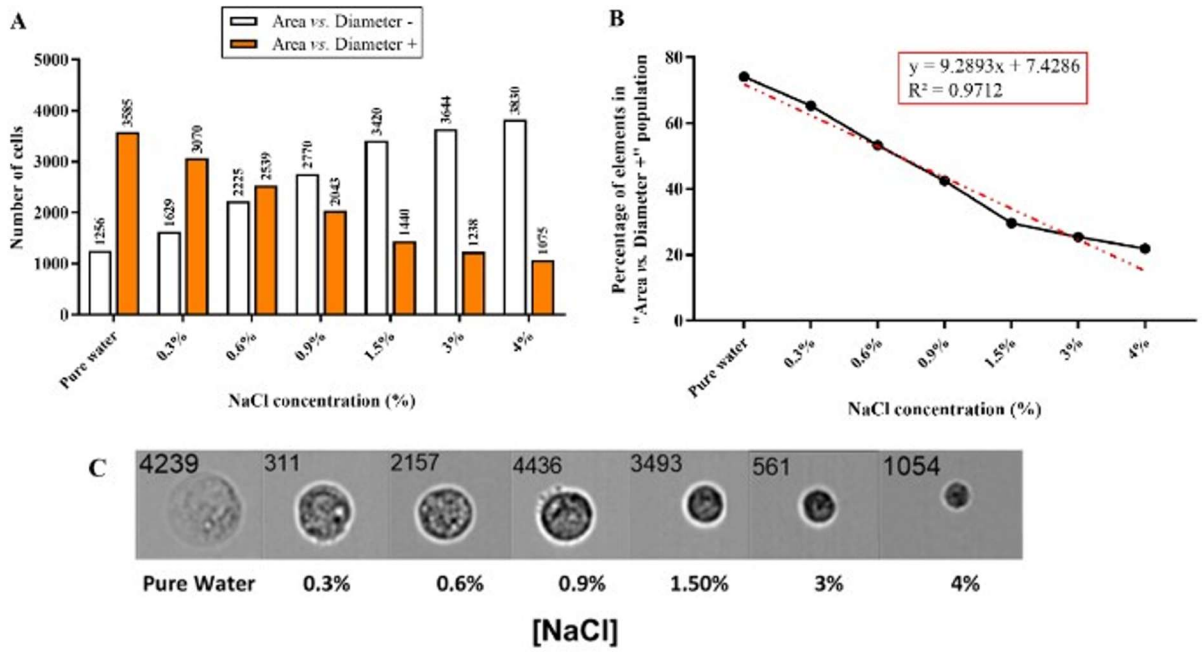

Figure 17. effects of rising NaCl concentrations on the FlowSight® Imaging Flow Cytometer's capacity to distinguish between different cell characteristics. (A) Changes in the number of cells in the "Area vs. Diameter -" and "Area vs. Diameter +" populations in relation to the concentration of NaCl. (B) Change in the proportion of elements (cells) in "Area vs. Diameter +" (a total of 5000 acquisitions) in relation to the concentration of NaCl. (C) The visive impact of the NaCl concentration on cell size.

Table 7 presents the measurements of circularity, SSC, and Area vs. Diameter for both the "Area vs. Diameter –" and "Area vs. Diameter +" populations of Caco-2 and K562 cells at various time points (from T1 to T4). The same data is also plotted in Figure 19.

Table 7. Circularity, SSC, and Area vs. Diameter parameters measurements at four different time points (T1 = 15 min, T2 = 30 min, T3 = 45 min, T4 = 60 min) in Caco-2 and K562 cells in Buffer 1, Buffer 4 and MEM. Percentages were calculated on a total of 5000 acquisitions (cells). "+" indicates population percentage above an average value, "-" indicates population percentage under the same value.

Caco-2						K562					
MEM											
		T1	T2	T3	T4			T1	T2	T3	T4
Circularity	-	13.9	15.7	13.6	16.8	Circularity	-	15.1	14.6	15.8	13.3
	+	85.9	84.3	86.3	83.1		+	84.9	85.4	84.2	86.7
SSC	-	45.9	85.5	86.1	87.7	SSC	-	97.6	97.8	97.5	98.1
	+	53.5	13.1	12.7	11.6		+	2.27	2.07	2.23	1.47
Area *vs.* Diameter	-	17.7	44.4	48.8	51.8	Area *vs.* Diameter	-	34.9	43.7	39.8	40.6
	+	78.4	50.6	46.1	44.2		+	60.9	52.9	56	55.2
Buffer 1											
		T1	T2	T3	T4			T1	T2	T3	T4
Circularity	-	11.2	9.4	6.53	7.2	Circularity	-	19.8	26.6	25	19.6
	+	88.7	90.5	93.4	92.5		+	80.2	73.3	74.9	80.2
SSC	-	89	89.4	95.8	69	SSC	-	94	92.6	90.3	92.5
	+	9.73	9.3	3.57	30.2		+	1.47	1.03	2.25	1.46
Area *vs.* Diameter	-	17.5	19.6	8.8	13.7	Area *vs.* Diameter	-	55.1	66.3	66.5	58.8
	+	70.9	68.8	69.6	69.7		+	38.3	28.1	27.3	34.7
Buffer 4											
		T1	T2	T3	T4			T1	T2	T3	T4
Circularity	-	28.1	29.8	34.6	30	Circularity	-	24.8	19	26.5	27
	+	71.9	70.2	65.4	70		+	75.2	81	73.5	73
SSC	-	72.9	70.5	62.8	64.9	SSC	-	98	97.7	97.9	98.1
	+	23.8	26.1	34.4	31.4		+	1.73	2.13	1.9	1.63
Area *vs.* Diameter	-	64.3	67	70.8	68.2	Area *vs.* Diameter	-	57.8	54.2	64.5	65.8
	+	30.9	28.3	25.4	27.7		+	38.4	41.4	32.1	30.5

As shown in Table 7 and Figure 18, the circularity and Area vs. Diameter parameters in Caco-2 cells were unaffected by incubation with Buffers 1 and 4. However, a different outcome was observed with MEM, which caused a decrease from 78.4 (T1) to 50.6 (T2), 46.1 (T3), and 44.2 (T4), likely due to the trypsinization step required for cell detachment before resuspension in one of the three solutions. Regarding SSC, this parameter was unaffected by Buffer 4, which did not notably impact cellular granularity. On the other hand, SSC increased in the presence of Buffer 1 (T4) and decreased when the cells were resuspended in MEM (T2, T3, and T4).

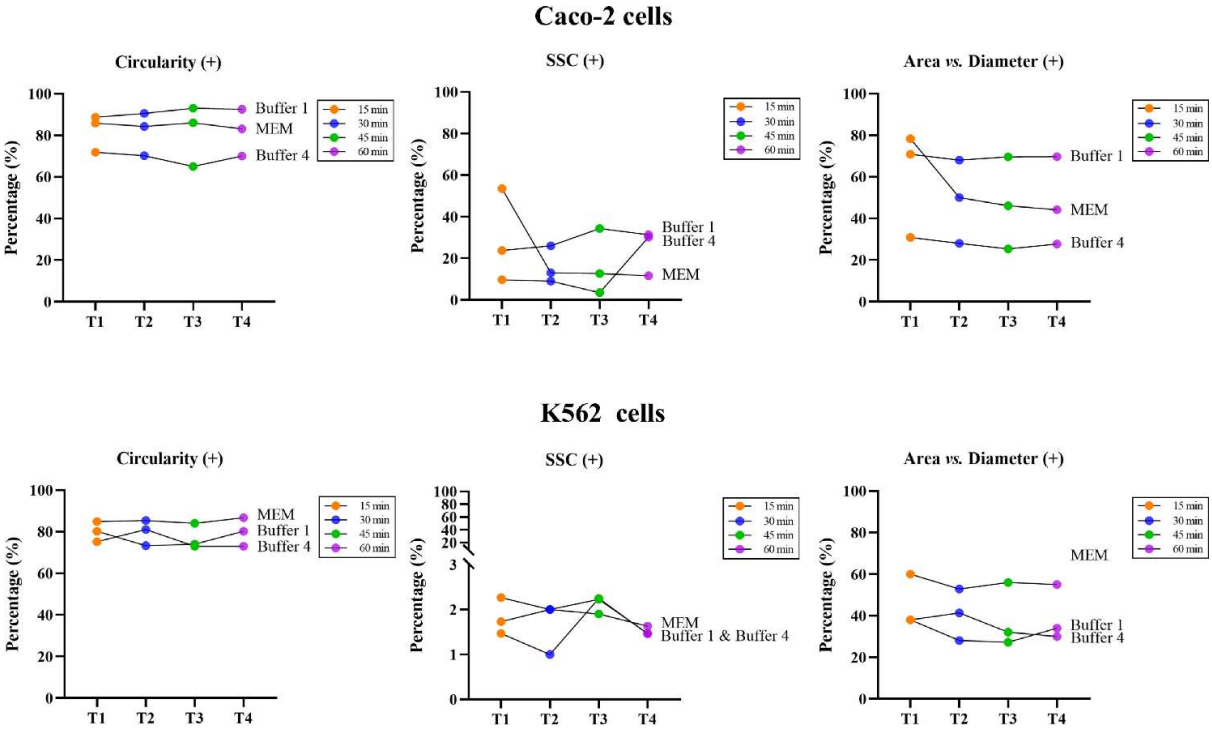

Figure 18. Circularity, SSC, and Area vs. Diameter parameters plotted at different times for both CaCo-2 and K562 cell lines.

Interestingly, at T4, both Buffer 1 and Buffer 4 resulted in the same SSC value, indicating a similar level of cell granularity. As expected, MEM, the standard medium for cell culture, produced lower SSC values compared to Buffer 1 and Buffer 4, indicating less stress. Table 7 and Figure 18 also provide the measurements for the three parameters in K562 cells. In general, K562 cells showed less sensitivity to the tested solutions. Buffer 4 did not affect particularly the circularity and SSC parameters, but a decrease in Area vs. Diameter was observed starting at T3. Some variations in the three parameters were observed at T2 and T3 for K562 cells resuspended in Buffer 1, but at T4, the values were comparable to those at T1, suggesting a transient modulation followed by a full recovery when the cells were resuspended in MEM. To better highlight the differences between the initial time point (T1) and the final time point

(T4), depending on the solution used (MEM, Buffer 1, and Buffer 4), the results were expressed as percentage differences (Figure 19).

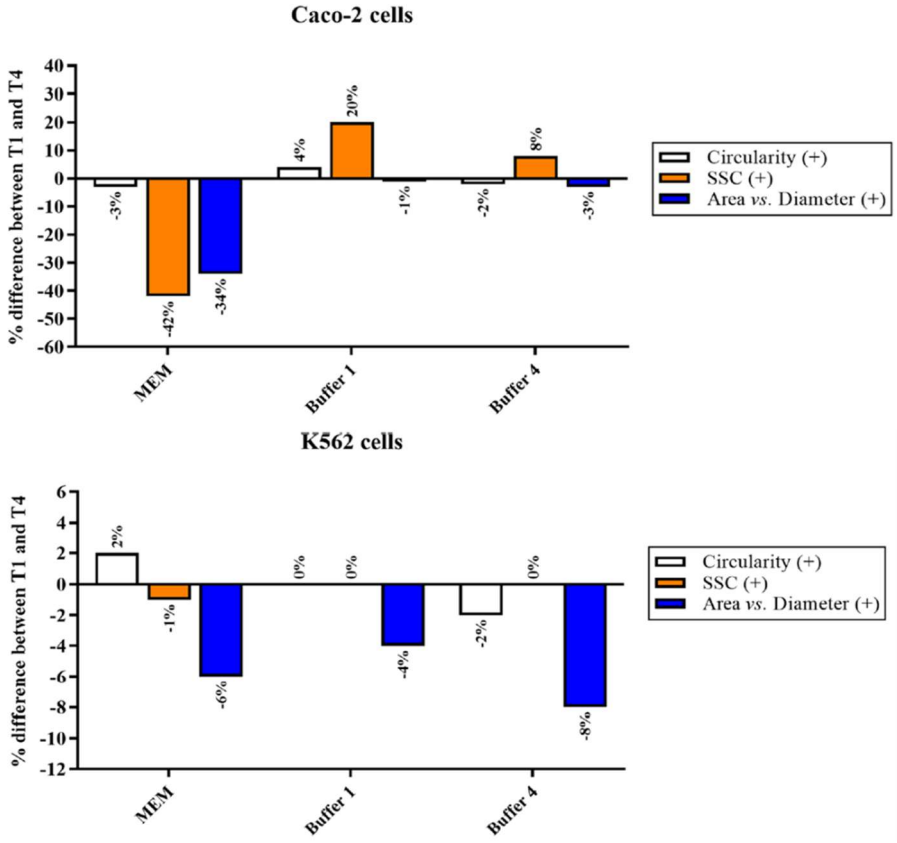

Figure 19. Percentage (%) variation of the three parameters between the initial time point (T1) and the final time point (T4) in Caco-2 and K562 cells. Each percentage was calculated using the formula: (Value at T4 – Value at T1)/100.

Figure 19 clearly illustrates that Buffer 4 is the most suitable for Caco-2 cells, while Buffer 1 should be preferred for K562 cells. Notably, for Caco-2 cells, the highest percentage difference for both circularity and SSC was observed when resuspending the cells in MEM.

3.1.3. Buffer Composition impact on Gene Expression Modulation

To evaluate how buffer composition may influence cellular stress responses and metabolic activity, we assessed the expression of GAPDH

(a marker of metabolic status), iNOS (indicative of oxidative stress), and IL-6B (a pro-inflammatory cytokine) in both Caco-2 (Figure 20A) and K562 (Figure 20B) cells when exposed to Buffer 1 and Buffer 4. Quantitative RT-PCR was performed at two time points (T4: 60 min and T5: 120 min), and expression levels were normalized to β-actin and compared to untreated controls (MEM, T0). In Caco-2 cells, Buffer 1 had minimal impact on GAPDH expression, though a slight downregulation trend was noted at T4. iNOS expression showed a transient increase at T4, returning to baseline by T5. Conversely, IL-6B levels were markedly upregulated at T5, suggesting a delayed inflammatory response. Buffer 4 induced a significant downregulation of GAPDH at both time points, alongside a pronounced but transient increase in iNOS at T4, which was followed by suppression below baseline at T5. IL-6B was significantly upregulated at both time points in cells treated with Buffer 4, indicating a more robust inflammatory response compared to Buffer 1. In K562 cells, GAPDH expression remained stable with Buffer 1 but was significantly reduced by Buffer 4 at both time points. iNOS expression decreased significantly in response to Buffer 1, while Buffer 4 also induced downregulation. Interestingly, IL-6B expression was significantly elevated by Buffer 1 at both T4 and T5, while Buffer 4 led to an upregulation at T4 only, with levels returning to baseline at T5. Overall, these data reveal that even buffers deemed non-cytotoxic based on viability assays can exert substantial and cell line-specific effects on key stress and metabolic gene pathways. These findings highlight the necessity of evaluating molecular responses to ensure that buffer selection does not inadvertently alter cell phenotype during dielectrophoretic sorting or downstream analyses.

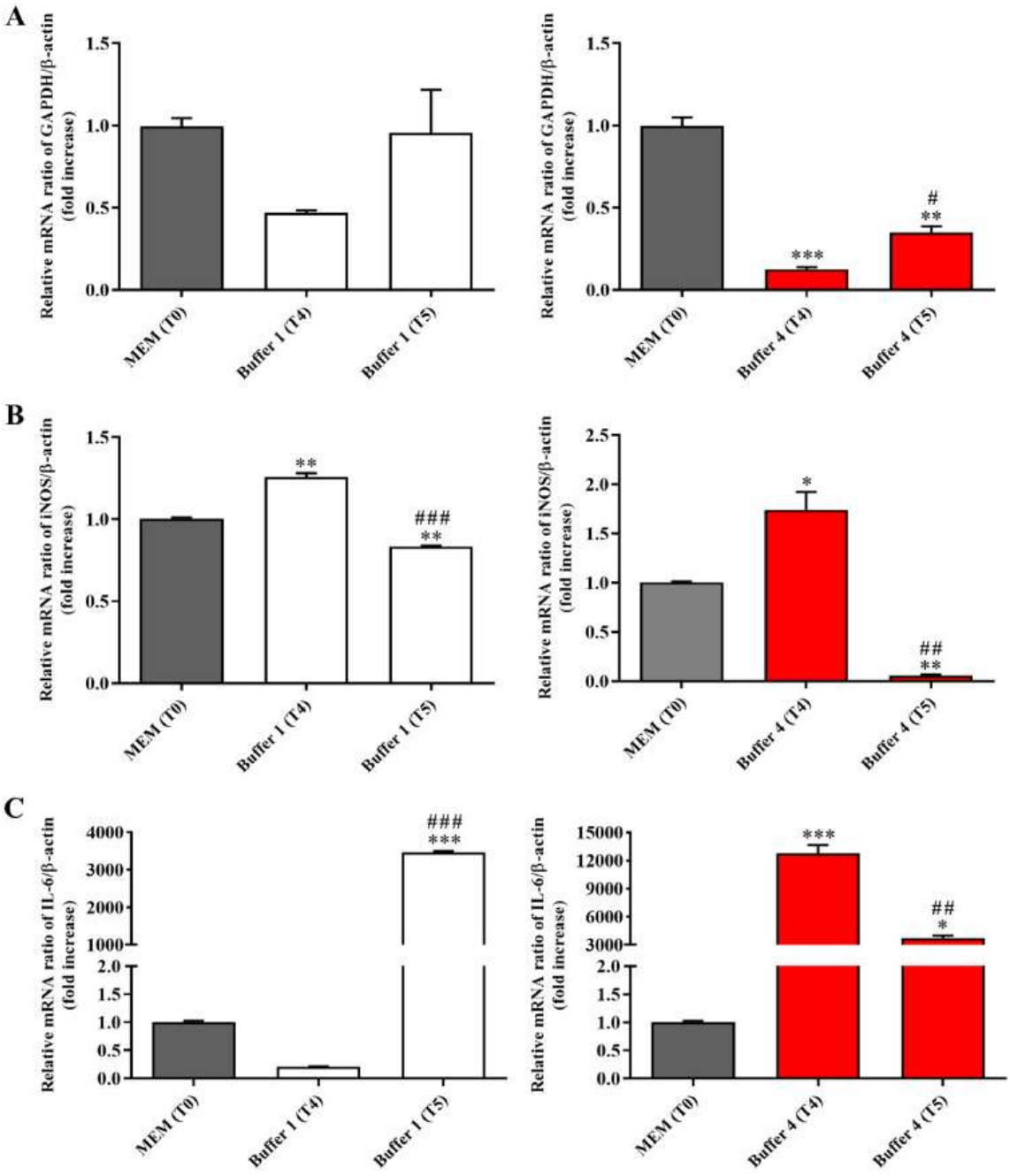

Figure 20A. Relative mRNA expression levels of GAPDH (A), iNOS (B) and IL-6B (C) were measured by RT-qPCR in CaCo-2 cells after exposure to Buffer 1 and Buffer 4. Data were normalized to β-actin and expressed as fold changes relative to untreated control cells (resuspend in MEM at T0. Data are represented as mean ± standard deviation (SD) of at least three independent experiments. Statistical significance versus T0: *$p < 0.005$, ** $p < 0.01$, *** $p < 0.001$; versus T4: # $p < 0.05$, ## $p < 0.01$, ### $p < 0.001$.

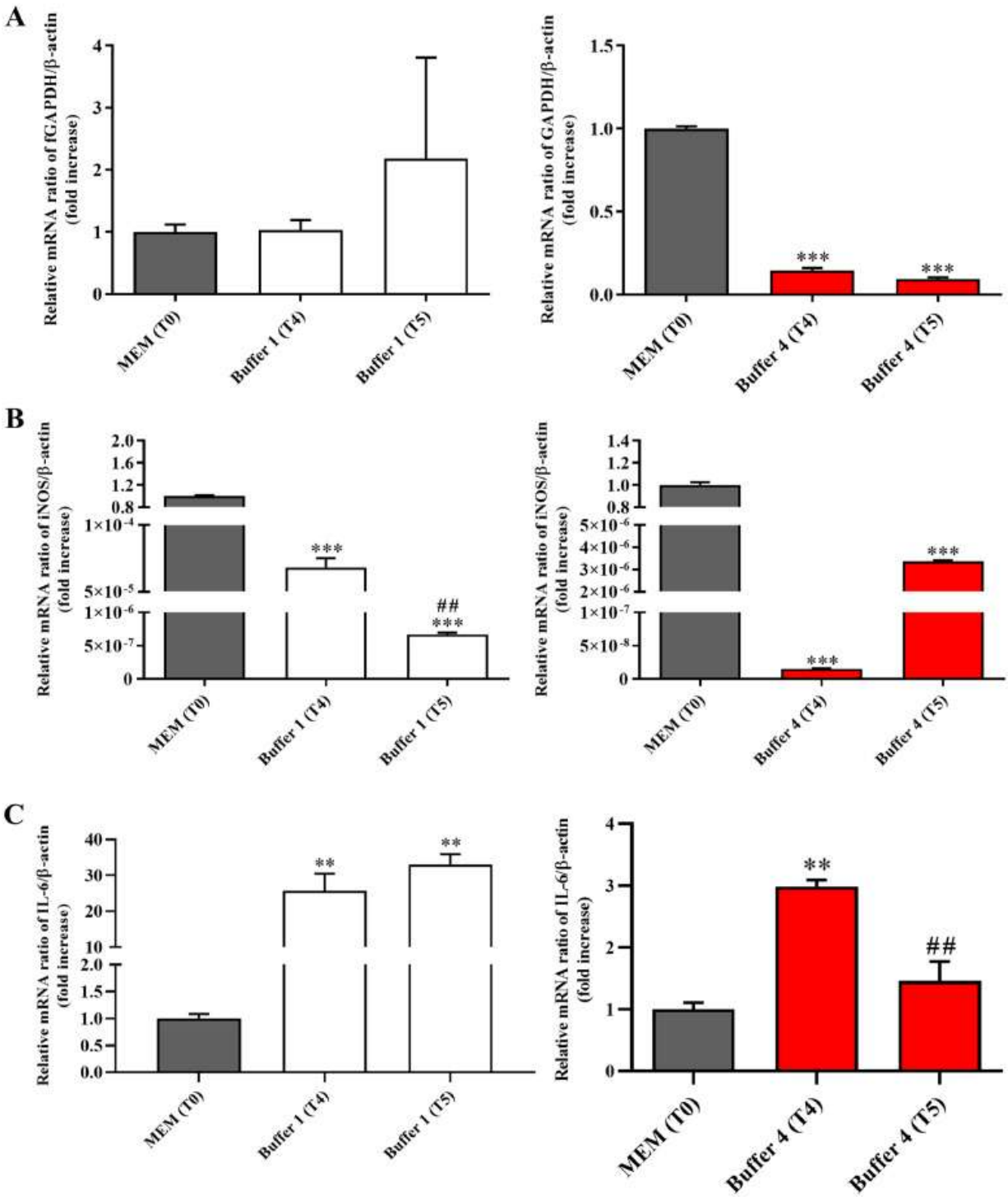

Figure 20B. Relative mRNA expression levels of GAPDH (A), iNOS (B) and IL-6B (C) were measured by RT-qPCR in CaCo-2 cells after exposure to Buffer 1 and Buffer 4. Data were normalized to β-actin and expressed as fold changes relative to untreated control cells (resuspend in MEM at T0. Data are represented as mean ± standard deviation (SD) of at least three independent experiments. Statistical significance versus T0: *$p < 0.005$, ** $p < 0.01$, *** $p < 0.001$; versus T4: # $p < 0.05$, ## $p < 0.01$, ### $p < 0.001$.

3.1.4. Impact of Conductivity on Cell Viability

The metabolic impact of varying the conductivity of Buffer 4/DEP on CaCo-2 cells was assessed using the MTT assay. Cells were seeded in 96-well plates, and 24 hours after seeding the culture medium was replaced with four Buffer 4/DEP solutions of decreasing conductivity: 33 mS/m (reference), 10 mS/m, 1 mS/m, and 0.1 mS/m. Cell viability was then evaluated after 2 hours and 24 hours of exposure. At 2 hours (Figure 21, left), CaCo-2 cells maintained metabolic activity close to the control, with values of 96.76% at 33 mS/m, 102.5% at 10 mS/m, 103.19% at 1 mS/m, and 97.41% at 0.1 mS/m. At 24 hours (Figure 21, right), cell behavior diverged depending on conductivity. The reference condition (33 mS/m) and 10 mS/m supported growth slightly above control levels (107.41% and 106.3%, respectively). By contrast, lower conductivities resulted in reduced viability, with 89.10% at 1 mS/m and 79.04% at 0.1 mS/m.

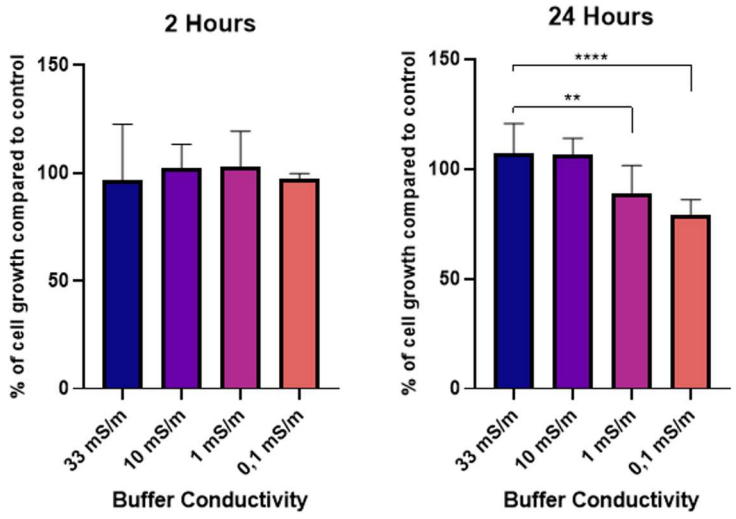

Figure 21. Effect of Buffer 4/DEP conductivity on CaCo-2 cell metabolic activity assessed by MTT assay. CaCo-2 cells were exposed for 2 h (left) and 24 h (right) to Buffer 4/DEP solutions with decreasing conductivity values (33 mS/m, 10 mS/m, 1 mS/m, 0.1 mS/m). Cell viability is expressed as percentage relative to untreated controls.

3.2. ELECTROROTATION SPECTRA

All cell lines involved in the study were pre-treated as described in the "Materials and Methods" section and diluted in buffer DEP to a final concentration of 500 cells/µL. The working volume of the electrorotation chip is approximately 15 µL, corresponding to 7,500 cells. Once injected into the chip, the cells are exposed to frequencies ranging from 10 kHz to 1000 kHz. The computer, connected to the microscope via the CAM, records the electrorotation at each frequency for 5 seconds. An algorithm developed at University of Catania DIEII is then used to calculate the rotational velocity at each frequency, as shown in the following figures.

Breast-derived cell lines (Figure 22), The electrorotation analysis performed on the 184A1, MDA-MB-231, and MCF-7 cell lines revealed distinct rotational behaviors in response to increasing frequencies ranging from 10 kHz to 1100 kHz. As shown in the table and corresponding plot, the 184A1 (non-tumorigenic epithelial breast cells) exhibited a markedly faster rotation profile, especially at low frequencies (e.g., −19.6 rad/s at 70 kHz), suggesting an higher membrane polarizability compared to the cancerous counterparts. MCF-7 (luminal A breast cancer cells) displayed intermediate values across the spectrum, while MDA-MB-231 (triple-negative breast cancer cells) showed the lowest rotation rates, particularly in the mid-frequency range (e.g., −5.5 rad/s at 300 kHz and −0.8 rad/s at 1000 kHz).

	Tissue: **BREAST**		
	Cell Line		
KHz	**184A1**	**MDAMB-231**	**MCF7**
30	-9,3	-7,0	-5,9
40	-14,3	-7,3	-6,4
50	-17,1	-7,1	-7,6
60	-17,4	-6,8	-7,7
70	-19,6	-6,4	-8,2
80	-19,2	-6,0	-8,7
90	-19,1	-5,5	-9,4
100	-17,9	-5,5	-11,0
200	-13,2	-3,6	-8,9
300	-10,0	-2,6	-7,5
400	-7,7	-2,2	-6,8
500	-7,0	-2,0	-5,1
600	-5,9	-1,8	-4,0
700	-5,2	-1,7	-2,8
800	-4,5	-1,6	-1,6
900	-3,7	-1,5	-0,4
1000	-3,2	-1,4	0,8
	FASTER		
	SLOWER		

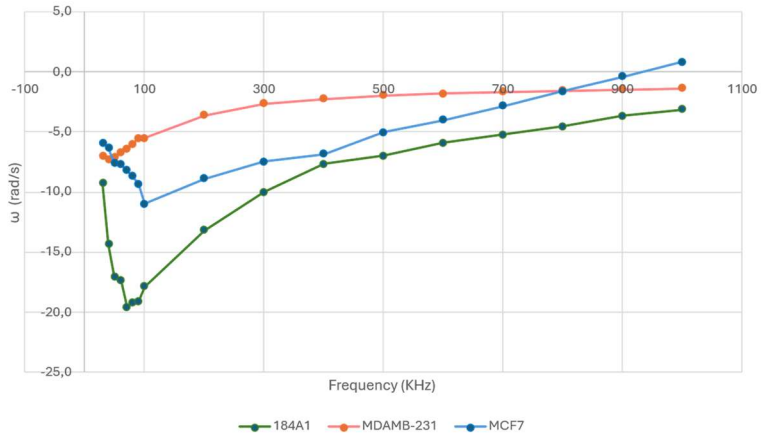

Figure 22. On the left, the table shows the electrorotation values of the 184A1 (green in the graph), MDA-MB-231 (orange in the graph), and MCF-7 (blue in the graph) cell lines across all frequencies within the tested spectrum. Each data point represents the average of at least four independent measurements. On the right, the graph derived from the table.

Prostate-derived cell lines (Figure 23), across all frequencies, the non-tumorigenic PWR1E cells exhibited the fastest rotational velocities, with values consistently more negative than those of the two tumor-derived lines. A minimal shift in ω was observed until approximately 100 kHz, followed by a gradual decrase in velocity at higher frequencies. The two cancerous cell lines, PC3 and LnCap, displayed similar trends but with slower velocities across the entire spectrum. PC3 cells showed the lowest rotational behavior, particularly at intermediate and high frequencies, reaching −0.6 µrad/s at 800 kHz. LnCap cells followed a comparable but slightly faster trajectory, with values remaining above those of PC3 but under PWR1E. Notably, the difference between PC3 and LnCap became more pronounced in the mid-to-high frequency range (300–700 kHz). These data indicate a clear separation in rotational response between non-malignant and malignant prostate cell lines, with a progressive divergence as frequency increases.

	Tissue:	PROSTATE	
	Cell Line		
KHz	PWR1E	PC3	LnCap
30	-8,8	-6,6	-6,3
40	-8,8	-6,9	-7,6
50	-8,9	-6,5	-6,8
60	-8,6	-5,7	-7,0
70	-8,2	-5,4	-6,6
80	-7,9	-5,0	-6,3
90	-7,7	-5,0	-6,0
100	-6,8	-5,1	-5,4
200	-6,0	-3,1	-4,6
300	-3,8	-1,8	-3,1
400	-3,5	-2,5	-3,0
500	-3,1	-2,0	-2,5
600	-3,3	-1,6	-2,5
700	-2,9	-1,1	-1,5
800	-2,4	-0,6	-1,3

FASTER

SLOWER

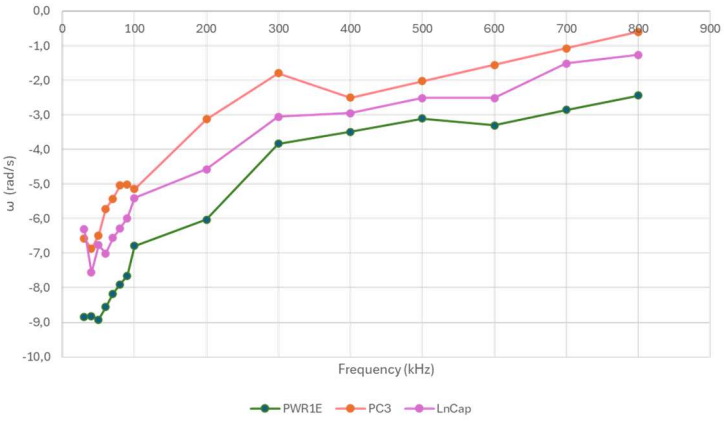

Figure 23. On the left, the table shows the electrorotation values of the PWR1E (green in the graph), PC3 (orange in the graph), and LnCap (pink in the graph) cell lines across all frequencies within the tested spectrum. Each data point represents the average of at least four independent measurements. On the right, the graph derived from the table.

Colon-derived cell lines[98] (Figure 24), the non-cancerous CCD-841 cells exhibited the fastest rotational velocities across the entire spectrum, with a pronounced minimum between 50 and 100 kHz (e.g., −24.1 rad/s at 70 kHz), indicating a maximum response to the applied field. Their rotation gradually decreased at higher frequencies but remained consistently higher that of the cancerous lines. Both tumor-derived cell lines, HCT-116 and CaCo-2, showed slower rotational velocities at all frequencies tested. HCT-116 displayed a relatively stable curve with values decreasing progressively with frequency, reaching −2.4 rad/s at 1000 kHz. CaCo-2 cells followed a similar trend but with slightly slower velocities in the higher frequency range, culminating in the least positive value (−0.4 rad/s) at 1000 kHz among the three cell lines.

The gap between CCD-841 and the two cancer cell lines was more evident at lower and intermediate frequencies, while differences between HCT-116 and CaCo-2 became more distinguishable at higher frequencies.

	Tissue:	COLON	
	Cell Line		
KHz	CCD-841	HCT-116	CaCo-2
30	-10,1	-8,4	-13,3
40	-16,8	-11,7	-14,3
50	-20,5	-11,4	-13,3
60	-20,8	-10,7	-12,4
70	-24,1	-10,1	-11,6
80	-23,6	-9,4	-10,5
90	-23,5	-8,8	-9,9
100	-21,9	-8,4	-9,2
200	-16,0	-5,3	-5,9
300	-12,0	-4,1	-4,9
400	-8,9	-3,5	-4,6
500	-8,2	-3,1	-3,8
600	-6,8	-2,8	-3,1
700	-5,9	-2,7	-2,4
800	-4,9	-2,5	-1,8
900	-3,8	-2,3	-1,1
1000	-3,1	-2,4	-0,4
	FASTER		
	SLOWER		

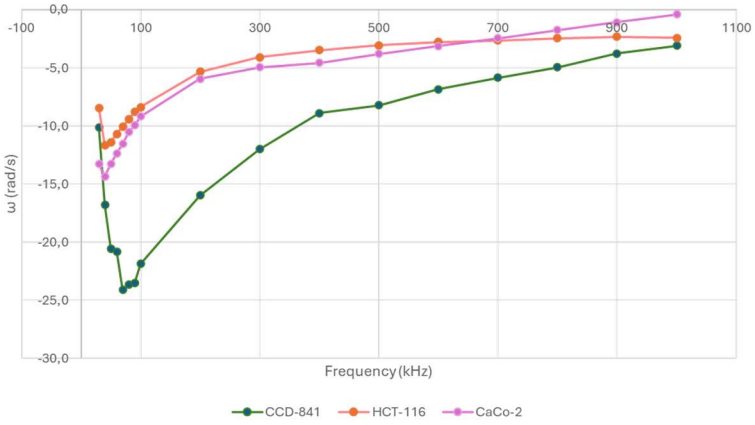

Figure 24. On the left, the table shows the electrorotation values of the CCD-841 (green in the graph), HCT-116 (orange in the graph), and CaCo-2 (pink in the graph) cell lines across all frequencies within the tested spectrum. Each data point represents the average of at least four independent measurements. On the right, the graph derived from the table.

Blood-derived cell lines (Figure 25), HCC1937 cells displayed the most stable behavior, with modestly negative rotational velocities across all frequencies, and only a limited shift in response to increasing frequency. In contrast, HDLM2 cells exhibited a marked frequency-dependent profile: an initial increase in rotational velocity was observed between 50 and 300 kHz, reaching a minimum at 300 kHz (−7.0 rad/s), followed by a progressive recovery at higher frequencies. U266 cells also showed a biphasic profile. Their rotational velocity increased sharply at low frequencies (−6.5 rad/s at 200 kHz), but unlike HDLM2, the deceleration phase began earlier and proceeded more steeply, resulting in lower velocities in the high-frequency range, culminating in −2.5 rad/s at 1000 kHz. Compared to the solid tumor-derived cell lines analyzed in this study, the differences among hematological cell lines were less pronounced. The potential reasons behind this more homogeneous electrorotational behavior will be addressed in the Discussion section.

Tissue:	BLOOD		
	Cell Line		
KHz	HCC1937	HDLM2	U266
30	-1,7	-2,0	-4,0
40	-1,7	-2,3	-4,1
50	-1,8	-2,9	-4,8
60	-1,8	-3,4	-4,5
70	-1,9	-3,6	-4,4
80	-2,0	-3,8	-6,0
90	-2,3	-4,4	-4,6
100	-2,6	-4,8	-6,3
200	-3,6	-6,4	-6,5
300	-3,8	-7,0	-4,9
400	-3,6	-6,7	-4,4
500	-3,5	-6,3	-3,4
600	-3,2	-5,7	-4,1
700	-3,1	-5,4	-3,6
800	-3,0	-5,2	-3,5
900	-3,0	-5,2	-3,5
1000	-3,1	-4,7	-2,5
	FASTER		
	SLOWER		

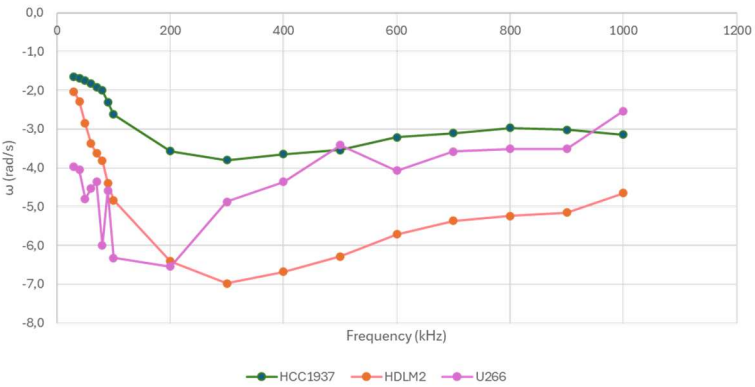

Figure 25. On the left, the table shows the electrorotation values of the HCC-1937 (green in the graph), HDLM2 (orange in the graph), and U266 (pink in the graph) cell lines across all frequencies within the tested spectrum. Each data point represents the average of at least four independent measurements. On the right, the graph derived from the table.

3.3 RT-qPCR for ELECTROROTATION-RELATED GENES

To explore potential molecular determinants underlying the observed differences in electrorotation spectra, the expression of two genes—*BANP* (BTG3 Associated Nuclear Protein), a chromatin-associated regulator of cell cycle and apoptosis[99], and *PTK2* (Protein Tyrosine Kinase 2, also known as FAK1), a cytoskeletal-associated kinase involved in adhesion and mechanotransduction[100]—was measured by RT-qPCR across all cell lines. Gene expression values were then compared to the corresponding electrorotation profiles, with particular attention to the frequency at which the rotational velocity reaches its minimum, commonly referred to as the electrorotation peak. This peak corresponds to a crossover point in the dielectric response of the cell[101], where the dominant response to electrorotation shifts from the membrane to the cytoplasmic compartment. It is influenced by multiple cellular features, including membrane capacitance, cytoplasmic conductivity, and internal structural organization[77]. The analysis aimed to assess whether the expression levels of *BANP* and *PTK2* correlate with the position of the electrorotation peak, potentially reflecting molecular or structural properties that modulate the cell's dielectric behavior.

Among **breast-derived cell lines** (184A1, MCF-7, MDA-MB-231, Figure 26), the non-tumorigenic 184A1 cells demonstrated the largest dynamic range in rotational velocity (Figure 26E). This was matched by the highest *BANP* expression (Figure 26A). In contrast, MCF-7 and MDA-MB-231 displayed more restricted changes in rotation (Figure 26E) and lower *BANP* levels (Figure 26A). *PTK2* expression was again found to be comparable across the three lines (Figure 26C), with a clear correlation to electrorotation behavior (R^2=0.8361. Figure 26D). It was observed also a higher correlation between *BANP* expression and the Peak of Rotational Velocity (Figure 26B), with a R^2=0.9625 (Figure 26B).

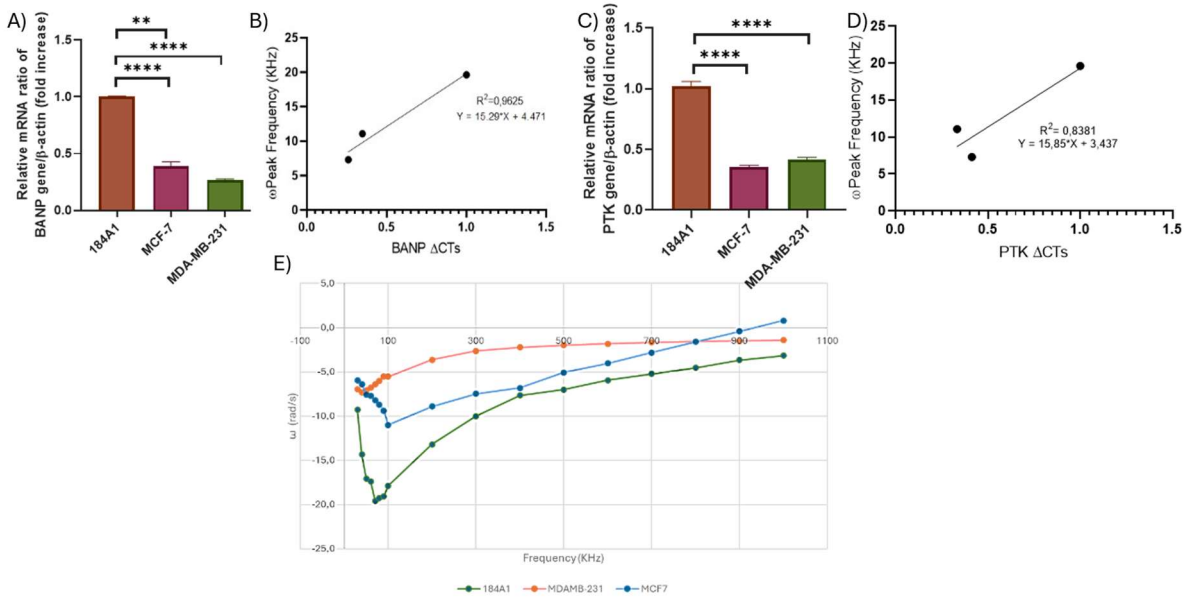

Figure 26. Relative mRNA expression levels of *BANP* (A) and *PTK2* (C) were measured by RT-qPCR in Breast derived cell line in normal conditions. Data were normalized to β-actin and expressed as fold changes relative to untreated control cells. (B) Correlation between *BANP* expression and ω maximum frequency. (D) Correlation between *PTK2* expression and ω maximum frequency. (E) Relative electrorotation spectrum. Data are represented as mean ± standard deviation (SD) of at least three independent experiments. Statistical significance: *p < 0.05, ** p < 0.01, *** p < 0.001, **** p < 0.0001.

In **Prostate-derived cell lines** (PWR1E, PC3, LnCap, Figure 27), analysis of *BANP* (Figure 27A) and *PTK2* (Figure 27C) gene expression was compared with their respective electrorotation profiles. Among the three, PWR1E sane cells exhibited the largest shift in rotational velocity across the frequency range (Figure 27E), which coincided with the highest *BANP* expression (R^2=0.9563, Figure 27B). Conversely, PC3 and LnCap showed more moderate variations in electrorotation, paralleled by lower *BANP* levels (Figure 27A). *PTK2* expression was relatively similar among all three cell lines, and no direct correlation with rotational velocity changes was observed (Figure 27D).

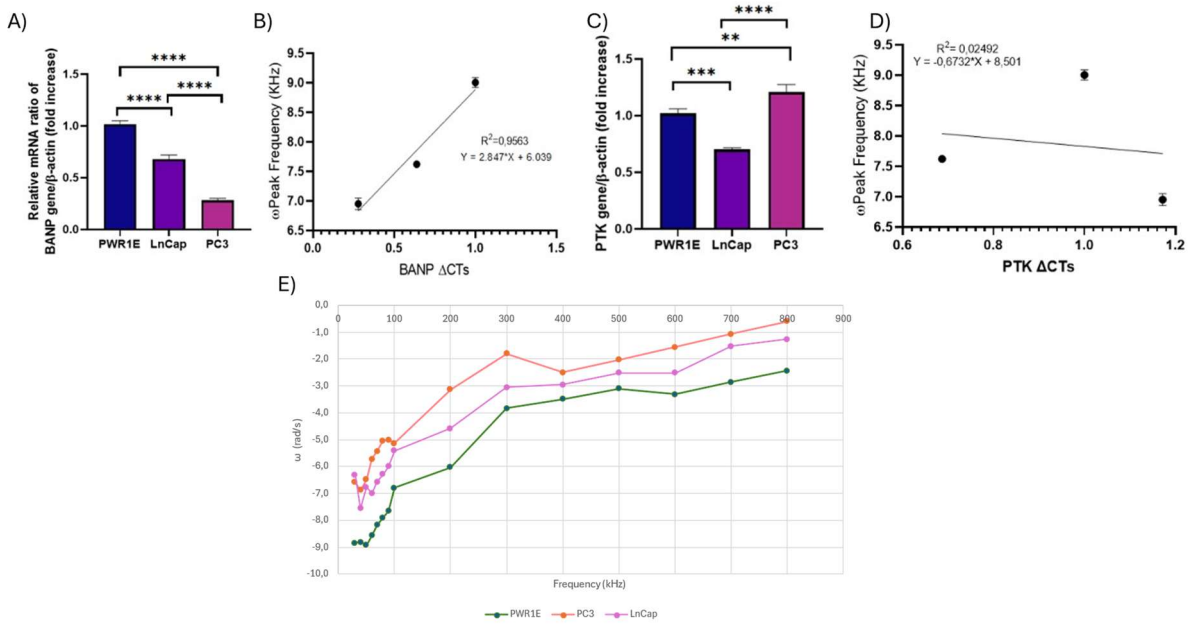

Figure 27. Relative mRNA expression levels of *BANP* (A) and *PTK2* (C) were measured by RT-qPCR in Prostate derived cell line in normal conditions. Data were normalized to β-actin and expressed as fold changes relative to untreated control cells. (B) Correlation between *BANP* expression and ω maximum frequency. (D) Correlation between *PTK2* expression and ω maximum frequency. (E) Relative electrorotation spectrum. Data are represented as mean ± standard deviation (SD) of at least three independent experiments. Statistical significance: *p < 0.05, ** p < 0.01, *** p < 0.001, **** p < 0.0001.

For the **colon-derived cell lines** (CCD-841, HCT-116, CaCo-2, Figure 28), CCD-841 cells showed the greatest difference in rotational velocity across the spectrum (Figure 28E), and this corresponded to a higher expression of *BANP* (Figure 28A) compared to the two tumor-derived lines. HCT-116 and CaCo-2, both of which displayed more stable rotational profiles, showed reduced *BANP* expression (Figure 28A). *PTK2* levels varied slightly among the CaCo-2 and CCD-841lines and increase significantly in HCT-116 (Figure 28C). *BANP* shows a direct proportionality with ω Peak Frequency ($R^2 = 0.9627$, Figure 28C), while *PTK2* seems to be exactly inverted, but not so correlated ($R^2 = 0.4458$, Figure 28D).

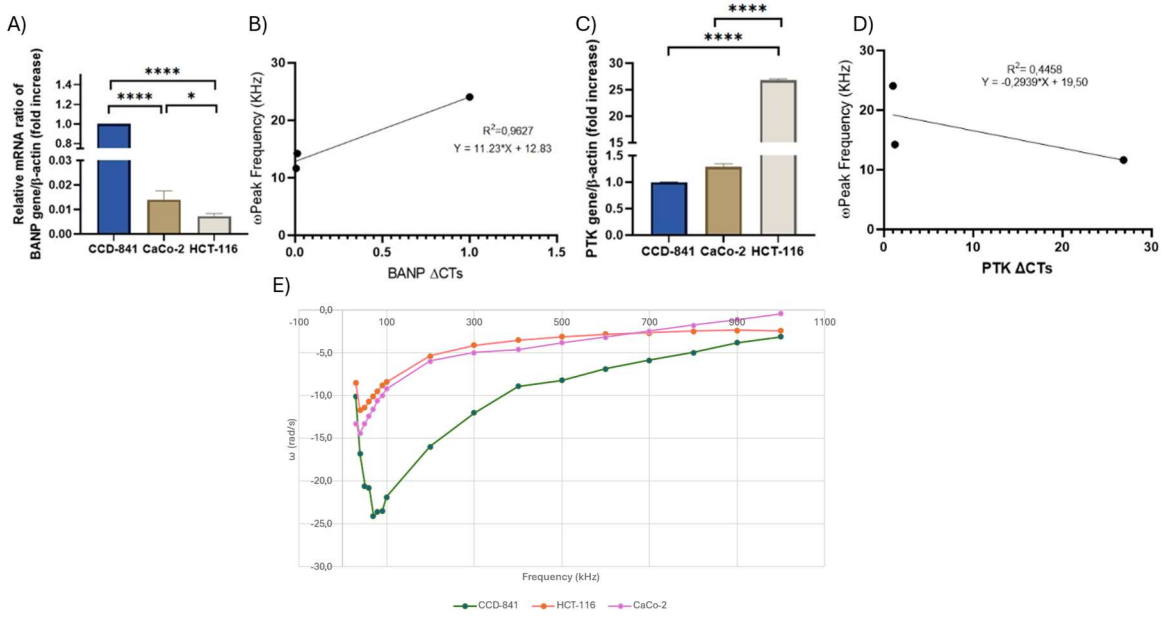

Figure 28. Relative mRNA expression levels of *BANP* (A) and *PTK2* (C) were measured by RT-qPCR in Colon derived cell line in normal conditions. Data were normalized to β-actin and expressed as fold changes relative to untreated control cells. (B) Correlation between *BANP* expression and ω maximum frequency. (D) Correlation between *PTK2* expression and ω maximum frequency. (E) Relative electrorotation spectrum. Data are represented as mean ± standard deviation (SD) of at least three independent experiments. Statistical significance: *p < 0.05, ** p < 0.01, *** p < 0.001, **** p < 0.0001.

In the **hematopoietic cell lines** (HCC1937, HDLM2, U266; Figure 29), *BANP* expression was particularly high in HDLM2, while U266 showed values more similar to HCC1937 (Figure 29A). In contrast, the trend was reversed for *PTK2*, with U266 displaying the highest expression levels and HDLM2 the lowest, only slightly below those of HCC1937 (Figure 29 C). No significant correlation was found between the expression of these two genes and the position of the electrorotation peak (Figure 29B and 28D).

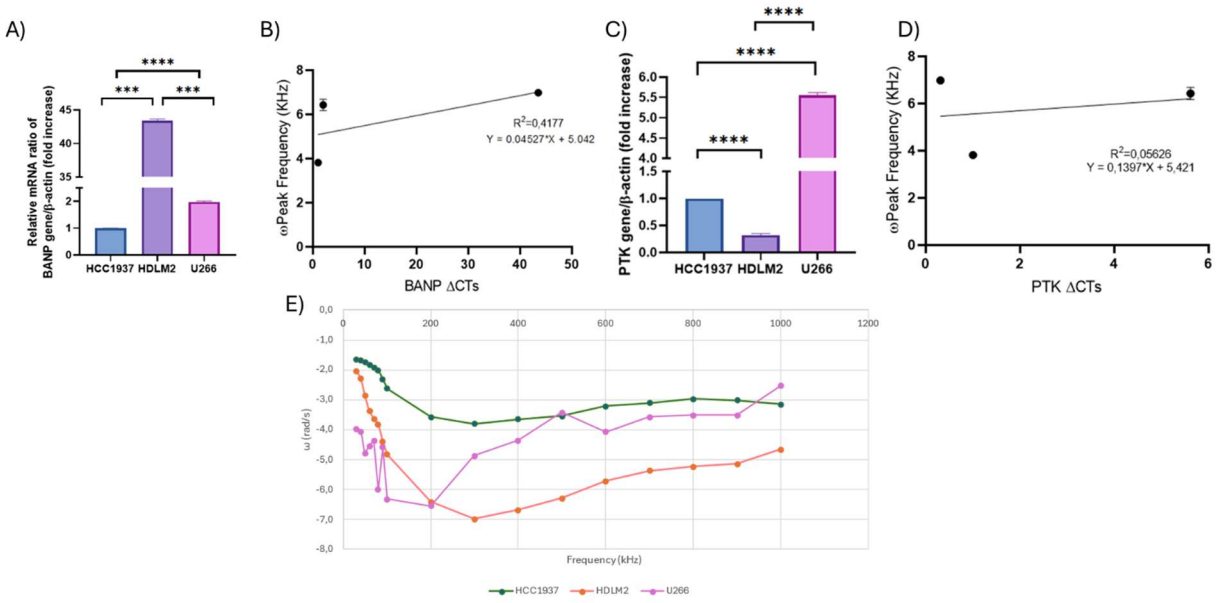

Figure 29. Relative mRNA expression levels of *BANP* (A) and *PTK2* (C) were measured by RT-qPCR in Colon derived cell line in normal conditions. Data were normalized to β-actin and expressed as fold changes relative to untreated control cells. (B) Correlation between *BANP* expression and ω maximum frequency. (D) Correlation between *PTK2* expression and ω maximum frequency. (E) Relative electrorotation spectrum. Data are represented as mean ± standard deviation (SD) of at least three independent experiments. Statistical significance: *p < 0.05, ** p < 0.01, *** p < 0.001, **** p < 0.0001.

4. DISCUSSION

4.1. SUITABILITY OF THE BUFFER SYSTEM FOR ROT EXPERIMENTS

The metabolic and physical integrity of cells during electrorotation measurements is a fundamental prerequisite, as alterations in viability, morphology, or gene expression could profoundly confound dielectric readouts. Furthermore, the development of dielectrophoretic devices for the isolation (early or not) of tumor cells is parallel to their recovery for downstream analysis, therefore a buffer that more or less significantly alters pheno/genotypic properties is not desirable. Although cell viability in this work was evaluated through the MTT assay, future studies could integrate complementary approaches (LDH release or Annexin V/PI assays) to better characterize the metabolic and structural responses of cells to different buffer conditions. Our data robustly demonstrates that Buffers 1 and 4/DEP maintain cell viability and morphology at levels comparable to standard culture conditions, confirming their appropriateness for electrorotation assays. Metabolic impact measured with the MTT assay (Figure 16) demonstrated that CaCo-2 cells exposed to Buffer 4 exhibited an initial decrease in metabolic activity (64.9% compared to the control), most likely due to the initial exposure to a buffer different from the chosen one and to transient changes in the first hour. However, after 24 hours, metabolic activity exceeded 115% compared to the control, confirming the transient nature of the changes in the first hour. Buffer 1, on the other side, has a more stable trend. In the first hour, the

CaCo-2s slightly decrease their metabolic activity (91.9%), while after 24 hours it settles just above 100%, meaning that Buffer 1 also receives greater attention when choosing the buffer of choice for ROT experiments. A possible explanation for the difference in biological impact between the two buffers can be traced back to their composition (Table 4): Buffer 4 contains many more elements that could disrupt, albeit temporarily, the cells' metabolic activity.

K562 cells exposed to both buffers showed significantly greater declines than their adhering counterparts. In fact, after one hour, mitochondrial activity dropped to 65.7%, while after 24 hours it further decreased to 81% for Buffer 1, and from 66.3% to 72.3% for Buffer 4/DEP. This finding can have an explanation: technically, MTT works better with adherent cells: suspension cells can lose some of the reagent or formazan crystals during handling, producing a lower signal even if not all cells are dead[102]. Additionally, if the buffer lacks nutrients, the metabolism of suspension cells quickly declines. In any case, the highest averages in terms of mitochondrial activity were observed with Buffer 1 (81%) and Buffer 4/DEP (80%), compared to approximately 70% for Buffers 2 and 3 (Figure 16). For this reason, the subsequent experiments regarding the 'physical' impact of the buffers were carried out using Buffers 1 and 4. Before evaluating the impact of Buffers 1 and 4/DEP on the size of CaCo-2 and K562 cells, we first aimed to determine whether the available instrument (FlowSight Imaging Flow Cytometer) could detect even minimal differences in this regard, given that Buffers 1 and 4 have partially similar electrochemical properties. Consequently, CaCo-2 cells were exposed for one hour in an incubator to solutions with increasing NaCl concentrations (from pure water up to 4%), after which they were

passed through the instrument's capillary and 5,000 events per concentration were recorded.

During data analysis, the instrument automatically defines a cut-off for each dimensional parameter analyzed (in our case, the parameter considers two aspects: "Area vs Diameter"), dividing the 5,000 events (or cells) into populations below the cut-off (Area vs Diameter -) and above the cut-off (Area vs Diameter +).

What was observed is fully consistent with the literature and follows a coherent trend[103,104] (Figure 17): in pure water, 80% of the population is above the cut-off, as cell dimensions are considerably larger due to the hypotonic effect of the pure solvent, which causes the cells to swell. At 4% NaCl, more than 80% of the population falls below the cut-off (Area vs Diameter -), because the cells shrink in response to the high external salt concentration, reducing their size.

As shown in Figure 17B, doubling the NaCl concentration appears to produce a difference of about 5 percentage points in the populations between one concentration and the next, which supports the conclusion that the instrument is suitable for conducting the same experiments using Buffers 1 and 4/DEP to evaluate their impact on the geometric and physical parameters of CaCo-2 and K562 cells.

In the next step, CaCo-2 and K562 cells were exposed to Buffers 1 and 4/DEP for 15 (T1) to 60 (T4) minutes, using MEM as a control. In the same instrument, changes in Circularity, Side Scattering (SSC), and again Area vs. Diameter were observed. The results reported in Table 7 and Figures 18 and 19 show that:

For both cell lines, circularity remains very similar to that of the control, while SSC slightly increases for CaCo-2 but remains unchanged for K562. This latter observation reflects intrinsic differences between the lines:

solid tumor cells are more sensitive to ionic variations at the intracellular level due to a more developed cytoskeleton and a complex intracellular compartmentalization, whereas K562 cells show a less pronounced response, having fewer internal structures that could contribute to noticeable changes in granularity.

Paradoxically (Figure 19), when averaging the differences observed across the various populations, both buffers disturb these parameters less than MEM, which is why both were selected for the final evaluation conducted using RT-qPCR.

All these findings align with prior studies emphasizing the critical influence of buffer osmolarity and ionic composition on cell health during dielectrophoretic manipulation[79,105]. Buffers designed for electrorotation must balance electrical conductivity with osmotic pressure, avoiding hypotonic or hypertonic stresses that alter membrane integrity or intracellular ion gradients[106]. The stability in morphological parameters (circularity, SSC, Area vs. Diameter) shown in Figures 18 and 19 further validates that Buffers 1 and 4/DEP do not induce significant mechanical or osmotic perturbations.

After exposing both cell lines to the buffers for 120 minutes (T4) and 240 minutes (T5), RT-qPCR analysis (Figure 20A) showed that:

In CaCo-2 cells, Buffer 1 maintains GAPDH expression unchanged, which is consistent with the results obtained from the MTT assay. iNOS expression also remains stable with Buffer 1. However, after two hours, there is a notable increase in IL-6B beta. This spike can likely be explained by the composition of Buffer 1, which contains PBS, FBS, and BSA but lacks sugars or additional stabilizing ions. Such conditions may induce mild osmotic or metabolic stress, triggering inflammatory signaling pathways (e.g., NF-κB) that upregulate IL-6B.

Buffer 4 slightly reduces GAPDH expression after one and two hours, consistent with the MTT data showing a transient reduction in mitochondrial activity. iNOS expression, in contrast, decreases significantly after two hours, while IL-6B beta remains elevated, similar to Buffer 1. The observed combination of low iNOS and high IL-6B beta in Buffer 4 can be explained by the fact that these two inflammatory markers are regulated through partially independent signaling pathways. While IL-6B responds rapidly to mild osmotic or metabolic stress[107], iNOS expression is more sensitive to nutrient availability and may be downregulated under conditions that reduce oxidative stress[108], such as the presence of sugars and calcium in Buffer 4. The more stable IL-6B response may also reflect a maintained alert signal by the cells, even when oxidative stress is reduced.

For the K562 cell line, GAPDH expression is more altered compared to the adherent counterpart (Figure 20B), as can also be seen from the decrease at 120 and 240 minutes with Buffer 4. In this case as well, the data reflect the results obtained from the MTT assay in the RT-qPCR. It is interesting to note how iNOS expression in this cell line is significantly reduced by both buffers, indicating that the K562 line does not suffer from nutrient deprivation. Meanwhile, interleukin-6 beta is upregulated after both one and two hours with Buffer 1, whereas with Buffer 4, after two hours, it begins to return toward basal levels. Unlike the adherent CaCo-2 cells, which are more sensitive to environmental changes, K562 cells grow in suspension and are more resistant to stress or temporary nutrient deprivation. This characteristic likely explains why the expression of markers such iNOS is less affected in K562 cells. Moreover, since Buffer 1 contains fewer nutrients than Buffer 4, it is consistent that stress-related inflammatory processes, such as IL-6 beta expression, remain elevated for

longer when cells are exposed to Buffer 1, while Buffer 4 allows a faster return to basal levels.

In conclusion, gene expression analyses (Figures 20A/B) revealed subtle, cell-type specific modulations in stress and inflammatory markers (iNOS, IL-6B). These transient responses suggest a mild cellular reaction to buffer exposure, consistent with literature documenting that even non-cytotoxic buffers can trigger early stress signaling[109]. Importantly, these molecular changes did not translate into lasting viability or morphological deficits, supporting the buffers' practical utility. However, this underlines the necessity of assessing molecular endpoints alongside classical viability, particularly for applications where downstream gene expression fidelity is critical.

Considering that Buffer 4 induces only transient metabolic effects, preserves dimensional and morphological parameters in both adherent and suspension cells, and maintains stress- and inflammation-related gene expression within manageable ranges, it was chosen as the optimal medium for electrorotation experiments, ensuring minimal perturbation while allowing reliable downstream analyses[86].

Trying to demonstrate that also the conductivity is a fundamental parameter to consider in the creation of a new bio-compatible buffer, the results about conductivity impact on cells indicate that CaCo-2 cells tolerate Buffer 4/DEP well across a broad conductivity range in the short term (2 h), with values remaining close to or slightly above 100% of control. This suggests that acute exposure does not compromise cellular metabolism and may even transiently promote activity at intermediate conductivities.

However, after 24 hours, a clearer dependence on conductivity emerges. Conductivities close to the physiological reference (33 mS/m) or moderately reduced (10 mS/m) preserved or slightly enhanced cell growth, while markedly lower values (1 mS/m and 0.1 mS/m) resulted in a significant decrease in metabolic activity. This highlights the importance of maintaining conductivity within a biologically compatible window to ensure long-term cell stability.

The role of conductivity is particularly relevant in the context of buffer design for electrorotation experiments. Conductivity not only determines the electric field distribution and the dielectric contrast between cells and medium, but also directly affects cellular physiology, as extreme ionic depletion can disrupt osmotic balance, ion transport, and membrane potential. A well-balanced buffer must therefore satisfy two criteria simultaneously: optimal dielectric properties for accurate and sensitive electrorotation analysis and biocompatibility over the experimental timeframe, preserving metabolic activity and cellular integrity.
Overall, presented data provides a rigorous experimental basis to recommend Buffer 4/DEP for electrorotation studies, balancing electrical properties optimal for measurement with preservation of cell physiological integrity.

4.2. ELECTROROTATION SPECTRA REVEAL CELL TYPE- AND TISSUE-SPECIFIC DIELECTRIC BEHAVIOR

Electrorotation offers a unique lens into cellular biophysics, integrating membrane properties and intracellular organization. This study confirms its sensitivity to tissue origin and tumor status, in agreement with established work[51,77,89].

The distinct rotational profiles observed in breast cells (Figure 22) mirror known biophysical differences between normal and malignant phenotypes. The pronounced negative velocities and broad frequency response of 184A1 cells suggest greater membrane capacitance and heterogeneous intracellular structures, consistent with more intact and polarized epithelial membranes[77]. Conversely, the cancer lines, particularly MDA-MB-231, with their limited spectra, likely reflect decreased membrane integrity and altered cytoskeletal organization, a feature characteristic of aggressive, mesenchymal-like phenotypes[110]. This aligns with literature showing cancer progression often correlates with reduced membrane capacitance and increased cytoplasmic conductivity[111].

Prostate cells (Figure 23) exhibited a similar gradient, with PWR1E cells showing faster rotation, while tumor lines PC3 and LnCap showed slower rotation especially at mid-to-high frequencies. This supports the hypothesis that tumoral transformation alters membrane and cytoskeletal properties affecting dielectric response, consistent with prior findings linking prostate cancer aggressiveness to membrane remodeling and

intracellular ionic fluxes[112]. The frequency range (300–700 kHz) where differences peak may correspond to changes in membrane capacitance and cytoplasmic permittivity[113].

In colon cells (Figure 24), the notable dielectric contrast between CCD-841 and cancerous CaCo-2 and HCT-116 is expected and already analyzed by this research team[98], as tumor progression even in this case reduce membrane complexity and alter cytoplasmic composition[114]. The observation that CaCo-2 rotates faster at high frequencies than HCT-116 is intriguing, potentially reflecting differential differentiation states or polarity, supported by evidence that CaCo-2 cells can form polarized monolayers mimicking enterocytes, while HCT-116 are more undifferentiated[115]. This suggests electrorotation can capture subtle phenotypic differences beyond mere tumor/non-tumor status.

The hematopoietic lines (Figure 25) stand apart with their flatter and less dynamic profiles, exhibiting minimal variation in rotational velocity. This may be due to their suspension phenotype and simpler architecture, lacking the complex membrane and cytoskeletal structures of adherent epithelial cells. Such uniform dielectric behavior has been reported previously and is consistent with less intracellular compartmentalization and lower membrane capacitance[106]. It also warns against direct comparison between suspension and adherent cells in dielectric studies, as their fundamental biophysical properties diverge.

In sum, the results emphasize that electrorotation is a sensitive, label-free method capable of distinguishing cell types and transformation states via

their unique dielectric fingerprints, confirming and extending prior work in the field.

Several studies have previously applied electrorotation to characterize specific cellular models, confirming that ROT can resolve differences in membrane properties, cytoplasmic conductivity or dielectric dispersion[116]. However, a direct comparison with our results is not fully appropriate for two main reasons. First, the experimental platforms used in earlier works differ substantially from the ROT-QSG system employed in this thesis, particularly in terms of electrode geometry, field uniformity, signal generation, and the level of automation[117]. These technological differences strongly influence the amplitude, frequency-dependence, and stability of the measured rotational spectra, making the absolute values reported in different studies only partially comparable.

Second, most previous electrorotation studies were conducted on very small cell numbers[116], often limited to single-cell analysis or a few cells per experiment, due to the low throughput and manual nature of traditional ROT setups. In contrast, the system used in this work enables the acquisition and analysis of a significantly larger number of cells, providing more robust statistics and allowing the identification of cell-type–specific dielectric signatures with higher confidence.

4.3. CORRELATION BETWEEN *BANP* AND *PTK2* EXPRESSION AND ELECTROROTATION PEAK FREQUENCY

The search for molecular pathways that correlate with dielectric behavior is challenging but crucial for electrorotation mechanistic understanding. Our finding that *BANP* expression strongly correlates with the electrorotation peak in solid tumor-derived lines (breast, prostate, colon; Figures 26–28) is novel and biologically plausible.

BANP, implicated in chromatin remodeling and cell cycle regulation[99,118]could influence nuclear architecture and intracellular ionic environment, both key determinants of cytoplasmic conductivity and membrane potential[119]. High *BANP* expression in non-tumorigenic lines correlating with deeper peaks and broader electrorotation spectra, suggests a more complex intracellular organization or tighter chromatin compaction, which may increase dielectric heterogeneity. This hypothesis aligns with emerging evidence linking nuclear structure alterations to changes in cellular dielectric properties[120].

A plausible explanation for the observed correlation between *BANP* expression and electrorotation profiles in solid-derived cell lines lies in the interplay between nuclear organization, intracellular charge distribution, and cell morphology[99,118]. Healthy cells, which generally show higher *BANP* expression, displayed broader electrorotational spectra and definite peaks. This can be interpreted as the result of a more ordered chromatin and cytoskeletal architecture[121], which provides greater coherence in the

distribution of electrical charges within the cell[122]. Consequently, the transition between membrane-dominated and cytoplasm-dominated responses becomes more distinct, yielding a more evident dielectric peak. From a molecular point of view, *BANP* may serve as a marker of internal dielectric integrity. Its role in regulating chromatin compaction suggests that high *BANP* expression could promote a more compact and electrically homogeneous nucleus, thereby amplifying the net dipole moment induced during exposure to a rotating field. This enhanced polarization capacity may explain the stronger and more defined electrorotational signatures observed in *BANP*-high cells.

Finally, cellular geometry emerges as an additional determinant of dielectric behavior. Non-transformed epithelial cells typically maintain a regular, often spherical morphology, which favors uniform polarization and efficient rotation[123]. In contrast, tumor cells frequently exhibit irregular morphologies[124], characterized by pseudopodia, nuclear distortions, vacuolization, and altered organelle organization. These structural abnormalities may disrupt the homogeneity of the electric field distribution across the cell, resulting in attenuated frequency responses and in some cases a shift or flattening of the electrorotation peak.

Taken together, these considerations support the idea that *BANP* expression, intracellular order, and cell morphology act synergistically to shape dielectric properties, explaining why healthy cells exhibit sharper and more coherent electrorotational responses compared to their malignant counterparts.

A separate discussion is required for suspension cell lines.

Despite exhibiting measurable differences in *BANP* expression levels (Figure 29A), the hematopoietic lines analyzed (HCC1937, HDLM2, and

U266) showed remarkably similar electrorotation spectra, characterized by flat, poorly defined peaks and minimal variation across frequencies (Figures 29B–D). This apparent discrepancy suggests that the lack of correlation between *BANP* expression and electrorotation behavior in these cells does not imply the absence of a biological relationship but rather reflects the specific biophysical and structural nature of hematopoietic cells.

This highlights that correlation between *BANP* expression and electrorotation behavior must be interpreted in light of the fundamental differences between adherent and suspension cells. In solid-tissue-derived cell lines (such as breast, prostate, and colon), higher *BANP* expression is associated with broader and more defined electrorotation spectra. This relationship likely reflects the interplay between chromatin organization, cytoskeletal integrity, and membrane polarization, which are all interdependent in adherent cells[125]. *BANP*, being involved in chromatin remodeling and transcriptional regulation, contributes to maintaining nuclear compaction and structural order, which may propagate to cytoskeletal organization and, consequently, to a more coherent dielectric response.

In contrast, hematopoietic lines, representing suspension phenotypes, displayed similar electrorotation spectra regardless of *BANP* expression levels. This does not necessarily indicate that *BANP* has no correlation with electrorotation, but rather that its structural consequences cannot manifest dielectrically in cells that lack polarity, stable focal adhesions, and cytoskeletal anchoring. In such models, the dielectric response is dominated by the homogeneous properties of the membrane and

cytoplasm, leading to flatter spectra and reduced sensitivity to nuclear-level variations[126].

This hypothesis is speculative but logically grounded. Since *BANP* is known to influence chromatin compaction and nuclear organization, it is plausible that such structural modulation could have downstream effects on cytoskeletal arrangement, cell adhesion dynamics, and ultimately on the dielectric response. However, this connection remains theoretical at present, as no direct experimental evidence linking *BANP* to adhesion-related or cytoskeleton-associated pathways has been reported in the current literature.

In summary, the relationship between *BANP* expression and electrorotation behavior is context-dependent: it emerges clearly in structurally complex, adherent cells where nuclear, cytoskeletal, and membrane domains are functionally coupled, but becomes undetectable in suspension systems where such coupling is intrinsically limited.

Regarding *PTK2*, its absence of correlation with electrorotation behavior was unexpected given its known role in focal adhesion, mechanotransduction, and cytoskeletal dynamics[127]. However, *PTK2* expression levels alone may insufficiently capture functional differences in membrane-cytoskeleton interactions, or these interactions may not significantly influence the dielectric parameters measured. Prior studies suggest that electrorotation is more sensitive to global dielectric properties than localized signaling events[106]. Hence, *PTK2*'s role may be masked or irrelevant in this context.

To summarize, the factors modulating electrorotation velocity and the sharpness of the rotational peak can be broadly grouped according to cellular phenotype, molecular expression, and morphology (Table 8). Healthy, well-structured cells with high *BANP* expression and regular geometry tend to rotate faster and display broader, more defined spectra, whereas tumor and hematopoietic cells, often characterized by reduced *BANP*

expression, cytoskeletal disorganization, and irregular shapes, exhibit flatter and attenuated profiles. A concise overview of these relationships is presented in Table 8.

Factors Increasing Electrorotation Velocity / Producing Sharper Peaks	Factors Decreasing Electrorotation Velocity / Flattening Spectra
Healthy phenotype (e.g., 184A1, PWR1E, CCD-841): intact membranes, organized cytoskeleton, heterogeneous cytoplasmic structure	Tumor phenotype (e.g., MDA-MB-231, PC3, CaCo-2, HCT-116): reduced membrane integrity, altered cytoskeleton, increased cytoplasmic conductivity
High *BANP* expression → compact chromatin, more ordered nucleus, stronger net dipole moment	Low *BANP* expression → less compact chromatin, reduced dielectric coherence
Regular/spherical morphology of non-transformed epithelial cells, favoring uniform polarization	Irregular morphology (pseudopodia, nuclear distortions, vacuolization, organelle alterations)
Adherent solid tissues (breast, prostate, colon) → broader spectra, sharper dielectric transitions	Suspension phenotype (hematopoietic lines: HCC1937, U266, HDLM2) → flatter spectra, limited variability
Polarized and differentiated epithelia (e.g., CaCo-2 compared to HCT-116) → broader responses, higher dielectric complexity	Advanced malignancy / mesenchymal features → restricted spectra, attenuated frequency response
PTK2 expression: no consistent correlation observed	

Table 8. Summary of factors influencing electrorotation velocity and peak frequency.

5. CONCLUSION and FUTURE PERSPECTIVES

This thesis demonstrates the potential of electrorotation as a powerful, label-free technique for investigating the dielectric properties of living cells, with relevance for both basic research and biomedical applications. Through the careful selection and validation of biocompatible buffers, specifically Buffer 1 and Buffer 4/ Buffer DEP, we established optimal experimental conditions that preserve cell viability, morphology, and molecular integrity during electrorotation measurements.

Electrorotation spectra acquired from twelve cell lines of different tissue origins revealed distinctive, tissue-specific rotational behaviors. In solid tissue-derived lines, particularly from breast, prostate, and colon, the technique successfully discriminated between non-tumorigenic and tumorigenic phenotypes, uncovering dielectric signatures likely associated with differences in membrane structure, cytoplasmic conductivity, and intracellular organization. In contrast, hematological lines exhibited flatter, more homogeneous spectrum, possibly reflecting their suspension nature and reduced internal complexity.

Importantly, the correlation analysis between dielectric response and gene expression revealed a consistent relationship between *BANP* expression and the position of the electrorotation peak in solid tissues, suggesting a link between chromatin organization and dielectric behavior. Conversely, *PTK2*, despite its biological relevance in cell adhesion and mechanotransduction, showed no meaningful correlation, underscoring the complexity of identifying molecular markers of dielectric phenotype. Although the original project design included the

extension of electrorotation experiments to bacterial systems, this part of the study could not be performed due to the unavailability of the necessary microfluidic device, caused by technical limitations beyond the author's control. Despite this, the work conducted establishes a solid foundation for future investigations into microbial dielectric profiling. Overall, these results highlight the versatility of electrorotation not only as a tool for cell characterization, but also as a potential readout of functional molecular states.

Looking forward, several perspectives emerge from this work. First, future studies should explore the application of electrorotation to discriminate between healthy and host cells infected with intracellular pathogens. This represents a crucial biomedical challenge, since early detection of infection-related biophysical alterations could open novel diagnostic avenues. Although originally planned within this thesis, these experiments could not be carried out due to time and instrument availability, but they remain in a promising direction.

Second, the ability of electrorotation to distinguish healthy and tumor cells in mixed populations should be systematically tested. The integration of these datasets with machine learning–based algorithms would allow the development of predictive models capable of recognizing subtle dielectric signatures in heterogeneous samples, ultimately paving the way for translational applications such as liquid biopsy or early tumor detection.

Finally, a key step toward practical applicability will be to assess the post-assay recovery and reculture of cells after electrorotation experiments. Demonstrating that cells remain viable and functionally competent after exposure would validate the platform as compatible with

downstream analyses (e.g., transcriptomics, proteomics, or functional assays), greatly enhancing its value as a non-destructive analytical method.

In conclusion, while this thesis provides a solid proof-of-concept of electrorotation as a sensitive biophysical profiling tool, its future lies in expanding towards more complex biological systems, integrating computational approaches, and validating downstream compatibility, finally bridging the gap between biophysical research and clinical applications.

6. RESEARCH CONTRIBUTIONS AND DISSEMINATION

6.1. RELATED TO PhD PROJECT

Translational Oncology 28 (2023) 101599

Contents lists available at ScienceDirect

Translational Oncology

journal homepage: www.elsevier.com/locate/tranon

Impact of buffer composition on biochemical, morphological and mechanical parameters: A tare before dielectrophoretic cell separation and isolation

Paolo G. Bonacci [a,1], Giuseppe Caruso [b,c,1,*], Grazia Scandura [d], Clarissa Pandino [d], Alessandra Romano [d], Giorgio I. Russo [e], Ronald Pethig [f], Massimo Camarda [g,2], Nicolò Musso [a,2]

[a] Department of Biomedical and Biotechnological Sciences, University of Catania, Catania 95123, Italy
[b] Department of Drug and Health Sciences, University of Catania, Catania 95125, Italy
[c] Oasi Research Institute-IRCCS, Troina 94018, Italy
[d] Haematological section, University of Catania, Catania 95125, Italy
[e] Urology section, University of Catania, Catania 95125, Italy
[f] Institute for Integrated Micro and Nano Systems, Joint Research Institute for Integrated Systems, School of Engineering, The University of Edinburgh, Edinburgh EH9 3JF, UK
[g] STLab srl, Catania 95126, Italy

ARTICLE INFO

Keywords:
Dielectrophoresis
Cell status
Biochemical parameters
Circulating tumor cells
Cell isolation and separation
Microfluidics

ABSTRACT

Dielectrophoresis (DEP) represents an electrokinetic approach for discriminating and separating suspended cells based on their intrinsic dielectric characteristics without the need for labeling procedure. A good practice, beyond the physical and engineering components, is the selection of a buffer that does not hinder cellular and biochemical parameters as well as cell recovery. In the present work the impact of four buffers on biochemical, morphological, and mechanical parameters was evaluated in two different cancer cell lines (Caco-2 and K562). Specifically, MTT ([3-(4,5-dimethylthiazol-2-yl)-2,5-diphenyltetrazolium bromide]) assay along with flow cytometry analysis were used to evaluate the occurring changes in terms of cell viability, morphology, and granulocyte stress formation, all factors directly influencing DEP sorting capability. Quantitative real-time PCR (qRT-PCR) was instead employed to evaluate the gene expression levels of interleukin-6 (IL-6) and inducible nitric oxide synthase (iNOS), two well-known markers of inflammation and oxidative stress, respectively. An additional marker representing an index of cellular metabolic status, i.e. the expression of glyceraldehyde-3-phosphate dehydrogenase (GAPDH) gene, was also evaluated. Among the four buffers considered, two resulted satisfactory in terms of cell viability and growth recovery (24 h), with no significant changes in cell morphology for up to 1 h in suspension. Of note, gene expression analysis showed that in both cell lines the apparently non-cytotoxic buffers significantly modulated IL-6, iNOS, and GAPDH markers, underlining the importance to deeply investigate the molecular and biochemical changes occurring during the analysis, even at apparently non-toxic conditions. The selection of a useful buffer for the separation and analysis of cells without labeling procedures, preserving cell status, represents a key factor for DEP analysis, giving the opportunity to further use cells for additional analysis.

"Impact of buffer composition on biochemical, morphological and mechanical parameters: A tare before dielectrophoretic cell separation and isolation"[86], *article published on Translation Oncology, Elsevier.*

International Journal of
Molecular Sciences

MDPI

Review

Label-Free Enrichment of Circulating Tumor Plasma Cells: Future Potential Applications of Dielectrophoresis in Multiple Myeloma

Nicolò Musso [1,2,†], Alessandra Romano [3,*,†], Paolo Giuseppe Bonacci [1], Grazia Scandura [3], Clarissa Pandino [3], Massimo Camarda [2], Giorgio Ivan Russo [4], Francesco Di Raimondo [3], Emma Cacciola [5,6] and Rossella Cacciola [6,7]

1 Department of Biomedical and Biotechnological Sciences (BIOMETEC), University of Catania, 95125 Catania, Italy
2 StLab SRL, 95126 Catania, Italy
3 Department of General Surgery and Surgical Medical Specialties, University of Catania, 95125 Catania, Italy
4 Urology Section, University of Catania, Via S. Sofia 78, 95125 Catania, Italy
5 Department of Medical, Surgical Sciences and Advanced Technologies "G.F. Ingrassia", University of Catania, 95123 Catania, Italy
6 Hemostasis/Hematology Unit, A.O.U. Policlinico "G. Rodolico-San Marco", 95123 Catania, Italy
7 Department of Clinical and Experimental Medicine, University of Catania, 95123 Catania, Italy
* Correspondence: alessandra.romano@unict.it; Tel.: +39-095-378-2971
† These authors contributed equally to this work.

check for updates

Citation: Musso, N.; Romano, A.; Bonacci, P.G.; Scandura, G.; Pandino, C.; Camarda, M.; Russo, G.I.; Di Raimondo, F.; Cacciola, E.; Cacciola, R. Label-Free Enrichment of Circulating Tumor Plasma Cells: Future Potential Applications of Dielectrophoresis in Multiple Myeloma. *Int. J. Mol. Sci.* 2022, 23, 12052. https://doi.org/10.3390/ijms231912052

Abstract: In multiple myeloma (MM), circulating tumor plasma cells (CTPCs) are an emerging prognostic factor, offering a promising and minimally invasive means for longitudinal patient monitoring. Recent advances highlight the complex biology of plasma cell trafficking, highlighting the phenotypic and genetic signatures of intra- and extra-medullary MM onset, making CTPC enumeration and characterization a new frontier of precision medicine for MM patients, requiring novel technological platforms for their standardized and harmonized detection. Dielectrophoresis (DEP) is an emerging label-free cell manipulation technique to separate cancer cells from healthy cells in peripheral blood samples, based on phenotype and membrane capacitance that could be successfully tested to enumerate and isolate CTPCs. Herein, we summarize preclinical data on DEP development for CTPC detection, as well as their clinical and research potential.

Keywords: minimal residual disease; multiple myeloma; acute leukemia; lymphoma

"Label-Free Enrichment of Circulating Tumor Plasma Cells: Future Potential Applications of Dielectrophoresis in Multiple Myeloma"[51], *review published on International Journal of Molecular Sciences, MDPI.*

Automated Electrorotation System for High-Throughput Dielectric Cell Characterization

Samuele Moscato, Andrea Ballo, Pasquale Memmolo, Paolo Bonacci, Nicolò Musso, Maide Bucolo, and Massimo Camarda

***Abstract*— *Objective:* This work presents ROT-QSG, a compact, automated, and user-friendly electrorotation system for label-free dielectric characterization of biological cells, enabling applications in disease diagnosis, drug discovery, and personalized medicine. *Methods:* The ROT-QSG system consists of three main components: (1) a custom electronic device—Quadrature Signal Generator (QSG); (2) a specifically designed electrorotation chip—ROT-chip; and (3) a dedicated image processing algorithm—Pixel Intensity (PxI)—which enables automatic, operator-independent extraction of cell rotation data. Electrorotation allows the dielectric characterization of cells by analyzing their rotational response to varying electric field frequencies, generating the rotation–frequency spectrum (ROT-spectrum). To ensure high consistency and repeatability, the entire experimental workflow—from signal generation to spectrum extraction—has been fully automated through a dedicated experimental control algorithm. *Results:* The system was validated by analyzing three immortalized cell lines (CaCo-2, CCD-841, and OPM2), from which ROT spectra and corresponding cell membrane capacitance values were successfully extracted. *Conclusion:* The comparative study revealed clear differences in membrane capacitance among the three cell types, confirming the system's capability to detect meaningful dielectric variations. The repeatability of measurements within each cell line and the observed distinct spectral differences between the cell lines demonstrate its sensitivity to variations in membrane morphology and structural organization. *Significance:* The system, designed with a strong focus on integration, automation, and ease of use in biological settings, has the potential to enhance dielectric characterization across a wide range of cell types, contributing to a deeper understanding of cellular functions and disease mechanisms.**

***Index Terms*— Electrokinetic, Dielectric cell modeling, Image Processing, Cell differentiation.**

This work was supported by the European Union, Project SAMOTHRACE under Grant ECS00000022. The authors thank the BRIT, University of Catania (Italy), for the use of their laboratories. The authors would also like to thank Prof. Stefania Stefani, University of Catania (Italy), and Prof. Ronald Pethig, University of Edinburgh, Scotland.

Samuele Moscato, Andrea Ballo, and Maide Bucolo are with the Department of Electrical Electronic and Computer Science Engineering, University of Catania, Italy (e-mail: samuele.moscato@phd.unict.it; andrea.ballo@unict.it; maide.bucolo@unict.it).

Pasquale Memmolo is with CNR – Institute of Applied Sciences and Intelligent Systems "Eduardo Caianiello", Pozzuoli, Italy (e-mail: pasquale.memmolo@isasi.cnr.it).

Paolo Bonacci, and Nicolò Musso are with the Department of Biomedical and Biotechnological Sciences, University of Catania, Italy (e-mail: paolo.bonacci@phd.unict.it; nmusso@unict.it).

Massimo Camarda, and Samuele Moscato are with STLab srl, Catania, Italy (e-mail: massimo.camarda@stlab.eu; samuele.moscato@stlab.eu).

I. Introduction

STUDYING the characteristics of cell membranes and cytoplasm is crucial to understanding cellular function and disease mechanisms. The insights of these studies allow for advances in medical research, drug development, and the treatment of diseases such as cancer [1] or neurodegenerative disorders [2]. The progress in technology and research methodologies has led to the development of different approaches for cell characterization, based on fluorescence [3], hydrodynamic [4], optical [5] and electrical systems [6]. In recent years, electrokinetic techniques have emerged as the primary approach for non-invasive, label-free biological cell characterization, separation, and manipulation. Label-free detection provides an effective alternative to traditional labeling methods, often costly, time-consuming, and potentially cytotoxic [7]. Several electrokinetic techniques are currently used for cell characterization [8]–[10], in which cells are modeled as electrical networks to extract their dielectric properties. These techniques can be broadly classified into impedance-based methods, dielectrophoresis (DEP), and electrorotation (ROT).

In impedance-based techniques [11], such as impedance flow cytometry (IFC) [12] and electric impedance spectroscopy (EIS) [13], cell dielectric properties are correlated with the measurement of the amplitude and phase current of a cell sample due to an alternating voltage stimulus (AC) at fixed or variable frequency [14]. This method is accurate, but requires specialized hardware, whereas DEP and ROT utilize simpler, cost-effective systems to induce cell movement using electric fields—non-uniform in DEP [15] and uniform in ROT [16]. Specifically, DEP induces translational movement, while ROT induces rotational motion. In both cases, the analysis of the cell's motion enables the determination of their dielectric characteristics as a function of the applied electrical signal frequencies, deriving the DEP (translation vs frequency) and ROT (rotation vs frequency) spectra, respectively. Typically, the explored frequencies range from 30 kHz up to a few MHz. For frequencies below 1 MHz, cell polarizability is dominated by the membrane's high resistance, while above, the membrane's resistance progressively shorts out due to its capacitance, allowing the electric field to penetrate into the cytoplasm [17]. This creates the opportunity, using broadband signal generators, to characterize both the cell membrane [18] and cytoplasm [19]. Additionally, unlike impedance-

"Automated Electrorotation System for High-Throughput Dielectric Cell Characterization"[98]*, article published on IEEE Transactions on Biomedical Engineering.*

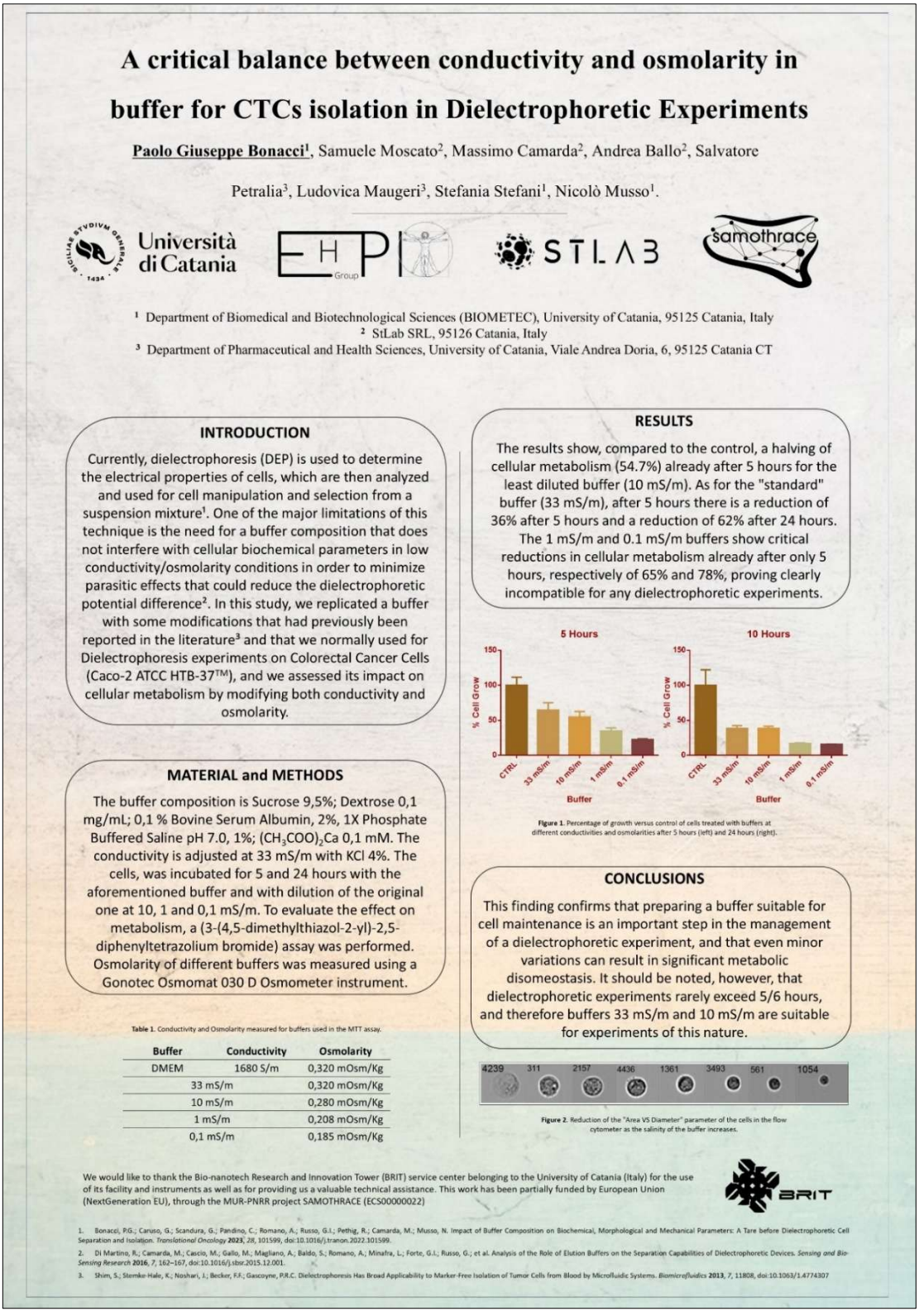

A critical balance between conductivity and osmolarity in buffer for CTCs isolation in Dielectrophoretic Experiments

Paolo Giuseppe Bonacci[1], Samuele Moscato[2], Massimo Camarda[2], Andrea Ballo[2], Salvatore Petralia[3], Ludovica Maugeri[3], Stefania Stefani[1], Nicolò Musso[1].

[1] Department of Biomedical and Biotechnological Sciences (BIOMETEC), University of Catania, 95125 Catania, Italy
[2] StLab SRL, 95126 Catania, Italy
[3] Department of Pharmaceutical and Health Sciences, University of Catania, Viale Andrea Doria, 6, 95125 Catania CT

INTRODUCTION

Currently, dielectrophoresis (DEP) is used to determine the electrical properties of cells, which are then analyzed and used for cell manipulation and selection from a suspension mixture[1]. One of the major limitations of this technique is the need for a buffer composition that does not interfere with cellular biochemical parameters in low conductivity/osmolarity conditions in order to minimize parasitic effects that could reduce the dielectrophoretic potential difference[2]. In this study, we replicated a buffer with some modifications that had previously been reported in the literature[3] and that we normally used for Dielectrophoresis experiments on Colorectal Cancer Cells (Caco-2 ATCC HTB-37™), and we assessed its impact on cellular metabolism by modifying both conductivity and osmolarity.

MATERIAL and METHODS

The buffer composition is Sucrose 9,5%; Dextrose 0,1 mg/mL; 0,1 % Bovine Serum Albumin, 2%, 1X Phosphate Buffered Saline pH 7.0, 1%; $(CH_3COO)_2Ca$ 0,1 mM. The conductivity is adjusted at 33 mS/m with KCl 4%. The cells, was incubated for 5 and 24 hours with the aforementioned buffer and with dilution of the original one at 10, 1 and 0,1 mS/m. To evaluate the effect on metabolism, a (3-(4,5-dimethylthiazol-2-yl)-2,5-diphenyltetrazolium bromide) assay was performed. Osmolarity of different buffers was measured using a Gonotec Osmomat 030 D Osmometer instrument.

Table 1. Conductivity and Osmolarity measured for buffers used in the MTT assay.

Buffer	Conductivity	Osmolarity
DMEM	1680 S/m	0,320 mOsm/Kg
33 mS/m		0,320 mOsm/Kg
10 mS/m		0,280 mOsm/Kg
1 mS/m		0,208 mOsm/Kg
0,1 mS/m		0,185 mOsm/Kg

RESULTS

The results show, compared to the control, a halving of cellular metabolism (54.7%) already after 5 hours for the least diluted buffer (10 mS/m). As for the "standard" buffer (33 mS/m), after 5 hours there is a reduction of 36% after 5 hours and a reduction of 62% after 24 hours. The 1 mS/m and 0.1 mS/m buffers show critical reductions in cellular metabolism already after only 5 hours, respectively of 65% and 78%, proving clearly incompatible for any dielectrophoretic experiments.

Figure 1. Percentage of growth versus control of cells treated with buffers at different conductivities and osmolarities after 5 hours (left) and 24 hours (right).

CONCLUSIONS

This finding confirms that preparing a buffer suitable for cell maintenance is an important step in the management of a dielectrophoretic experiment, and that even minor variations can result in significant metabolic disomeostasis. It should be noted, however, that dielectrophoretic experiments rarely exceed 5/6 hours, and therefore buffers 33 mS/m and 10 mS/m are suitable for experiments of this nature.

Figure 2. Reduction of the "Area VS Diameter" parameter of the cells in the flow cytometer as the salinity of the buffer increases.

We would like to thank the Bio-nanotech Research and Innovation Tower (BRIT) service center belonging to the University of Catania (Italy) for the use of its facility and instruments as well as for providing us a valuable technical assistance. This work has been partially funded by European Union (NextGeneration EU), through the MUR-PNRR project SAMOTHRACE (ECS00000022)

1. Bonacci, P.G.; Caruso, G.; Scandura, G.; Pandino, C.; Romano, A.; Russo, G.I.; Pethig, R.; Camarda, M.; Musso, N. Impact of Buffer Composition on Biochemical, Morphological and Mechanical Parameters: A Tare before Dielectrophoretic Cell Separation and Isolation. *Translational Oncology* **2023**, *28*, 101599, doi:10.1016/j.tranon.2022.101599.
2. Di Martino, R.; Camarda, M.; Cascio, M.; Gallo, M.; Magliano, A.; Baldo, S.; Romano, A.; Minafra, L.; Forte, G.I.; Russo, G.; et al. Analysis of the Role of Elution Buffers on the Separation Capabilities of Dielectrophoretic Devices. *Sensing and Bio-Sensing Research* **2016**, *7*, 162–167, doi:10.1016/j.sbsr.2015.12.001.
3. Shim, S.; Stemke-Hale, K.; Noshari, J.; Becker, F.F.; Gascoyne, P.R.C. Dielectrophoresis Has Broad Applicability to Marker-Free Isolation of Tumor Cells from Blood by Microfluidic Systems. *Biomicrofluidics* **2013**, *7*, 11808, doi:10.1063/1.4774307

"A critical balance between conductivity and osmolarity in buffer for CTCs isolation in Dielectrophoretic Experiments", poster accepted and presented at 62° Congresso della Società Italiana di Biochimica e Biologia Molecolare (SIB), Firenze 7-9 September 2023.

P-17-021

RELATIONSHIP BETWEEN ELECTROROTATION SPECTRUM AND MEMBRANE ASSOCIATED REGION1 BINDING PROTEIN (SMAR1) AND FOCAL ADHESION KINASE (FAK) GENE EXPRESSION.

P.G. Bonacci[1], S. Moscato[2], M. Camarda[2], M. Bucolo[3], S. Stefani[1], **N. Musso**[1]

[1] Department of Biomedical and Biotechnological Sciences, University of Catania, Catania, Italy
[2] StLab SRL, Catania, Italy
[3] Department of Electrical, Electronic and Computer Engineering, Catania (CT), Italy

BACKGROUND

The potential correlations between the genes *SMAR1* and *PTK2* and cellular membrane alterations have garnered significant research interest due to their implications in cancer biology. In this study, we extended our previous evaluation of the membrane genes *SMAR1*, *CK8*, and *PTK2* by including a third cell line, HCT-116, alongside CCD-841 (healthy colon) and CaCo-2 (colon adenocarcinoma). We aimed to investigate the differential expression of these genes across the three cell lines and explore their potential correlations with variations in electrorotation. Our findings provide a comprehensive analysis of gene expression profiles and their potential impact on the biophysical properties of cellular membranes in healthy and cancerous colon cells. This study offers new insights into the role of membrane-associated genes in colorectal cancer and underscores the importance of understanding gene expression dynamics in the context of cellular membrane behavior.

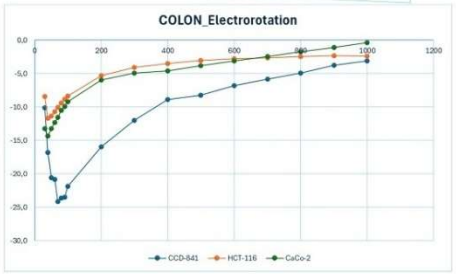

Figure 2. Variation of the rotational speed of the three cell lines as the frequency varies.

DISCUSSION

Our results on gene expression are in agreement with the literature: the *SMAR1* gene, commonly known as anti-oncogenic and whose activity is also related to TP53, is more expressed in healthy cells than in tumor cells. On the other hand, abnormal activation or overexpression of PTKs is frequently associated with various cancers. In fact, HCT-116 and CaCo-2 cells express *PTK* more than CCD-841 cells. In addition to its anti-oncogenic role, it has been demonstrated that *SMAR1* is involved in the reorganization of the cell membrane. Specifically, the greater its expression, the greater the smoothness of the membrane. This is also highlighted by the electrorotation experiment: CCD-841 cells, having a smoother structure, are able to reach greater speeds compared to the other two tumor lines which, expressing less *SMAR1*, offer more resistance to rotation due to greater membrane roughness.

MATERIALS

The CCD-841, CaCo-2 and HCT-116 cell lines were grown in their respective media [1]. The expression of *SMAR1* and *FAK* genes was evaluated via RTqPCR, with gene expression normalized to the β-actin. For electrorotation experiments, cells were washed and resuspended in an appropriate buffer [1] up to a final concentration of 150 cells/μL. Cells were then subjected to ER in an engineered plug-and-play chamber using a prototypal DEP chip (Figure 1), administering a frequency range of 10^4-10^7 Hz, and evaluating their velocity (ω) in radians per second.

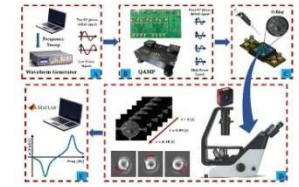

Figure 1A. Working principle schematic: (A) Low-power signal generations, (B) high-power quadrature stage, (C) ER-Device, (D) sensing and acquisition, and (E) offline analysis and result evaluation.

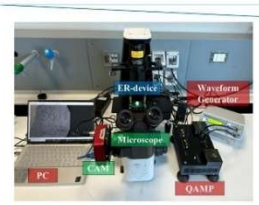

Figure 1B. experimental setup

RESULTS

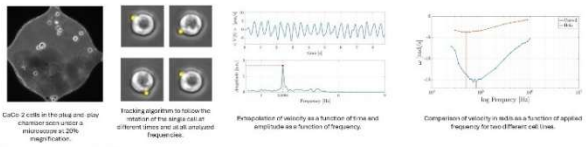

CaCo-2 cells in the plug and play chamber seen under a microscope in 20X magnification.

Tracking algorithm to follow the rotation of the single cell at different times and at all analyzed frequencies.

Extrapolation of velocity as a function of time and amplitude as a function of frequency.

Comparison of velocity in rad/s as a function of applied frequency for two different cell lines.

Our results show how there is a direct correlation between *SMAR1* expression and different behavior in electrorotation. Basically, it seems like the greater the expression of *SMAR1*, the greater the change in speed of the cell line as the frequency varies (Figure 2). RT-qPCR showed that healthy CCD-841 cells present the highest expression of SMAR1, CaCo-2 an intermediate situation while the lowest expression of *SMAR1* is presented by HCT-116. At the same time, the CCD-841 have speed values expressed in rad/s ranging from -3 to -24, the CaCo-2 from -0.6 to -14.3 and the HCT-116 from -2.3 to - 11.7. PTK expression, on the other hand, follows a diametrically opposite trend, with the highest expression value reported by HCT-116 and the lowest by CCD-841, with CaCo-2 always placed in the middle.

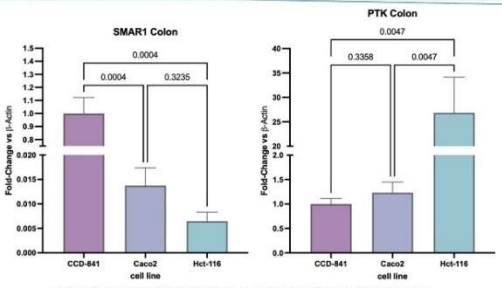

Figure 2. Expressions of the SMAR1 and PTK genes for the different cell lines normalized for beta actin.

CONCLUSIONS and PERSPECTIVES

Our study elucidates the significant correlations between the expression of SMAR1 and PTK2 genes and the biophysical properties of cellular membranes in both healthy and cancerous colon cells. These findings provide a comprehensive understanding of how membrane-associated gene expression influences cellular behavior, particularly in the context of colorectal cancer. The observed variations in electrorotation velocities among the cell lines offer a novel perspective on the mechanical properties of cell membranes, potentially paving the way for new diagnostic and therapeutic approaches. Future research should focus on further elucidating the molecular mechanisms underlying these correlations and exploring the broader implications of membrane gene expression in cancer biology. By integrating these insights with clinical data, we can enhance our understanding of cancer progression and develop more effective strategies for diagnosis and treatment.

[1] Bonacci, Paolo G et al. "Impact of buffer composition on biochemical, morphological and mechanical parameters: A tare before dielectrophoretic cell separation and isolation." *Translational oncology* vol. 28 (2023): 101599. doi:10.1016/j.tranon.2022.101599

We would like to thank the Bio-nanotech Research and Innovation Tower (BRIT) service center belonging to the University of Catania (Italy) for the use of its facility and instruments as well as for providing us a valuable technical assistance. This work has been partially funded by European Union (NextGeneration EU), through the MUR-PNRR project SAMOTHRACE (ECS00000022)

"Relationship Between Electrorotation Spectrum And Membrane Associated Region1 Binding Protein (SMAR1) And Focal Adhesion Kinase (FAK) Gene Expression", poster accepted and presented at 48° Federation of European Biochemical Societies (FEBS) Congress, Milan 29 June – 3 July 2024

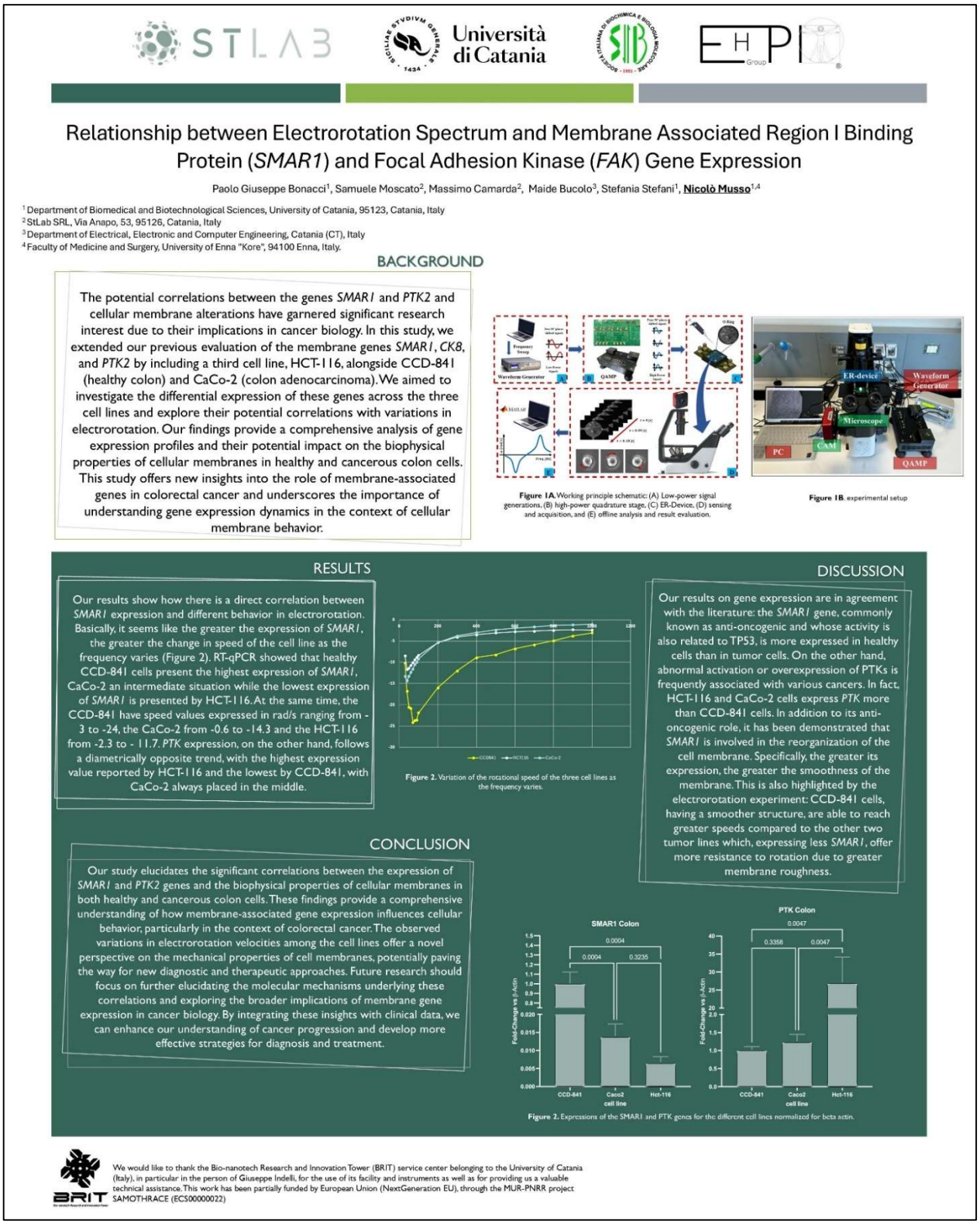

"Relationship Between Electrorotation Spectrum And Membrane Associated Region1 Binding Protein (SMAR1) And Focal Adhesion Kinase (FAK) Gene Expression", poster accepted and presented at 4° Tumor Biochemistry group of Società Italiana di Biochimica e Biologia Molecolare (SIB), Catania 16-17 September 2024.

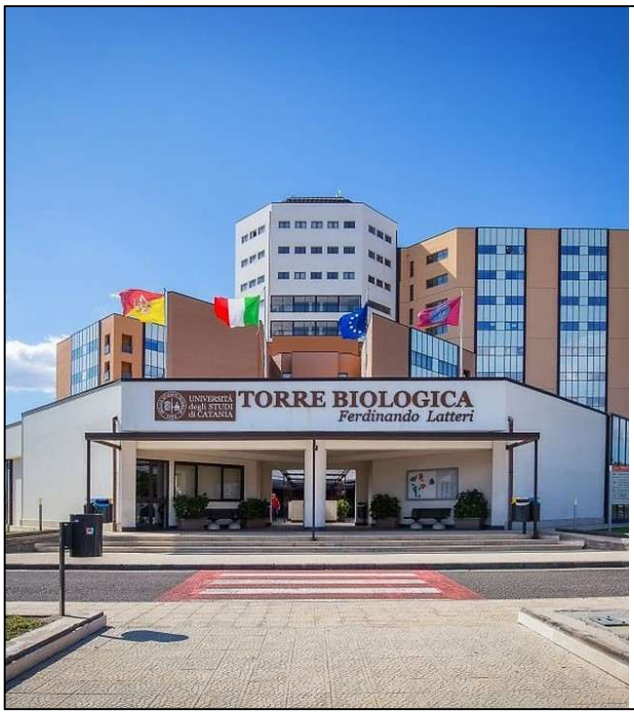

EXPLORING THE INFLUENCE OF BIO-ELECTROCHEMICAL PROPERTIES AND MEMBRANE ROUGHNESS ON PATHOLOGICAL CELL DETECTION IN LIQUID BIOPSIES VIA DIELECTROPHORESIS EXPERIMENTS

Dr. Bonacci Paolo Giuseppe, PhD student

~

Dipartimento di Scienze Biomediche e Biotecnologiche

Sezione di Biochimica Medica

IX Retreat Dipartimentale

12-13 Gennaio 2024 | Four Points Sheraton Catania

Exploring the Influence of Bio-electrochemical Properties and Membrane Roughness on Pathological Cell Detection in Liquid Biopsies via Dielectrophoresis Experiments, presentation at the IX Department Retreat of the Department of Biomedical and Biotechnological Sciences of the University of Catania, Section of Medical Biochemistry, Catania, 12-13 January 2024.

You have access | Journal of Urology | Prostate Cancer: Markers (IP05) | 1 May 2025

IP05-09 LABEL-FREE CHARACTERIZATION OF PROSTATE CANCER CELLS: A NOVEL AUTOMATED ELECTRO CELL-PHYSIOMETRY (ECP) PLATFORM FOR LIQUID BIOPSY. BIOPSY

Samuele Moscato, Giorgio Ivan Russo, Pasquale Memmolo, Bonacci Paolo, Nicolò Musso, Stefania Stefani, Maide Bucolo, and Massimo Camarda

View All Author Information

https://doi.org/10.1097/01.JU.0001109816.50355.3c.09

"Label-Free Characterization of Prostate Cancer Cells: a Novel Automated Electro Cell-Physiometry (ECP) Platform for Liquid Biopsy"[128]*, abstract Published on The Journal of Urology, Official Journal of the American Urological Association, AUA Journals.*

A critical balance between conductivity and osmolarity in buffers for Dielectrophoretic and Electrorotation experiments

Paolo Bonacci[1], Samuele Moscato[2,3], Andrea Ballo[2], Stefania Stefani[1], Nicolò Musso[1], Maide Bucolo[2], Massimo Camarda[3]

[1]*Department of Biomedical and Biotechnological Sciences (BIOMETEC), University of Catania, 95125 Catania, Italy*

[2]*Department of Electrical Electronic and Computer Science Engineering, University of Catania, Italy*

[3]*STLab SRL, 95126 Catania, Italy*

Dielectrophoresis (DEP) and Electrorotation (ER) are nowadays extensively used to determine the dielectric properties of cells [1]. One of the limitations of these techniques is the need for low conductivity buffers which do not interfere with cellular biochemical parameters, in order to reduce/minimize parasitic effects altering their electrokinetics or biological responses [2]. In the present work the impact of four buffers on biochemical, morphological, and mechanical parameters was evaluated in two different cancer cell lines (Caco-2 and K562) [3]. Specifically, MTT ([3-(4,5-dimethylthiazol-2-yl)-2,5-diphenyltetrazolium bromide]) assays along with flow cytometry analysis were used to evaluate the occurring changes in terms of cell viability, morphology, and granulocyte stress formation, all factors directly influencing DEP/ER biocompatibility. Quantitative real-time PCR (qRT-PCR) was instead employed to evaluate the gene expression levels of interleukin-6 (IL-6) and inducible nitric oxide synthase (iNOS), two well-known markers of inflammation and oxidative stress, respectively. An additional marker representing an index of cellular metabolic status, i.e., the expression of glyceraldehyde-3-phosphate dehydrogenase (GAPDH) gene, was also evaluated. Among the four considered buffers, two resulted superiors, in terms of cell viability and growth recovery (24 h), with no significant changes in cell morphology for up to 1 h of cells suspension. Of note, gene expression analysis showed that in both cell lines the apparently non-cytotoxic buffers significantly modulated IL-6, iNOS, and GAPDH markers, underlining the importance to deeply investigate the molecular and biochemical changes occurring during the analysis, even at apparently non-toxic conditions. The selection of a useful buffer for the separation and analysis of cells without labeling procedures, preserving cell status, represents a key factor for DEP/ER analysis, giving the opportunity to further use cells for additional analysis.

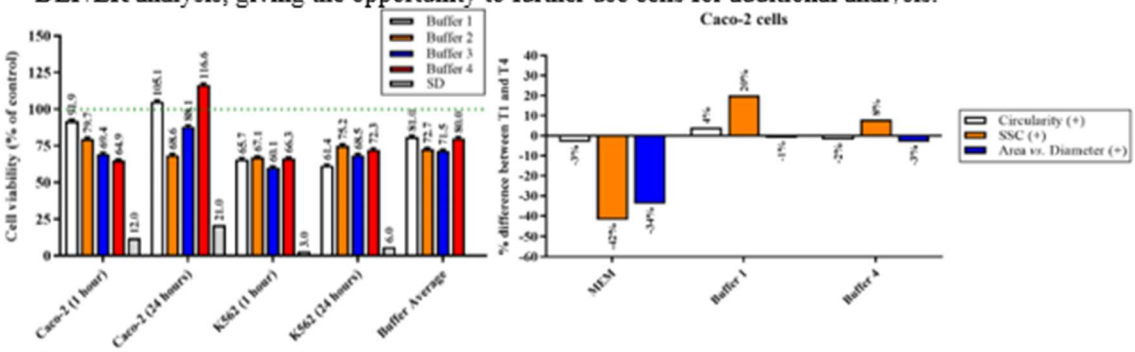

Fig. 1 Left) Changes in cell viability of Caco-2 and K562 cells in the presence of the four different buffers after 1 h and 24 h. Data are the mean of four values and are expressed as the percent variation with respect to the absorbance at 569 nm detected in cells grown in the presence of MEM (physiological cell culture medium; dotted line). SD = standard deviations among the four buffers for a specific condition; Buffer Average = mean of the four cell viability (%) values (Caco-2 at 1 h and 24 h; K562 at 1 h and 24 h) measured for each buffer. **Right)** Percentage (%) difference of the three parameters between the start time point (T1) and the endpoint (T4). Difference was calculated as follows: (Parameter value at T4 – Parameter value at T1)/100.

[1] E. A. Hnslee, Electrophoresis, 4, 1915 (2020)
[2] P.G. Bonacci et al. Translational Oncology 28, 101599 (2023)
[3] Di Martino et al. Devices. Sensing and Bio-Sensing Research 7, 162 (2016)

"A critical balance between conductivity and osmolarity in buffers for Dielectrophoretic and Electrorotation experiments", poster presented at Dielectrophoresis Conference 2024, UCD O'Brien Science Centre, University College Dublin (Ireland), July 1st-July 3rd.

AN AUTOMATED ELECTRO-CELL PHYSIOMETRY (ECP) PLATFORM BASED ON BROAD-BAND (30 kHz-300 MHz) ELECTROROTATION AND DIELECTROPHORESIS.

Samuele Moscato[1,2], Andrea Ballo[1,2], Pasquale Memmolo[4], Paolo Bonacci[3], Nicolò Musso[3], Stefania Stefani[3], Ron Pethig[1], Maide Bucolo[2] and Massimo Camarda[1]

[1]STLab srl, Catania, Italy

[2] Department of Electrical Electronic and Computer Science Engineering, University of Catania, Italy

[3] Department of Biomedical and Biotechnological Sciences, University of Catania, Italy

[4] CNR – Institute of Applied Sciences and Intelligent Systems "Eduardo Caianiello", via Campi Flegrei 34, 80070 Pozzuoli (Italy)

We report the development of a customized, integrated, and automated platform, optimized for electrokinetic characterization of cells from 30 kHz up to 300 MHz. The platform enables the assessment of cell properties through the measurement of membrane capacitance, cytoplasmic conductivity, and nuclear volume fluctuations. The platform is designed to provide a comprehensive and high-throughput analysis of cellular electrokinetics, with the ability to detect changes in cell behavior. This platform will find extensive application in different fields, including medical research, biotechnology, and pharmaceuticals, where the characterization of cell viability is crucial for the understanding of disease mechanisms, drug discovery, and the development of new therapies. The platform (Fig.1) comprises a broad frequency range quadrature signal amplifier (HF-QAMP) capable of supplying large enough power to allow for the simultaneous electrorotation (*ER*) plus dielectrophoresis (*DEP*) of multiple cells up to 300 MHz (Fig.2). An ad-hoc designed PCB system (*DEP & ER-chamber*), which minimize parasitic capacitances, permit operations at high MHz frequencies; a fast and robust image processing algorithm automatically track and extract multi-cell *DEP*- and *ER*-spectrums. The *Electro-Cell Physiometry (ECP)* Platform was validated using CaCo-2 ATCC HTB-37™ cells. Specifically, the electrorotation spectra were generated using up to $18V_{pp}$ voltages, which allowed simultaneous rotations, at high rotational velocities, of multiple cells at once. For each frequency, a video of a few seconds, less than 10, was sufficient for automatically extracting the rotational velocities. Two different cell rotation extraction algorithms were tested, the first algorithm used a correlation-based method, while the second algorithm, known as PiXel Intensity (PxI), was based on a new approach to analyzing the luminosity variation in pixels. Both algorithms provide periodic signals that were used to automatically determine the angular velocities of cells with great accuracy, as shown in Figure 3. The current work is aimed at integrating the signal generator and quadrature stage into a single unit. This development is intended to make the system more compact and easy to use in biological laboratory environments.

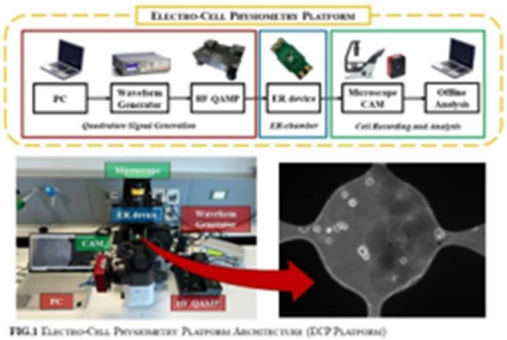

FIG.1 Electro-Cell Physiometry Platform Architecture (ECP Platform)

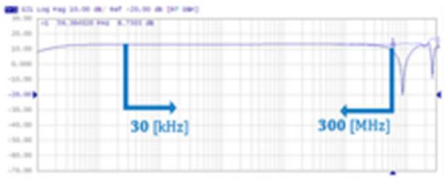

FIG.2 Bandwidth analysis of the ER-QAMP (3dB up to 300MHz)

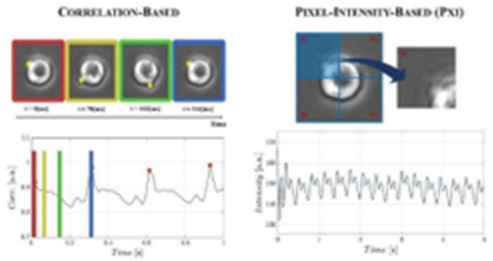

FIG.3 Overview of extraction algorithms

"An Automated Electro Cell-Physiometry (ECP) Platform Based on Broad-Band (30 kHz–300 MHz) Electrorotation and Dielectrophoresis", poster presented at Dielectrophoresis Conference 2024, UCD O'Brien Science Centre, University College Dublin (Ireland), July 1st-July 3rd.

6.2. OTHER PUBLICATIONS AND CONTRIBUTIONS

-Musso, N.; **Bonacci, P.G.;** Consoli, G.M.L.; Maugeri, L.; Terrana, M.; Lanzanò, L.; Longo, E.; Buscarino, G.; Consoli, A.; Petralia, S. *Biofriendly glucose-derived carbon nanodots: GLUT2-mediated cell internalization for an efficient targeted drug delivery and light-triggered cancer cell damage*. Journal of Colloid and Interface Science, **2025,** 137873, doi:10.1016/j.jcis.2025.137873.

- Maugeri, L.; Fangano, G.; Butera, E.; Forte, G.; **Bonacci, P.G.**; Musso, N.; Ruffino, F.; Ferreri, L.; Consoli, G.M.L.; Petralia, S. *Emissive Pentacene-Loaded βcyclodextrin-Derived C-Nanodots Exhibit Red-Light Triggered Photothermal Effect*. Pharmaceutics **2025**, 17, 543. https://doi.org/10.3390/pharmaceutics17050543

- Privitera, G.F., Musso, N., Micale, G., Bonomo, C., Alaimo, S., Bivona, D., **Bonacci, P.G.,** Scalia, G., Stefani, S., Pulvirenti, A. *CovidTGI: a tool to investigate the Temporal Genetic Instability of SARS-CoV-2 variants*, iScience **2025**, https://doi.org/10.1016/j.isci.2025.112315.

- Maniaci, A., **Bonacci, P.**, Stefani, S., Cocuzza, S., Merlino, F., Saibene, A.M., Sangiorgio, G., Maza-Solano, J., Lechien, J.R., La Mantia, I. and Musso, N. (2024), *Influence of Single Nucleotide Polymorphisms on CRS Outcomes: A Preliminary Observational Study.* The Laryngoscope, **2024**. https://doi.org/10.1002/lary.31719

- Mirabile, A., Sangiorgio, G., **Bonacci, P.G.,** Bivona, D., Nicitra, E., Bonomo, C., Bongiorno, D., Stefani, S., Musso, N. Advancing Pathogen Identification*: The Role of Digital PCR in Enhancing Diagnostic Power in Different Settings*. Diagnostic, **2024** 14, 598. https://doi.org/10.3390/diagnostics14151598.

- Consoli, G.M.L., Maugeri, L., Musso, N., Gulino, A., D'Urso, L., **Bonacci**, **P.**,

Buscarino, G., Forte, G. and Petralia, S. *One-Pot Synthesis of Luminescent and Photothermal Carbon Boron-Nitride Quantum Dots Exhibiting Cell Damage Protective Effects*, Advanced Healthcare Materials **2024**, https://doi.org/10.1002/adhm.202303692.

- Bivona, D.; Bonomo, C.; Colombini, L.; **Bonacci, P.G.**; Privitera, G.F.; Caruso, G.; Caraci, F.; Santoro, F.; Musso, N.; Bongiorno, D.; et al. *Generation and Characterization of Stable Small Colony Variants of USA300 Staphylococcus aureus in RAW 264.7 Murine Macrophages*. Antibiotics **2024**, 13, 264. https://doi.org/10.3390/antibiotics13030264

- Sangiorgio, G.; Nicitra, E.; Bivona, D.; Bonomo, C.; **Bonacci, P.**; Santagati, M.; Musso, N.; Bongiorno, D.; Stefani, S. *Interactions of Gram-Positive Bacterial Membrane Vesicles and Hosts: Updates and Future Directions*. Int. J. Mol. Sci. **2024**, 25, 2904. https://doi.org/10.3390/ijms25052904

- Longhitano, L.; Distefano, A.; Musso, N.; **Bonacci, P.**; Orlando, L.; Giallongo, S.; Tibullo, D.; Denaro, S.; Lazzarino, G.; Ferrigno, J.; et al. *(+)-Lipoic Acid Reduces Mitochondrial Unfolded Protein Response and Attenuates Oxidative Stress and Aging in an in Vitro Model of Non-Alcoholic Fatty Liver Disease*. Journal of Translational Medicine **2024**, 22, 82, doi:10.1186/s12967-024-04880-x.

-Cubisino, S.A.M., Conti Nibali, S., Musso, N., **Bonacci, P.,** De Pinto, V., Ceccarelli, M., Reina, S., *Electrophysiological properties and structural prediction of the SARS-CoV-2 viroprotein E*, Front. Mol. Biosci. **2024**, 11, doi: 10.3389/fmolb.2024.1334819. (A4, A5)

-Consoli, G.M.L., Maugeri, L., Forte, G., Buscarino, G., Gulino, A., Lanzanò, L., **Bonacci, P.,** Musso, N. *Red Light-Triggerable Nanohybrid of Graphene Oxide, Gold Nanoparticles and Thermo-Responsive Polymer for Combined Photothermia and Drug Release Effects,* Journal of Materials Chemistry B, **2023**, https://doi.org/10.1039/D3TB01863F

-Musso, N., Bivona, D., Bonomo, C., **Bonacci, P.**, D'Ippolito, M. E., Boccagni, C., Rubino, F., De Tanti, A., Lucca, L. F., Pingue, V., Colombo, V., Estraneo, A., Stefani, S., Andriolo, M., & Bagnato, S. (2023). *Investigating microRNAs as biomarkers in disorders of consciousness: a longitudinal multicenter study*. Scientific reports, 13(1), 18415. https://doi.org/10.1038/s41598-023-45719-7

-Bonomo, C.; **Bonacci, P.G.**; Bivona, D.A.; Mirabile, A.; Bongiorno, D.; Nicitra, E.; Marino, A.; Bonaccorso, C.; Consiglio, G.; Fortuna, C.G.; et al. *Evaluation of the Effects of Heteroaryl Ethylene Molecules in Combination with Antibiotics: A Preliminary Study on Control Strains*. Antibiotics **2023**, 12, 1308. https://doi.org/10.3390/antibiotics12081308

-Russo, G.I.; **Bonacci, P**.; Bivona, D.; Privitera, G.F.; Broggi, G.; Caltabiano, R.; Vella, J.; Lo Giudice, A.; Asmundo, M.G.; Cimino, S.; Morgia, G.; Stefani, S.; Musso, N. *Genomic Landscape Alterations in Primary Tumor and Matched Lymph Node Metastasis in Hormone-Naïve Prostate Cancer Patients*. Cancers **2022**, 14, 4212. DOI: https://doi.org/10.3390/cancers14174212

-Russo, G.I.; Musso, N.; Lo Giudice, A.; Asmundo, M.G.; Di Mauro, M.; **Bonacci, P.G.**; Massimino, M.; Bivona, D.; Stefani, S.; Pricoco, E.; Ferro, M.; Camarda, M.; Cimino, S.; Morgia, G.; Caltabiano, R.; Broggi, G.; *PD-1, PD-L1 and cAMP immunohistochemical expressions are associated with worse oncological outcome in patients with bladder cancer*, J Cancer Res Clin Oncol (**2022**), DOI: https://doi.org/10.1007/s00432-022-04262-0.

-Marino, A.; Bivona, A.; **Bonacci, P.** *Updates in central nervous system malaria: literature review and considerations*, Current Opinion in Infectious Diseases: June **2022** - Volume 35 - Issue 3 - p 255-261 DOI: 10.1097/QCO.0000000000000829

-Bivona, D.A.; Mirabile, A.; Bonomo, C.; **Bonacci, P.G**.; Stracquadanio, S.; Marino, A.; Campanile, F.; Bonaccorso, C.; Fortuna, C.G.; Stefani, S.; Musso, N.; Bongiorno,

D. *Heteroaryl-Ethylenes as New Effective Agents for High Priority Gram-Positive and Gram-Negative Bacterial Clinical Isolates.* Antibiotics **2022**, 11, 767. DOI: 10.3390/antibiotics11060767

-Musso, N.; **Bonacci, P.G.**; Bongiorno, D.; Stracquadanio, S.; Bivona, D.A.; Palermo, C.I.; Scalia, G.; Fichera, M.; Stefani, S. *Discriminatory Weight of SNPs in Spike SARS-CoV-2 Variants: A Technically Rapid, Unambiguous, and Bioinformatically Validated Laboratory Approach.* Viruses **2022**, 14, 123. DOI: 10.3390/v14010123

- Musso, N.; **Bonacci, P**.; Bivona, D.; Bonomo, C.; Bongiorno, D.; Stefani, S. *Robust, rapid discrimination of SARS-CoV-2 variants of concern from heterogeneous RNA samples by NGS using the QIAseq® DIRECT SARS-CoV-2 Kit,* White Paper published by QIAGEN®, **2021**.

-Bonacci, P.G.; Bivona, D.A.; Bongiorno, D.; Stracquadanio, S.; Massimino, M.; Bonomo, C.; Stracuzzi, A.; Pennisi, P.; Musso, N.; Stefani, S. *Low Represented Mutation Clustering in SARS-CoV-2 B.1.1.7 Sublineage Group with Synonymous Mutations in the E Gene*. Diagnostics **2021**, *11*, 2286. DOI: 10.3390/diagnostics11122286

-Bongiorno, D.; Musso, N.; **Bonacci, P.G**.; Bivona, D.A.; Massimino, M.; Stracquadanio, S.; Bonaccorso, C.; Fortuna, C.G.; Stefani, S. Heteroaryl-Ethylenes as New Lead Compounds in the Fight against High Priority Bacterial Strains. Antibiotics **2021**, *10*, 1034. DOI: 10.3390/antibiotics10091034.

The list presented includes works published during the three standard doctoral years (October 2022–October 2025). For a complete and updated list:

Scopus ID: 57240802600

ORCID: https://orcid.org/0000-0002-7305-7433

6.3. PARTICIPATION IN NATIONAL AND INTERNATIONAL CONFERENCES

- G. Zerbo, **P.G. Bonacci**, M. Terrana, G. Savoca and N. Musso, *Biological Effects of Green-Extracted Pistachio Derivatives on Colorectal Cancer Cells: Friend or Foe?* Poster accepted and presented at 63rd Congress of the Italian Society of Biochemistry and Molecular Biology, Palermo, 10-12 September 2025.

- M. Terrana, **P.G. Bonacci**, L. Maugeri, S. Petralia and N. Musso, *Nanoparticle-Mediated Delivery of K. pneumoniae DNA into Breast Cancer Cells: a Functionalization and Internalization Study.* Poster accepted and presented at 63rd Congress of the Italian Society of Biochemistry and Molecular Biology, Palermo, 10-12 September 2025.

- **P.G. Bonacci**, A. Costantino, M. Terrana, G. Zerbo, T. Luca, G. Magro, S. Castorina, M. Gulisano and N. Musso, *Geospatial Tracking of Tumor-Associated SNPs: Allele Frequency Gradients in Adjacent and Normal Colorectal Tissues.* Poster accepted and presented at 63rd Congress of the Italian Society of Biochemistry and Molecular Biology, Palermo, 10-12 September 2025.

- **P.G. Bonacci**, L. Maugeri, R. Vinciguerra, G. Scandura, A. Romano, L. Lanzanò, S. Stefani, S. Petralia, N. Musso. *Dynamic Regulation of Glucose Transporter Expression in Colorectal Cell Lines: a Proof of Concept for Tumor Targeting Strategies via Nanoparticles Delivery*. Short communication at Intersections Meeting, Joint annual meeting of the Puglia-Basilicata-Calabria and Sicily sections of the Italian Society of Biochemistry and Molecular Biology (SIB), Messina, 3-5 October 2024.

- **P.G. Bonacci**, L. Maugeri, R. Vinciguerra, G. Scandura, A. Romano, L. Lanzanò, S. Stefani, S. Petralia, N. Musso. *Dynamic Regulation of Glucose Transporter Expression in Colorectal Cell*

Lines: a Proof of Concept for Tumor Targeting Strategies via Nanoparticles Drug Delivery, poster accepted and presented at the 48th congress of the Federation of European Biochemical Societies (FEBS), Milan, 29 June – 3 July 2024.

- **P.G. Bonacci**, L. Maugeri, S. Petralia, D.A. Bivona, D. Bongiorno, S. Stefani and N. Musso, *A zeta potential study to measure S. aureus adhesion on human bone osteosarcoma cells*. Poster accepted and presented at the 34th European Congress of Clinical Microbiology and Infectious Diseases (ECCMID), Barcelona, 27-30 April 2024.

- **P.G. Bonacci**, C. Bonaccorso, G. Consiglio, C.G. Fortuna, S. Stefani and N. Musso, *Variation of gene expression and analogies with 5-Fluorouracil of two novel ethylene heteroaryl compounds*. Poster accepted and presented at 62nd Congress of the Italian Society of Biochemistry and Molecular Biology, Florence, 7-9 September 2023

-C. Bonaccorso, D.A. Bivona, D. Bongiorno, **P.G. Bonacci**, C. Bonomo, A. Mirabile, N. Musso, S. Stracquadanio, C.G. Fortuna and S. Stefani, *"Heteroaryl-ethylenes as new effective agents in the fight against high priority Gram-positive and Gram-negative bacterial clinical isolates".* Poster accepted at XL Convegno Nazionale della Divisione di Chimica Organica della Società Chimica Italiana, Palermo, 11-15 September 2022.

-D. Bivona, C. Bonomo, **P.G. Bonacci**, G. Privitera, N. Musso, G. Caruso, F. Caraci, S. Stefani and D. Bongiorno, "*Preliminary Evaluation of Genomic and Transcriptomic Changes in the Evolution from a USA300 wild-type isolate to SCV, able to perform phagosomal escape".* Poster accepted at the 32nd European Congress of Clinical Microbiology & Infectious Diseases (ECCMID), from 18 to 21 September 2022.

-N. Musso, **P. Bonacci**, D. Bongiorno, S. Stracquadanio, D. A. Bivona, C. I. Palermo, G. Scalia, M. Fichera and S. Stefani. *"Discriminatory Weight of SNPs in Spike SARS-Cov-2 Variants. A technically rapid, unambiguous and bioinformatically validated*

laboratory approach." Poster Presenter at 49th Congresso SIM 2021, Società Italiana di Microbiologia.

-D. Bivona, **P. Bonacci**, C. Bonaccorso, D. Bongiorno, C. Fortuna, S. Stracquadanio, S. Stefani, N. Musso. *"Efficacy of new promising di(heteroaryl)ethenes derivatives on Gram-positive bacteria in vitro and in an infection model"*. Poster accepted at 31 European Congress of Clinical Microbiology & Infectious Diseases (ECCMID), 9-12 July 2021.

7. ACKNOWLEDGMENTS

It seems only fair to finish these pages by expressing my deepest gratitude to those who have supported me throughout this journey. Without their guidance, generosity, and encouragement, this thesis would not have been possible.

I wish to warmly thank Professor Stefania Stefani, for allowing me to develop this research line, for her constant encouragement, and for believing in me far more than I believed in myself.

My heartfelt thanks go to Professors Miguel Viñas and Teresa Vinuesa from the Department of Pathology and Experimental Therapeutics at the University of Barcelona, for hosting me during my six-month research stay abroad and for making this invaluable experience possible.

I would like to express my sincere gratitude to Professors Joanna Wessely-Szponder and Marco Ciordani for their careful review of this thesis and for their valuable suggestions and insights, which greatly contributed to improving the quality and clarity of this work. Their expertise and constructive feedback have been truly appreciated.

I am sincerely grateful to the Departments of Electrical, Electronic and Computer Engineering, and to STLab, for providing the electrorotation device and enabling the dielectrophoretic characterization of the cell lines.

I would also thank Professor Alessandra Romano from the Department of Biomedical and Biotechnological Sciences for providing the suspension of cell lines, allowing their characterization and further enriching this work.

A fundamental contribution was given from the BRIT service center of the University of Catania for granting access to essential instrumentation and facilities for cell culture maintenance, nucleic acid extraction and quantification.

Finally, I express my profound gratitude to Professor Nicolò Musso, who has been by my side from the very beginning. He has been not only the cornerstone of my professional growth but also a guide in my personal growth. His mentorship has taught me not only how to work, but also how to trust my ideas and believe in my own skills.

This work has been partially funded by the European Union (NextGeneration EU), through the MUR-PNRR project SAMOTHRACE (ECS00000022).

8. BIBLIOGRAPHY

1. Hofman, V. *et al.* Detection of circulating tumor cells as a prognostic factor in patients undergoing radical surgery for non-small-cell lung carcinoma: comparison of the efficacy of the CellSearch Assay™ and the isolation by size of epithelial tumor cell method. *Int J Cancer* **129**, 1651–1660 (2011).
2. Deng, Z., Wu, S., Wang, Y. & Shi, D. Circulating tumor cell isolation for cancer diagnosis and prognosis. *EBioMedicine* **83**, 104237 (2022).
3. Zhang, H. *et al.* Detection Methods and Clinical Applications of Circulating Tumor Cells in Breast Cancer. *Frontiers in Oncology* **11**, (2021).
4. Seyfried, T. N. & Huysentruyt, L. C. On the Origin of Cancer Metastasis. *Critical reviews in oncogenesis* **18**, 43 (2013).
5. de Wit, S., van Dalum, G. & Terstappen, L. W. M. M. Detection of Circulating Tumor Cells. *Scientifica (Cairo)* **2014**, 819362 (2014).
6. Hussain, S. H., Huertas, C. S., Mitchell, A., Deman, A.-L. & Laurenceau, E. Biosensors for circulating tumor cells (CTCs)-biomarker detection in lung and prostate cancer: Trends and prospects. *Biosens Bioelectron* **197**, 113770 (2022).
7. Nguyen, T. N. A., Huang, P.-S., Chu, P.-Y., Hsieh, C.-H. & Wu, M.-H. Recent Progress in Enhanced Cancer Diagnosis, Prognosis, and Monitoring Using a Combined Analysis of the Number of Circulating Tumor Cells (CTCs) and Other Clinical Parameters. *Cancers (Basel)* **15**, 5372 (2023).

8. Cristofanilli, M. *et al.* Circulating tumor cells, disease progression, and survival in metastatic breast cancer. *N Engl J Med* **351**, 781–791 (2004).
9. Yang, Y.-P., Giret, T. M. & Cote, R. J. Circulating Tumor Cells from Enumeration to Analysis: Current Challenges and Future Opportunities. *Cancers (Basel)* **13**, 2723 (2021).
10. Paget, S. The distribution of secondary growths in cancer of the breast. 1889. *Cancer Metastasis Rev* **8**, 98–101 (1989).
11. Pote, M. S. & Gacche, R. N. Exosomal signaling in cancer metastasis: Molecular insights and therapeutic opportunities. *Arch Biochem Biophys* **764**, 110277 (2025).
12. Fares, J., Cordero, A., Kanojia, D. & Lesniak, M. S. The Network of Cytokines in Brain Metastases. *Cancers* **13**, 142 (2021).
13. Zhang, W. & Huang, P. Cancer-stromal interactions. *Cancer Biol Ther* **11**, 150–156 (2011).
14. Pienta, K. J., Robertson, B. A., Coffey, D. S. & Taichman, R. S. The Cancer Diaspora: Metastasis beyond the seed and soil hypothesis. *Clin Cancer Res* **19**, 10.1158/1078-0432.CCR-13–2158 (2013).
15. Hoshino, A. *et al.* Tumour exosome integrins determine organotropic metastasis. *Nature* **527**, 329–335 (2015).
16. Shoaib, Z., Fan, T. M. & Irudayaraj, J. M. K. Osteosarcoma mechanobiology and therapeutic targets. *Br J Pharmacol* **179**, 201–217 (2022).
17. Allen, T. A. The Role of Circulating Tumor Cells as a Liquid Biopsy for Cancer: Advances, Biology, Technical Challenges, and Clinical Relevance. *Cancers (Basel)* **16**, 1377 (2024).

18. Arakil, N., Akhund, S. A., Elaasser, B. & Mohammad, K. S. Intersecting Paths: Unraveling the Complex Journey of Cancer to Bone Metastasis. *Biomedicines* **12**, 1075 (2024).
19. Wei, C. *et al.* Crosstalk between cancer cells and tumor associated macrophages is required for mesenchymal circulating tumor cell-mediated colorectal cancer metastasis. *Mol Cancer* **18**, 64 (2019).
20. Que, Z. *et al.* Polyphyllin VII induces CTC anoikis to inhibit lung cancer metastasis through EGFR pathway regulation. *Int J Biol Sci* **19**, 5204–5217 (2023).
21. Wang, Y., Shi, J., Chai, K., Ying, X. & Zhou, B. P. The Role of Snail in EMT and Tumorigenesis. *Curr Cancer Drug Targets* **13**, 963–972 (2013).
22. Kim, S. *et al.* Slug promotes survival during metastasis through suppression of Puma-mediated apoptosis. *Cancer Res* **74**, 3695–3706 (2014).
23. Perez-Oquendo, M. & Gibbons, D. L. Regulation of ZEB1 Function and Molecular Associations in Tumor Progression and Metastasis. *Cancers (Basel)* **14**, 1864 (2022).
24. Yang, J. *et al.* Twist, a master regulator of morphogenesis, plays an essential role in tumor metastasis. *Cell* **117**, 927–939 (2004).
25. Zhang, S. *et al.* Mesenchymal phenotype of circulating tumor cells is associated with distant metastasis in breast cancer patients. *Cancer Manag Res* **9**, 691–700 (2017).
26. Jiang, Z., Sun, H., Yu, J., Tian, W. & Song, Y. Targeting CD47 for cancer immunotherapy. *Journal of Hematology & Oncology* **14**, 180 (2021).

27. Spillane, C. D. *et al.* The induction of a mesenchymal phenotype by platelet cloaking of cancer cells is a universal phenomenon. *Transl Oncol* **14**, 101229 (2021).
28. Liu, C. *et al.* PDGF receptor-α promotes TGF-β signaling in hepatic stellate cells via transcriptional and posttranscriptional regulation of TGF-β receptors. *Am J Physiol Gastrointest Liver Physiol* **307**, G749–G759 (2014).
29. Zhan, Q. *et al.* New insights into the correlations between circulating tumor cells and target organ metastasis. *Sig Transduct Target Ther* **8**, 1–23 (2023).
30. Goto, W. *et al.* Circulating tumor cell clusters-associated gene plakoglobin is a significant prognostic predictor in patients with breast cancer. *Biomark Res* **5**, 19 (2017).
31. Fusi, A. *et al.* Expression of chemokine receptors on circulating tumor cells in patients with solid tumors. *J Transl Med* **10**, 52 (2012).
32. Anand, S., Samuel, M., Ang, C.-S., Keerthikumar, S. & Mathivanan, S. Label-Based and Label-Free Strategies for Protein Quantitation. *Methods Mol Biol* **1549**, 31–43 (2017).
33. Megger, D. A. *et al.* Comparison of label-free and label-based strategies for proteome analysis of hepatoma cell lines. *Biochim Biophys Acta* **1844**, 967–976 (2014).
34. Wu, W. *et al.* Antigen-independent single-cell circulating tumor cell detection using deep-learning-assisted biolasers. *Biosensors and Bioelectronics* **271**, 116984 (2025).
35. Hu, X., Zang, X. & Lv, Y. Detection of circulating tumor cells: Advances and critical concerns. *Oncol Lett* **21**, 422 (2021).
36. Fagotto, F. EpCAM as Modulator of Tissue Plasticity. *Cells* **9**, 2128 (2020).

37. Nicolini, A., Ferrari, P. & Rossi, G. Mucins and Cytokeratins as Serum Tumor Markers in Breast Cancer. *Adv Exp Med Biol* **867**, 197–225 (2015).
38. Riethdorf, S., O'Flaherty, L., Hille, C. & Pantel, K. Clinical applications of the CellSearch platform in cancer patients. *Adv Drug Deliv Rev* **125**, 102–121 (2018).
39. Wang, L. *et al.* Promise and limits of the CellSearch platform for evaluating pharmacodynamics in circulating tumor cells. *Semin Oncol* **43**, 464–475 (2016).
40. Rossi, E., Facchinetti, A. & Zamarchi, R. Customizing CellSearch platform. *Cytometry A* **83**, 595–598 (2013).
41. Swennenhuis, J. F. & Terstappen, L. Sample Preparation Methods Following CellSearch Approach Compatible of Single-Cell Whole-Genome Amplification: An Overview. *Methods Mol Biol* **1347**, 57–67 (2015).
42. Rostami, P. *et al.* Novel approaches in cancer management with circulating tumor cell clusters. *Journal of Science: Advanced Materials and Devices* **4**, 1–18 (2019).
43. Wang, L. *et al.* Promise and Limits of the CellSearch® Platform for Evaluating Pharmacodynamics in Circulating Tumor Cells (CTC). *Semin Oncol* **43**, 464–475 (2016).
44. Andree, K. C., van Dalum, G. & Terstappen, L. W. M. M. Challenges in circulating tumor cell detection by the CellSearch system. *Mol Oncol* **10**, 395–407 (2016).
45. Zhu, S., Jiang, F., Han, Y., Xiang, N. & Ni, Z. Microfluidics for label-free sorting of rare circulating tumor cells. *Analyst* **145**, 7103–7124 (2020).

46. Yap, K., Cohen, E. N., Reuben, J. M. & Khoury, J. D. Circulating Tumor Cells: State-of-the-art Update on Technologies and Clinical Applications. *Curr Hematol Malig Rep* **14**, 353–357 (2019).
47. Rawal, S., Yang, Y.-P., Cote, R. & Agarwal, A. Identification and Quantitation of Circulating Tumor Cells. *Annu Rev Anal Chem (Palo Alto Calif)* **10**, 321–343 (2017).
48. Hochstetter, A. *et al.* Deterministic Lateral Displacement: Challenges and Perspectives. *ACS Nano* **14**, 10784–10795 (2020).
49. Huang, D., Man, J., Jiang, D., Zhao, J. & Xiang, N. Inertial microfluidics: Recent advances. *Electrophoresis* **41**, 2166–2187 (2020).
50. Nasiri, R., Shamloo, A. & Akbari, J. Design of a Hybrid Inertial and Magnetophoretic Microfluidic Device for CTCs Separation from Blood. *Micromachines (Basel)* **12**, 877 (2021).
51. Musso, N. *et al.* Label-Free Enrichment of Circulating Tumor Plasma Cells: Future Potential Applications of Dielectrophoresis in Multiple Myeloma. *Int J Mol Sci* **23**, 12052 (2022).
52. Bogatyr, V., Biebricher, A. S., Bergamaschi, G., Peterman, E. J. G. & Wuite, G. J. L. Quantitative Acoustophoresis. *ACS Nanosci Au* **2**, 341–354 (2022).
53. Alnaimat, F., Dagher, S., Mathew, B., Hilal-Alnqbi, A. & Khashan, S. Microfluidics Based Magnetophoresis: A Review. *Chem Rec* **18**, 1596–1612 (2018).
54. Gupta, V. *et al.* ApoStream(TM), a new dielectrophoretic device for antibody independent isolation and recovery of viable cancer cells from blood. *Biomicrofluidics* **6**, 24133 (2012).

55. Balasubramanian, P. *et al.* Antibody-independent capture of circulating tumor cells of non-epithelial origin with the ApoStream® system. *PLoS One* **12**, e0175414 (2017).
56. Le Du, F. *et al.* EpCAM-independent isolation of circulating tumor cells with epithelial-to-mesenchymal transition and cancer stem cell phenotypes using ApoStream® in patients with breast cancer treated with primary systemic therapy. *PLoS One* **15**, e0229903 (2020).
57. Goater, A. D. & Pethig, R. Electrorotation and dielectrophoresis. *Parasitology* **117 Suppl**, S177-189 (1998).
58. Sarno, B., Heineck, D., Heller, M. J. & Ibsen, S. D. Dielectrophoresis: Developments and applications from 2010 to 2020. *Electrophoresis* **42**, 539–564 (2021).
59. Hawkins, B. G., Lai, N. & Clague, D. S. High-Sensitivity in Dielectrophoresis Separations. *Micromachines (Basel)* **11**, 391 (2020).
60. Henslee, E. A. Review: Dielectrophoresis in cell characterization. *Electrophoresis* **41**, 1915–1930 (2020).
61. Kung, Y.-C., Niazi, K. R. & Chiou, P.-Y. Tunnel dielectrophoresis for ultra-high precision size-based cell separation. *Lab Chip* **21**, 1049–1060 (2021).
62. Cen, E. G. *et al.* A combined dielectrophoresis, traveling wave dielectrophoresis and electrorotation microchip for the manipulation and characterization of human malignant cells. *J Microbiol Methods* **58**, 387–401 (2004).
63. Pethig, R. & Markx, G. H. Applications of dielectrophoresis in biotechnology. *Trends Biotechnol* **15**, 426–432 (1997).
64. Yoda, K., Ichikawa, Y. & Motosuke, M. Continuous-flow electrorotation (cROT): improved throughput characterization for dielectric properties of cancer cells. *Lab Chip* **23**, 4986–4996 (2023).

65. Huang, Y. *et al.* Separation of Simulants of Biological Warfare Agents from Blood by a Miniaturized Dielectrophoresis Device. *Biomedical Microdevices* **5**, 217–225 (2003).
66. Lim, S. W., Tran, T. M. & Abate, A. R. PCR-activated cell sorting for cultivation-free enrichment and sequencing of rare microbes. *PLoS One* **10**, e0113549 (2015).
67. Cai, D., Xiao, M., Xu, P., Xu, Y.-C. & Du, W. An integrated microfluidic device utilizing dielectrophoresis and multiplex array PCR for point-of-care detection of pathogens. *Lab Chip* **14**, 3917–3924 (2014).
68. Varshney, M., Li, Y., Srinivasan, B. & Tung, S. A label-free, microfluidics and interdigitated array microelectrode-based impedance biosensor in combination with nanoparticles immunoseparation for detection of *Escherichia coli* O157:H7 in food samples. *Sensors and Actuators B: Chemical* **128**, 99–107 (2007).
69. Malic, L. *et al.* Polymer-based microfluidic chip for rapid and efficient immunomagnetic capture and release of Listeria monocytogenes. *Lab Chip* **15**, 3994–4007 (2015).
70. Abdullah, A. *et al.* Microfluidic based impedance biosensor for pathogens detection in food products. *Electrophoresis* **40**, 508–520 (2019).
71. Li, Z., Fu, Y., Fang, W. & Li, Y. Electrochemical Impedance Immunosensor Based on Self-Assembled Monolayers for Rapid Detection of Escherichia coli O157:H7 with Signal Amplification Using Lectin. *Sensors* **15**, 19212–19224 (2015).
72. Rafati, A. & Gill, P. Microfluidic method for rapid turbidimetric detection of the DNA of Mycobacterium tuberculosis using loop-

mediated isothermal amplification in capillary tubes. *Microchim Acta* **182**, 523–530 (2015).

73. Liu, D., Liang, G., Zhang, Q. & Chen, B. Detection of Mycobacterium tuberculosis Using a Capillary-Array Microsystem with Integrated DNA Extraction, Loop-Mediated Isothermal Amplification, and Fluorescence Detection. *Anal. Chem.* **85**, 4698–4704 (2013).
74. Wang, R. *et al.* Impedimetric detection of bacteria by using a microfluidic chip and silver nanoparticle based signal enhancement. *Mikrochim Acta* **185**, 184 (2018).
75. Fang, X. *et al.* A portable and integrated nucleic acid amplification microfluidic chip for identifying bacteria. *Lab Chip* **12**, 1495–1499 (2012).
76. Poovathy, S., Hanan, A. & Husain, A. A Review on The Applications of Dielectrophoretic based Microfluidic Devices in Cancer Cell Detection. in *2023 Advances in Science and Engineering Technology International Conferences (ASET)* 1–4 (2023). doi:10.1109/ASET56582.2023.10180686.
77. Gascoyne, P. R. C. & Shim, S. Isolation of Circulating Tumor Cells by Dielectrophoresis. *Cancers (Basel)* **6**, 545–579 (2014).
78. Shim, S. *et al.* Antibody-independent isolation of circulating tumor cells by continuous-flow dielectrophoresis. *Biomicrofluidics* **7**, 11807 (2013).
79. Rahmati, M. & Chen, X. Separation of circulating tumor cells from blood using dielectrophoretic DLD manipulation. *Biomed Microdevices* **23**, 49 (2021).
80. Najafipour, I. *et al.* Dielectrophoresis-based microfluidics for detection and separation of circulating tumor cells. *Sensors and Actuators Reports* **9**, 100304 (2025).

81. Moon, H.-S. *et al.* Continuous separation of breast cancer cells from blood samples using multi-orifice flow fractionation (MOFF) and dielectrophoresis (DEP). *Lab Chip* **11**, 1118–1125 (2011).
82. Zhao, K. *et al.* Implementation of an Integrated Dielectrophoretic and Magnetophoretic Microfluidic Chip for CTC Isolation. *Biosensors* **12**, 757 (2022).
83. Gupta, V. *et al.* ApoStream(TM), a new dielectrophoretic device for antibody independent isolation and recovery of viable cancer cells from blood. *Biomicrofluidics* **6**, 24133 (2012).
84. Yeo, K. I. *et al.* Ultra-sensitive dielectrophoretic surface charge multiplex detection inside a micro-dielectrophoretic device. *Biosens Bioelectron* **210**, 114235 (2022).
85. Zhao, K. *et al.* Implementation of an Integrated Dielectrophoretic and Magnetophoretic Microfluidic Chip for CTC Isolation. *Biosensors* **12**, 757 (2022).
86. Bonacci, P. G. *et al.* Impact of buffer composition on biochemical, morphological and mechanical parameters: A tare before dielectrophoretic cell separation and isolation. *Transl Oncol* **28**, 101599 (2023).
87. Shim, S., Stemke-Hale, K., Noshari, J., Becker, F. F. & Gascoyne, P. R. C. Dielectrophoresis has broad applicability to marker-free isolation of tumor cells from blood by microfluidic systems. *Biomicrofluidics* **7**, 11808 (2013).
88. Huang, X. *et al.* On-chip microfluidic buffer swap of biological samples in-line with downstream dielectrophoresis. *Electrophoresis* **43**, 1275–1282 (2022).
89. Russo, G. I. *et al.* The Role of Dielectrophoresis for Cancer Diagnosis and Prognosis. *Cancers (Basel)* **14**, 198 (2021).

90. Caruso, G. *et al.* Receptor-mediated toxicity of human amylin fragment aggregated by short- and long-term incubations with copper ions. *Mol Cell Biochem* **425**, 85–93 (2017).
91. Li, H., Sun, S., Yap, J. Q., Chen, J. & Qian, Q. 0.9% saline is neither normal nor physiological. *J Zhejiang Univ Sci B* **17**, 181–187 (2016).
92. Torrisi, S. A. *et al.* Fluoxetine and Vortioxetine Reverse Depressive-Like Phenotype and Memory Deficits Induced by Aβ1-42 Oligomers in Mice: A Key Role of Transforming Growth Factor-β1. *Front. Pharmacol.* **10**, (2019).
93. Caruso, G. *et al.* Carnosine Decreases PMA-Induced Oxidative Stress and Inflammation in Murine Macrophages. *Antioxidants* **8**, 281 (2019).
94. Silva, A. M., Martins-Gomes, C., Ferreira, S. S., Souto, E. B. & Andreani, T. Molecular Physicochemical Properties of Selected Pesticides as Predictive Factors for Oxidative Stress and Apoptosis-Dependent Cell Death in Caco-2 and HepG2 Cells. *International Journal of Molecular Sciences* **23**, 8107 (2022).
95. Kus, M., Ibragimow, I. & Piotrowska-Kempisty, H. Caco-2 Cell Line Standardization with Pharmaceutical Requirements and In Vitro Model Suitability for Permeability Assays. *Pharmaceutics* **15**, 2523 (2023).
96. Dalton, C., Goater, A. D., Drysdale, J. & Pethig, R. Parasite viability by electrorotation. *Colloids and Surfaces A: Physicochemical and Engineering Aspects* **195**, 263–268 (2001).
97. Front Matter. in *Flat Panel Display Manufacturing* i–xxvii (John Wiley & Sons, Ltd, 2018). doi:10.1002/9781119161387.fmatter.
98. Moscato, S. *et al.* Automated Electrorotation System for High-Throughput Dielectric Cell Characterization. *IEEE Transactions on*

Biomedical Engineering 1–10 (2025) doi:10.1109/TBME.2025.3617496.

99. Grand, R. S. *et al.* BANP opens chromatin and activates CpG-island-regulated genes. *Nature* **596**, 133–137 (2021).
100. Zebda, N., Dubrovskyi, O. & Birukov, K. G. Focal adhesion kinase regulation of mechanotransduction and its impact on endothelial cell functions. *Microvasc Res* **83**, 71–81 (2012).
101. Dielectrophoretic Studies of Bioparticles. in *Dielectrophoresis* 309–379 (John Wiley & Sons, Ltd, 2017). doi:10.1002/9781118671443.ch11.
102. Nga, N. T. H., Ngoc, T. T. B., Trinh, N. T. M., Thuoc, T. L. & Thao, D. T. P. Optimization and application of MTT assay in determining density of suspension cells. *Analytical Biochemistry* **610**, 113937 (2020).
103. Morgan, T. Effect of NaCl on composition and volume of cells of the rat papilla. *Am J Physiol* **232**, F117-122 (1977).
104. García, M. J. & Ardila, A. M. Cell volume variation under different concentrations of saline solution (NaCL). *Revista Colombiana de Anestesiología* **37**, 101–105 (2009).
105. Voldman, J. Electrical forces for microscale cell manipulation. *Annu Rev Biomed Eng* **8**, 425–454 (2006).
106. Placing Dielectrophoresis into Context as a Particle Manipulator. in *Dielectrophoresis* 1–29 (John Wiley & Sons, Ltd, 2017). doi:10.1002/9781118671443.ch1.
107. Welc, S. S. & Clanton, T. L. The regulation of interleukin-6 implicates skeletal muscle as an integrative stress sensor and endocrine organ. *Exp Physiol* **98**, 359–371 (2013).

108. Förstermann, U. & Sessa, W. C. Nitric oxide synthases: regulation and function. *Eur Heart J* **33**, 829–837 (2012).

109. Pethig, R. & Markx, G. H. Applications of dielectrophoresis in biotechnology. *Trends Biotechnol* **15**, 426–432 (1997).

110. Shen, W.-C. *et al.* Methylation and PTEN activation in dental pulp mesenchymal stem cells promotes osteogenesis and reduces oncogenesis. *Nat Commun* **10**, 2226 (2019).

111. Huang, J. *et al.* Electrical regulation of Schwann cells using conductive polypyrrole/chitosan polymers. *J Biomed Mater Res A* **93**, 164–174 (2010).

112. Zhao, H. *et al.* Tumor microenvironment derived exosomes pleiotropically modulate cancer cell metabolism. *eLife* **5**, e10250 (2016).

113. Castellanos, A., Ramos, A., González, A., Green, N. G. & Morgan, H. Electrohydrodynamics and dielectrophoresis in microsystems: scaling laws. *J. Phys. D: Appl. Phys.* **36**, 2584 (2003).

114. Kwak, M. *et al.* Adherens junctions organize size-selective proteolytic hotspots critical for Notch signalling. *Nat Cell Biol* **24**, 1739–1753 (2022).

115. Yeung, T. M., Gandhi, S. C., Wilding, J. L., Muschel, R. & Bodmer, W. F. Cancer stem cells from colorectal cancer-derived cell lines. *Proc Natl Acad Sci U S A* **107**, 3722–3727 (2010).

116. Huang, L., Liang, F., Feng, Y., Zhao, P. & Wang, W. On-chip integrated optical stretching and electrorotation enabling single-cell biophysical analysis. *Microsyst Nanoeng* **6**, 57 (2020).

117. Han, S.-I., Joo, Y.-D. & Han, K.-H. An electrorotation technique for measuring the dielectric properties of cells with simultaneous use

of negative quadrupolar dielectrophoresis and electrorotation. *Analyst* **138**, 1529–1537 (2013).

118. Babu, S., Takeuchi, Y. & Masai, I. Banp regulates DNA damage response and chromosome segregation during the cell cycle in zebrafish retina. *eLife* **11**, e74611 (2022).

119. Bortner, C. D., Gómez-Angelats, M. & Cidlowski, J. A. Plasma Membrane Depolarization without Repolarization Is an Early Molecular Event in Anti-Fas-induced Apoptosis*. *Journal of Biological Chemistry* **276**, 4304–4314 (2001).

120. Wang, H. *et al.* Correlation between the dielectric properties and biological activities of human ex vivo hepatic tissue. *Phys. Med. Biol.* **60**, 2603 (2015).

121. Ramdas, N. M. & Shivashankar, G. V. Cytoskeletal control of nuclear morphology and chromatin organization. *J Mol Biol* **427**, 695–706 (2015).

122. Alisafaei, F., Jokhun, D. S., Shivashankar, G. V. & Shenoy, V. B. Regulation of nuclear architecture, mechanics, and nucleocytoplasmic shuttling of epigenetic factors by cell geometric constraints. *Proc Natl Acad Sci U S A* **116**, 13200–13209 (2019).

123. Rappel, W.-J. & Edelstein-Keshet, L. Mechanisms of Cell Polarization. *Curr Opin Syst Biol* **3**, 43–53 (2017).

124. Baba, A. I. & Câtoi, C. TUMOR CELL MORPHOLOGY. in *Comparative Oncology* (The Publishing House of the Romanian Academy, 2007).

125. Parsons, J. T., Horwitz, A. R. & Schwartz, M. A. Cell adhesion: integrating cytoskeletal dynamics and cellular tension. *Nat Rev Mol Cell Biol* **11**, 633–643 (2010).

126. Bilodeau, A. R. The Pros and Cons of Adherent Versus Suspension Cell Culture | BioPharm International. https://www.biopharminternational.com/view/the-pros-and-cons-of-adherent-versus-suspension-cell-culture (2025).
127. Humphrey, J. D., Dufresne, E. R. & Schwartz, M. A. Mechanotransduction and extracellular matrix homeostasis. *Nat Rev Mol Cell Biol* **15**, 802–812 (2014).
128. Moscato, S. *et al.* IP05-09 LABEL-FREE CHARACTERIZATION OF PROSTATE CANCER CELLS: A NOVEL AUTOMATED ELECTRO CELL-PHYSIOMETRY (ECP) PLATFORM FOR LIQUID BIOPSY. BIOPSY. *The Journal of Urology* https://doi.org/10.1097/01.JU.0001109816.50355.3c.09 (2025) doi:10.1097/01.JU.0001109816.50355.3c.09.